The Dissertation Committee for Taewoo Ha Certifies that this is the approved version of the following Dissertation:

Flexible and Stretchable Piezoelectric Bio-Integrated Sensors and Energy Harvesters Based on Polyvinylidene Fluoride (PVDF)

Committee:

Nanshu Lu, Supervisor

Jonathan W. Valvano

Ananth Dodabalapur

Thomas Milner

Jayant Sirohi

Flexible and Stretchable Piezoelectric Bio-Integrated Sensors and Energy Harvesters Based on Polyvinylidene Fluoride (PVDF)

by

Taewoo Ha

Dissertation

Presented to the Faculty of the Graduate School of

The University of Texas at Austin

in Partial Fulfillment

of the Requirements

for the Degree of

Doctor of Philosophy

The University of Texas at Austin

August 2018

Dedication

Dedicated to my family

Acknowledgements

First and foremost, my deepest and sincere appreciation should go to Professor Nanshu Lu. Thanks to her thoughtful guidance in research and heartfelt advice about personal life, I have truly grown as a better person, both professionally and personally. When I had difficulty in continuing my Ph. D program, Dr. Lu recognized my potential and assigned me to her research group, which was the most dramatic turning point in my life. Her patience and unwavering trust in me have been the biggest support for my research work. Through enthusiastic discussions about research topics and issues with her, I have received many inspirations and genuinely enjoyed doing research. It is not excessive to say that Dr. Lu is the greatest mentor, advisor, and supporter in my life.

I am grateful to my committee members, Prof. Jonathan W. Valvano, Prof. Ananth Dodabalapur, Prof. Thomas Milner, and Prof. Jayant Sirohi for allowing their time to guide my research with valuable comments and advices. With their direction, this thesis could be clear and persuasive. The collaborations with the research group of Prof. Jayant Sirohi and his student, Jason Tran, have significantly improved the thesis. I would also like to thank Dr. John X.J. Zhang and Dr. Ramesh Yerraballi for advising and supporting me while I was working as a teaching assistant in the biomedical engineering department.

I thankfully acknowledge the financial support from US Air Force Office of Scientific Research (AFOSR) under Grant No. FA9550-15-1-0112, US Office of Naval Research (ONR) under Grant No. N00014-16-1-2044, and US National Science Foundation (NSF) under Grant No. CMMI-1351875.

I would like to thank the group members, Dr. Shixuan Yang, Dr. Shutao Qiao, Dr. Christopher Brennan, Dr. Shideh Kabiri Ameri, Daniel Sanchez, Liu Wang, Siyi Liu, Hyoyoung Jeong, Hongwoo Jang, Zhaohe Dai, Kyoungho Ha, Xiangxing Yang, Heeyong Huh, and all previous members. Working with the members of Lu research group was a deeply memorable experience during my graduate school years. Thanks to the group, I learned a lot while collaborating with them for the research project, and I could expedite the project with less trials and errors. They were always willing to discuss any subjects, including research problems, and I really enjoyed our conversations. Every one of them was kind, professional, and humorous.

Special thanks to my friends, Dr. Kunhee Cho, Dr. Jeonggoo Song, Dr. Jeeho Ryu, Dr. Donghyun Kim, Dr. Seohee Kim, Dr. Sangeun Park, Dr. Junse Lee, Dr. Changmin Lee, Dr. Joon Sohn, Jaehyun Kim, Soonil Lee, and all others who have been kind and shared their time with me. Without them, my life of studying abroad would have been boring and miserable. I am extremely delighted that most people around me have successfully achieved their goal and they are working toward a better life.

My parents, my sister, parents-in law, and relatives were the best supporters in my life, although we have been apart for several years. Their unconditional love makes me courageous and confident and gave me the strength to make it this far. I hope this thesis is the start of returning the love I have received.

Lastly, I give many thanks to my wife, Hani Khang, for loving and supporting me for all these years. I am so thankful of your patience, maintaining two years of our long-distance relationship, and your courageous decision to accept my proposal, which was probably one of the most difficult decisions you have ever made. I think meeting you was the best thing that ever happened to me, and I am proud that I could mention you in the

outcome of my efforts. As we have overcome many difficult times together, I believe our relationship will remain steadfast.

Flexible and Stretchable Piezoelectric Bio-Integrated Sensors and Energy Harvesters Based on Polyvinylidene Fluoride (PVDF)

Taewoo Ha, Ph.D.

The University of Texas at Austin, 2018

Supervisor: Nanshu Lu

Piezoelectricity is a phenomenon that electric energy is generated in a certain material when the material is subjected to mechanical load, and vice versa. Piezoelectric devices with high stretchability and flexibility for bio-integrated applications, including skin-conformal strain sensors and energy harvesters, have been developed for many years. However, the manufacturing process for conventional ceramic-based piezoelectric materials is sophisticated, expensive, and time-consuming. In contrast, piezoelectric polymer sheets, such as polyvinylidene fluoride (PVDF), are commercially available, mechanically robust, biocompatible, and less demanding to manufacture. This dissertation introduces low-cost, stretchable bio-integrated sensors and energy harvesters based on PVDF, and a novel subtractive digital manufacturing method for them called the "cut-and-paste" method. To systematically investigate our devices, we developed analytical, numerical, and experimental methods and obtained consistent results. As one demonstration, we created a filamentary serpentine (FS) network of 28-μm-thick PVDF as the soft and stretchable vibration sensor and attached the sensor on human chest to measure seismocardiography (SCG), which reflects chest vibration associated with heartbeats. The SCG measured by our PVDF sensor was comparable with conventional accelerometers,

but PVDF sensor was much softer and imperceptible to wear. To optimize the SCG sensing location and to clarify the effect of the skin-sensor elastic mismatch, full-field displacement and strain analysis of the chest motion was conducted via three-dimensional digital image correlation (3D DIC) method. Integrating the FS PVDF-based SCG sensor with Au-based electrocardiogram (ECG) sensors, a skin-soft electro- and mechano-acoustic cardiovascular (EMAC) sensing tattoo has been created. It can synchronously collect electrical and mechanical cardiovascular signals which when combined, can fully reveal the cardiac mechanics such as the pre-ejection period (PEP), the isovolumetric contraction time (ICT), etc. Based on the strong negative correlations between systolic time intervals and systolic/diastolic blood pressures, continuous blood pressure (BP) could be non-invasively tracked via the EMAC sensing tattoo. As another demonstration, we created serpentine PVDF based stretchable energy harvester. We had to optimize the electrode design to minimize the counter effect due to the opposite signs of strain developed in the serpentine ribbon when subjected to stretch. After optimization, the serpentine ribbon exhibits much higher stretchability but comparable attainable electrical outputs with the straight PVDF ribbons.

Table of Contents

List of Tables

List of Figures

Chapter 1: Introduction

This chapter describes the background and motivation for flexible and stretchable piezoelectric devices based on polyvinylidene fluoride (PVDF) for bio-integrated applications. It will also introduce a time- and cost-effective manufacturing process we used, the "cut-and-paste" method. A roadmap for this dissertation is offered at the end of this chapter.

1.1 BACKGROUND

Recent advances in micro-electro-mechanical systems (MEMS) technology and novel functional materials show a possibility to realize battery-free medical devices in the near future. Self-powered devices collect and use energy from ambient environments such as surrounding temperature [1], humidity [2], and mostly mechanical motion [3, 4] to recharge their own battery; or directly transduce the energy to electrical signal [5]. This enables medical devices, including medical health monitoring devices [6], pacemakers [7], and hearing aids [8], to run for a prolonged time.

Depending on the energy harvesting principle, e.g., thermoelectricity, triboelectricity, and piezoelectricity, there are numerous functional materials for self-powered devices. For example, thermoelectric or pyroelectric material converts thermal energy to electrical energy, while triboelectric or piezoelectric material convert mechanical energy to electrical energy [9]. Particularly for implantable applications, mechanical transducers can utilize the mechanical energy from the motion of organs, which is consistent and stable, compared to the thermal energy from the temperature difference between the human body and air [10].

Owing to their simplicity, high sensitivity, and zero operating power, piezoelectric materials have been used in various applications as sensors or actuators, including strain sensors [11, 12], pressure sensors [13, 14], ultrasonic devices [15, 16], and linear actuators [17, 18]. Widely-used piezoelectric materials including quartz, barium titanate ($BaTiO_3$) [19], lead zirconate titanate (PZT) [20], and zinc oxide (ZnO) [21] are intrinsically rigid

and fragile. Hence it is difficult to incorporate them in bio-integrated devices as the large deformation of human tissues may easily cause fracture to them [22, 23]. Furthermore, mounting such rigid devices may be obstructive and uncomfortable for the patient, as well as creating error in the biosignal measurement due to the elastic mismatch between the devices and the human tissue. Polymeric piezoelectric materials such as polyvinylidene fluoride (PVDF) [24] and porous electromechanical film (EMFi) [25] are intrinsically more compliant, but their piezoelectric coefficients are smaller than those of the ceramic ones [26]. Table 1.1 shows the properties of piezoelectric materials with respect to their molecular structures [27-31].

Material Type	Quartz-Like	Perovskites	Polymers
Materials	SiO_2(Quartz), $LiNbO_3$,$LiTaO_3$	Pb(Ti, Zr)O_3 (PZT), $BaTiO_3$	PVDF, PVDF-TrFE
Piezoelectric Coefficient d_{33} [pC/N]	5-30	50-500	5-30
Relative Dielectric Constant	5-15	500-1000	5-15
Elastic Stiffness [GPa]	> 100	50 - 100	1-10
Strain-to-Rupture (%)	1 %	0.2 %	2 %
Manufacturability	Simple	Sophisticated	Moderate
Processability	Difficult	Difficult	Easy

Table 1.1. Properties of Piezoelectric Materials

In the last few decades, emerging research on flexible and stretchable electronics technology enabled mechanically robust piezoelectric devices for bio-integrated applications. For example, Dagdeviren, et al. invented a conformal piezoelectric energy

harvester with 500 nm PZT layer on 75 μm polyimide and successfully demonstrated its energy harvesting performance on the bovine heart, as described in Fig. 1.1 (a) [32]. In this case, the superior flexibility from the thinness of the device allows to it to sustain the curvature variation of the organs [33-35]. Yet flexibility is not sufficient to model a device on to a bio tissue, which has complex surfaces and exhibits large deformation of more than 20 % [36]. For decades, structural approaches such as the wavy buckling structures of thin PZT ribbons [37] have been proposed to achieve a high system compliance and limit strains in devices below the fracture point. Figure 1.1 (b) shows an example of stretchable piezoelectric devices by Qi and co-workers. After PZT crystalline materials were grown on a stripe-patterned MgO crystal substrate, the PZT materials were transferred to a poly(dimethyl siloxane) (PDMS) substrate via the stretch-attach-release method to achieve a wavy structure of PZT ribbons [37]. Notably, the stretchable device showed an enhanced piezoelectric performance, which is presumably derived from the strain gradient at the buckled regions. Similar approaches were suggested by Feng et al. [38]; They confirmed that the wavy PZT nanoribbons integrated with elastomer substrates (Fig. 1.1 (c)) exhibit higher stretchability (8 %) than rigid flat films casted on rigid silicon substrates, while maintaining comparable ferroelectricity and piezoelectricity than that of flat films.

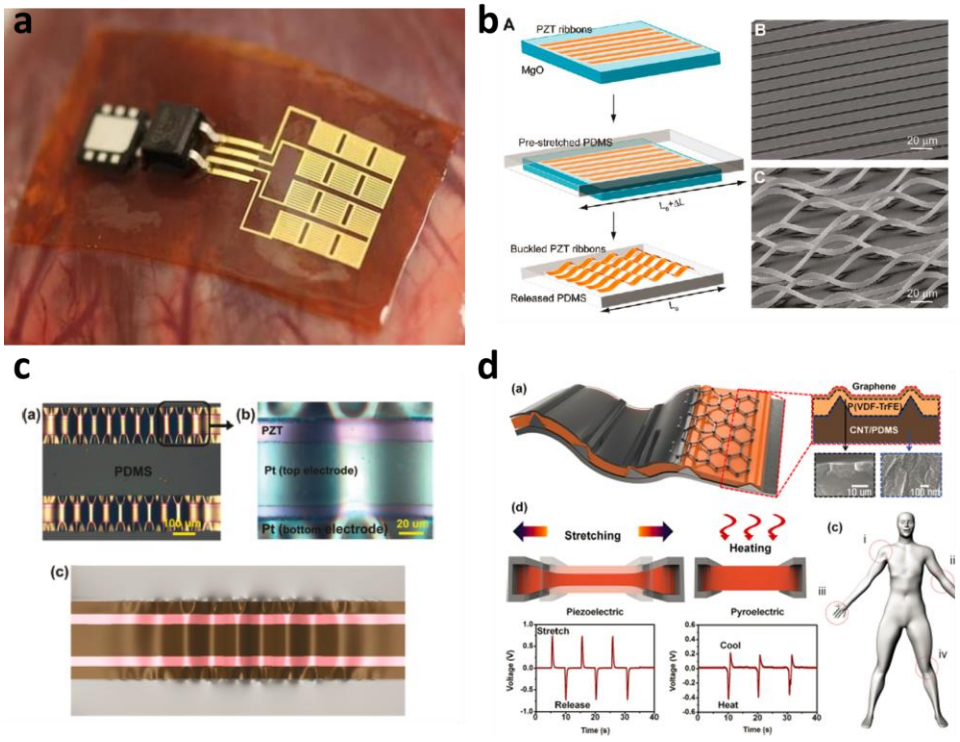

Figure 1.1. Flexible and Stretchable Bio-integrated Devices. (a) A conformal piezeoelctric energy harvester on a bovine heart [32]. (b) Energy harvesting devices fabricated from buckled PZT ribbons [37]. (c) A wavy PZT nanoribbons with electrodes on PDMS [38]. (d) A skin-conformal piezoelectric generator made of PVDF copolymer [39].

A critical challenge to manufacturing stretchable piezoelectric devices is the fabrication process. Most ceramic-based piezoelectric materials require an annealing process in vacuum at a high temperature for high-quality crystallization [26]. Furthermore, the brittleness of solid piezoelectric materials hinders the direct deposition, as well as

patterning or printing, of piezoelectric materials on a soft substrate the more complex pattern a device has, the more expensive the production cost.

Compared to solid piezoelectric materials, piezoelectric polymers are mechanically robust, biocompatible, and less demanding on manufacturing and engineering. For this reason, piezoelectric polymers are used in many biomedical applications such as strain sensors [40], pressure sensors [41], and energy harvesters [42], despite their low piezoelectric coefficient. The curing temperature is less than 300 ^{o}C in many cases found in the literature [26]. Since piezoelectric polymers are solution-processible, various fabrication techniques are applicable, e.g., spin-coating [43], electrospun printing [44], and inkjet printing [45], which makes mechanically robust piezoelectric polymer-based devices feasible. For example, a skin-conformal piezoelectric generator made of PVDF copolymer was invented by J. Lee and colleagues [39]. The device structure is described in Fig. 1.1 (d). Polyvinylidene fluoride trifluoro ethylene (PVDF-TrFE) was cast on a composite of carbon nanotubes (CNTs) and PDMS and then covered by a graphene nanosheet. Due to low stiffness of electrode layers and a micro-line-patterning on CNT/PDMS composite, the device was stretchable up to 30 %, which corresponds with the stretchability of human skin. Therefore, genuine bio-integrated, self-powered devices for bio-integrated applications may be possible via piezoelectric polymers with novel structures.

1.2 MOTIVATION

Despite the efforts on ceramics-based stretchable piezoelectric devices, the intrinsic stiffness and brittleness of ceramics greatly limit their potential for bio-integration. Currently, the designs of such devices are mostly empirical. Furthermore, the photolithography-based manufacturing process of those devices is complicated, costly and time-consuming.

Since piezoelectric polymers such as PVDF are commercially available, mechanically robust, and biocompatible, they can be used in bio-integrated devices which demand high sensitivity and zero operating power. In addition, the freeform and low-cost "cut-and-paste" process invented by our group [46] may be directly applicable to PVDF.

Based on the mechanical advantages and processability of piezoelectric polymers, it is possible to build tissue-soft stretchable and unobstructive bio-integrated piezoelectric devices out of PVDF. The research goals of this dissertation include: 1) build analytical and numerical models for flexible and stretchable structures of the piezoelectric materials to provide rigorous mathematical tools to design soft piezoelectric devices; 2) establish a low-cost, rapid prototyping process for such devices; 3) fabricate flexible and stretchable bio-integrated piezoelectric sensors with high sensitivity and generators with high energy density.

1.3 DISSERTATION ROADMAP

The research objective of this dissertation is to design, manufacture, and test soft bio-integrated sensors and generators out of piezoelectric polymers such as PVDF. Chapter 2 will summarize the basic mechanical and electromechanical properties of PVDF and discuss existing flexible and stretchable bio-integrated devices based on PVDF. To fully understand flexible piezoelectric devices, a linear piezoelectric theory is established for analyzing piezoelectric unimorphs under various boundary conditions in Chapter 3. As flexibility is not enough for soft bio-tissue, we will move on to the modeling and manufacture of stretchable piezoelectric serpentines and their practical application of monitoring seismocardiogram (SCG) on the surface of the human chest in Chapter 4. The sensing location of SCG on the chest will be optimized via the full-field, three-dimensional digital image correlation (3D DIC) method in Chapter 5. Chapter 6 will discuss a dual-mode stretchable electronic tattoo (E-tattoo) for noninvasive but synchronous electrocardiogram (ECG) and SCG sensing, which can be combined for the continuous estimation of blood pressure. As another application of PVDF serpentines, a stretchable generator enhanced by the engraving method will be introduced in Chapter 7. Conclusions of the dissertation and future research directions will be presented in Chapter 8.

Chapter 2: Elastic and Piezoelectric Properties of PVDF

This chapter reviews fundamental linear piezoelectric theories and the characterization of directly purchased 28-μm thick PVDF sheets. Elastic and piezoelectric properties were measured experimentally and anisotropy was noted. Applications of PVDF as bio-integrated devices are introduced.

2.1 PIEZOELECTRICITY

The origin of the word "piezo" is the Greek, which means "to press." The piezoelectric effect was first discovered by Curie [47]. Piezoelectricity can be defined as a direct conversion between the electrical energy and mechanical energy. Bi-directionality is a distinct property of piezoelectricity, compared with triboelectricity. As described in Fig. 2.1 (a), the polarization is induced by the external tension; hence, charges are generated on electrodes. The direct piezoelectric effect, which is applicable to sensors or energy generators [48], can be written as

$$P_T = dT\ , \tag{2.1}$$

where P_T is the piezoelectric polarization induced by the stress T, and d is the piezoelectric coupling coefficient. The diagram Fig. 2.1 (b) shows the inverse piezoelectric effect that the external electric field deforms the piezoelectric material. The inverse piezoelectric effect can be formulated as

$$S_E = d^t E_{in}, \tag{2.2}$$

where S_E is the strain induced by the electric field observed in the piezoelectric material E_{in}, and d^t is the inverse piezoelectric coupling coefficient. This inverse piezoelectric effect can be applied to actuator applications including acoustic devices [49]. Note that the direction of induced polarization by direct piezoelectric effect and induced strain by inverse piezoelectric effect will be reversed when the poling direction is opposite (bottom of Fig. 2.1 (a) and (b)).

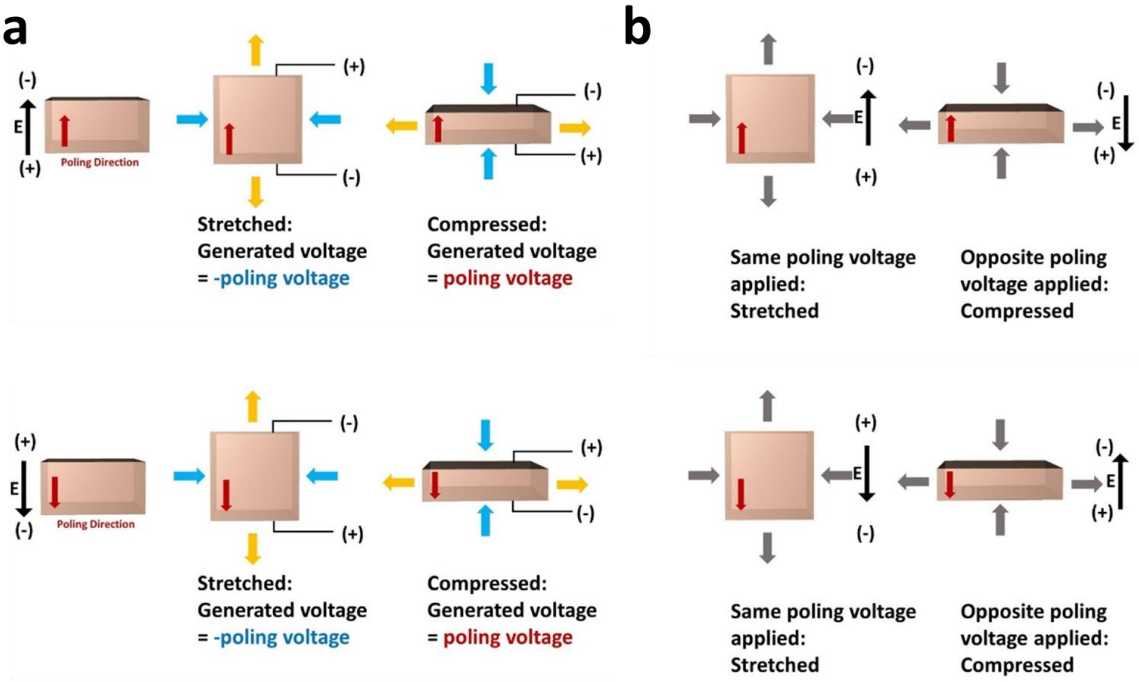

Figure 2.1. (a) The direct piezoelectric effect and (b) the inverse piezoelectric effect.

The assumption behind Equation (2.1) is there is no external electric field. To generalize the problem, we should define the general electric displacement field for piezoelectric materials. As illustrated in Fig. 2.2, the electrostatic definition of the electric displacement field induced by the external electric field is given as

$$D = \varepsilon_0 E_{ex} = \varepsilon_0 \varepsilon_r E_{in} = \varepsilon_0 E_{in} + P_E , \tag{2.3}$$

where D is the electric displacement field, E_{ex} is the external electric field, E_{in} is the electric field observed in the dielectric material, P_E is the polarization induced by the external electric field, ε_r is the relative permittivity of the piezoelectric material and ε_0 is the free space permittivity of which the value is $8.854\times10^{-12}(\mathrm{F/m})$ [50]. In general electrostatics, the Equation (2.3) denotes the dielectric effect to the electric field. If the external electric field is applied to the dielectric material, the magnitude of electric field decreases because some of the electric field forms polarization.

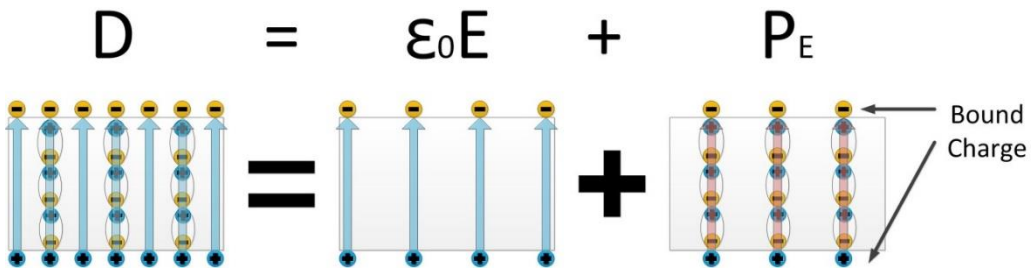

Figure 2.2. The relation among the electric displacement field, electric field and polarization.

Combining the Equation (2.1) and (2.3), the general definition of electric displacement for piezoelectric materials is

$$D = \varepsilon_0 E_{in} + P_E + P_T = \varepsilon_0 \varepsilon_r^T E_{in} + dT\,, \tag{2.4}$$

where ε_r^T is the relative permittivity under constant stress, P_E is the polarization induced by the external electric field, and P_T is the polarization induced by the stress. The

Equation (2.4) asserts that the electric displacement field of a piezoelectric material can be created by the external electric field or the external mechanical stimulus. If both are applied, the total polarization in the piezoelectric material is the sum of the P_E and P_T, assuming there is no thermal loss.

In a similar manner, the general elastic property of the piezoelectric material can be also formulated. From the Hooke's Law, the relation between the stress and the strain is

$$S_T = sT, \tag{2.5}$$

where S_T is the strain derived from the stress and *s* is the compliance coefficient. The total strain caused by the stress and the electric field derived from the Equation (2.2) and the (2.5) is

$$S = S_T + S_E = s^E T + d^t E_{in}, \tag{2.6}$$

where s^E denotes the elastic compliance coefficient under constant electric field. The Equation (2.6) describes the strain of a piezoelectric material can be caused by the external mechanical stimulus or the external electric field. For the notation unification, the electric field term in the Equation (2.4) and (2.6) is specified with the notation E_{in}, which is the electric field observed in the piezoelectric material. The relation between the external electric field and the internal electric field is $E_{ex} = \varepsilon_r E_{in}$. The electric field notation will be unified as *E* meaning the internal electric field from now on.

The pole direction of the polarization depends on the force direction since the piezoelectric materials are basically anisotropic [7]. This directional nature of piezoelectric materials can be controlled mostly through the pretreatment process called poling process [8]. To describe the anisotropic property analytically, the Equation (2.4) and (2.6) are usually described as tensor.

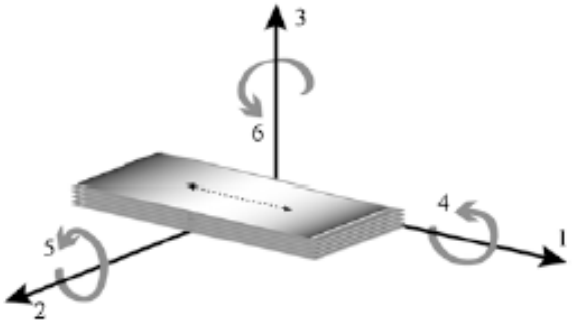

Figure 2.3. Tensor directions in 1-6 numbering system [51].

For convenience, redefinition of the coordinate expression is required; x-x: 11, y-y: 22, z-z: 33, x-y: 12, x-z: 13, y-z: 23. Usually, the numberings are further simplified as described in the Figure 2.3; $11 \rightarrow 1$, $22 \rightarrow 2$, $33 \rightarrow 3$, $23 \rightarrow 4$, $13 \rightarrow 5$, $12 \rightarrow 6$ [51]. This numbering system will be used for the simplicity and the unification from now on. Following the direction numbering notation above, the Equation (2.4) and (2.6) become

$$\begin{bmatrix} D_1 \\ D_2 \\ D_3 \end{bmatrix} = \begin{bmatrix} d_{11} & d_{12} & d_{13} & d_{14} & d_{15} & d_{16} \\ d_{21} & d_{22} & d_{23} & d_{24} & d_{25} & d_{26} \\ d_{31} & d_{32} & d_{33} & d_{34} & d_{35} & d_{36} \end{bmatrix} \begin{bmatrix} T_1 \\ T_2 \\ T_3 \\ T_4 \\ T_5 \\ T_6 \end{bmatrix} + \varepsilon_0 \times \begin{bmatrix} \varepsilon_{r11}^T & \varepsilon_{r12}^T & \varepsilon_{r13}^T \\ \varepsilon_{r21}^T & \varepsilon_{r22}^T & \varepsilon_{r23}^T \\ \varepsilon_{r31}^T & \varepsilon_{r32}^T & \varepsilon_{r33}^T \end{bmatrix} \begin{bmatrix} E_1 \\ E_2 \\ E_3 \end{bmatrix} \tag{2.7}$$

$$\begin{bmatrix} S_1 \\ S_2 \\ S_3 \\ S_4 \\ S_5 \\ S_6 \end{bmatrix} = \begin{bmatrix} s_{11}^E & s_{12}^E & s_{13}^E & s_{14}^E & s_{15}^E & s_{16}^E \\ s_{21}^E & s_{22}^E & s_{23}^E & s_{24}^E & s_{25}^E & s_{26}^E \\ s_{31}^E & s_{32}^E & s_{33}^E & s_{34}^E & s_{35}^E & s_{36}^E \\ s_{41}^E & s_{42}^E & s_{43}^E & s_{44}^E & s_{45}^E & s_{46}^E \\ s_{51}^E & s_{52}^E & s_{53}^E & s_{54}^E & s_{55}^E & s_{56}^E \\ s_{61}^E & s_{62}^E & s_{63}^E & s_{64}^E & s_{65}^E & s_{66}^E \end{bmatrix} \begin{bmatrix} T_1 \\ T_2 \\ T_3 \\ T_4 \\ T_5 \\ T_6 \end{bmatrix} + \begin{bmatrix} d_{11} & d_{12} & d_{13} \\ d_{21} & d_{22} & d_{23} \\ d_{31} & d_{32} & d_{33} \\ d_{41} & d_{42} & d_{43} \\ d_{51} & d_{52} & d_{53} \\ d_{61} & d_{62} & d_{63} \end{bmatrix} \begin{bmatrix} E_1 \\ E_2 \\ E_3 \end{bmatrix} \tag{2.8}$$

2.2 PROPERTIES OF PVDF

Although stretchable electromechanical devices based on patterned inorganic piezoelectric materials such as lead zirconate titanate (PZT) or zinc oxide (ZnO) have been reported [37, 38, 52, 53], those materials are hardly applicable to bio-integrated applications because of their intrinsic brittleness. Furthermore, the lead included in some ceramic-based piezoelectric materials are toxic. Piezoelectric polymer materials such as polyvinylidene fluoride (PVDF) are adequate substitutes for bio-integrated applications. The piezoelectricity in polymers discovered by Kawai broadens the application area where the mechanical flexibility is required [54]. Despite their relatively small piezoelectric coefficients, piezoelectric polymers are used in many bio-integrated applications because of the call for mechanical flexibility and biocompatibility. Furthermore, the voltage capability is higher than other materials, which is an advantage in sensor applications where the current is less important [55].

Polyvinylidene fluoride (PVDF) is a commercially available piezoelectric polymer that is mechanically robust and biocompatible, but is intrinsically stiff (Young's modulus = 2-4 GPa) compared with human skin [56, 57]. Stretchable electromechanical sensors or energy harvesters made of patterned PVDF are emerging in recent years. For example, line-type micro-patterned PVDF membrane [39], ribbon-like PVDF embedded in Ecoflex [58], and PVDF islands interconnected by serpentine metal wires [59] have shown stretchability around 30%, but their thinness and softness have not been explicitly addressed. Electrospun PVDF fibers have been employed for wearable sensors and energy

harvesters, but so far electrodes could only be placed at the ends of the fiber bundles instead of along each fiber in most cases [60-62]. Overall, thin PVDF devices are preferable for bio-integrated applications because of its mechanical robustness and slimness.

PVDF is a dielectric material. When an external electric field is applied, electric charges cannot flow through PVDF but molecules composing PVDF are polarized with respect to the direction of applied electric field. The dielectric constant of PVDF is known to be 7-8 [63]. The piezoelectricity of PVDF depends on the chain phase. There are several molecular phases of PVDF chains, and most untreated PVDF products are in the α-phase. As described in Fig. 2.4, the α-phase PVDF, of which hydrogen atoms and neighbored fluorine atoms are antiparallel to each other, has no dipole moment since dipoles are locally compensated. Thus, the α-phase PVDF is a paraelectric material that can be polarized by an external electric field without permanent dipoles in the material. On the contrary, the β-phase PVDF, of which hydrogen atoms and fluorine atoms are parallel in chain direction, is a ferroelectric material that possesses spontaneous electric polarization that is switchable by an external electric field [64]. Among all molecular phases of PVDF, the β-phase PVDF exhibits most significant ferroelectricity; and as all ferroelectric materials, the β-phase PVDF produces charges under strains (piezoelectricity). The β-phase PVDF can be artificially formed through thermal and electromechanical poling process [65]. For example, applying high voltage across the thickness of a PVDF film while heating the film over 70 °C aligns polymer chains to have the thickness direction of dipole moments; the elongated polarization tendency remains permanently, as described in the Fig. 2.5.

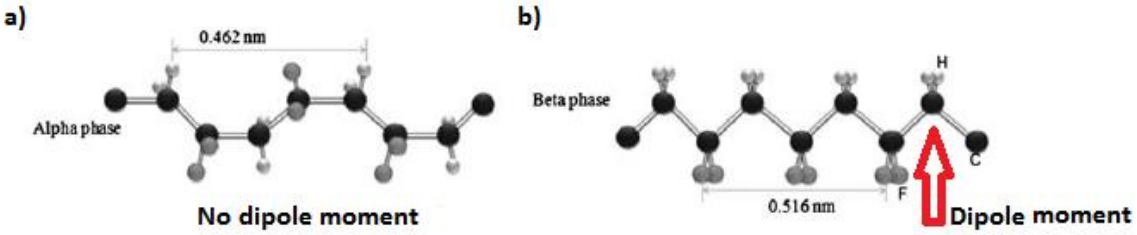

Figure 2.4. PVDF polymer chain phase. a) α-phase with no dipole and b) β-phase with dipole moment [66].

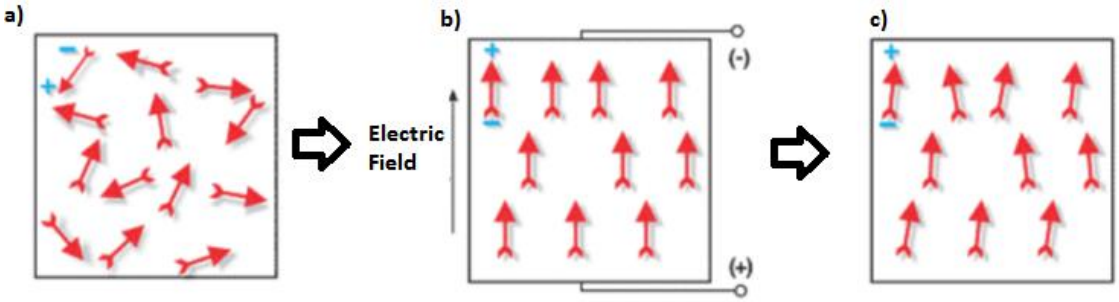

Figure 2.5. Polarizing of a piezoelectric ceramic. (a) Randomly oriented dipoles. (b) Aligned dipoles under strong electric field. (c) Permanently elongated polarization tendency [30].

Stretching PVDF film in uniaxial direction assists polymer chain alignment so that PVDF possesses high sensitivity in the stretched direction. Accordingly, the PVDF piezoelectric coefficient in the stretched direction (d_{31}) is higher than that in the transverse

direction (d_{32}). Typically, the piezoelectric coefficients of uniaxially stretched PVDF are d_{33}= -20-23 pC/N, d_{31}= 16 pC/N, and d_{32}= 3 pC/N [67]. Using biaxially or bi-equixially stretched PVDF or polymer blends such as polyvinylidene fluoride-trifluoroethylene (PVDF-TrFE) and polyvinylidene fluoride-chlolofluoroethylene (PVDF-CFE) [68] allows transversely isotropic piezoelectric properties; however, the obtainable piezoelectric coefficient is usually lower than uniaxially stretched PVDF and manufacturing process is rather complicated and costly than uniaxially stretched PVDF, which is mass-producible via roll-to-roll process. The piezoelectric coefficients for biaxially stretched PVDF are d_{33}= -20-25 pC/N, d_{31}= d_{32}= 5 pC/N, whereas the PVDF-TrFE exhibits slightly larger values of d_{33}= -24-33 pC/N, d_{31}= d_{32}= 7-10 pC/N [67, 69].

Humidity is another important parameter for manufacturing high-quality of PVDF films. Typically, PVDF film is cast from a PVDF-contained hydrophobic solvent. During the casting, the evaporation of the solvent may be slower than the intake of water vapor from humidified air, which causes phase separation and creates sub-micro size porous structures in PVDF film. Porous structures in the PVDF film is a serious impediment to deposit metals on both surfaces of the film. Thus, smooth surface PVDF membrane is desirable, which can be obtained under dry (~ 0 %) and relatively high temperature (>90 °C) conditions [70]. Temperature is also a key condition for PVDF chain phase transformation by stretching. As PVDF below 80 °C is fragile, PVDF ruptures when it is stretched more than 150 %; therefore, the transformation of chain phase below 80 °C is

challenging. Higher temperature increases chain directionality; however, the ratio of phase transformation from α to β becomes lower [71].

2.3 CHARACTERIZATION AND MEASUREMENT OF PVDF PARAMETERS

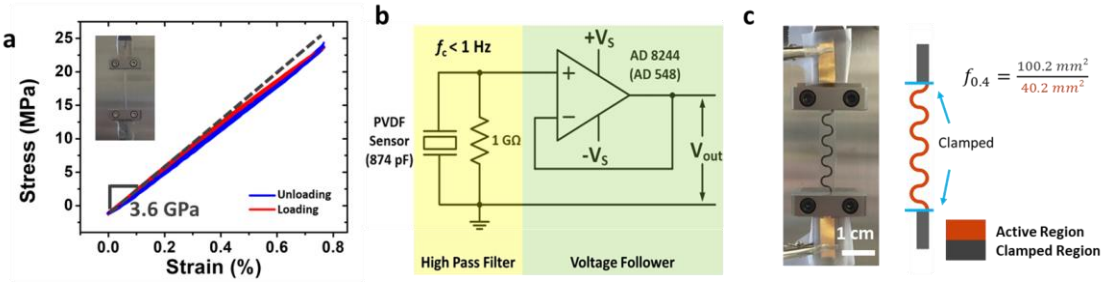

Figure 2.6. (a) A representative stress-strain curve of a straight PVDF ribbon. (b) A voltage follower circuit for piezoelectric sensors. (c) A photograph of a serpentine-shaped PVDF ribbon under the tensile test and an illustration of the voltage compensation factor *f*.

For actual devices, we purchased a 28.4-μm-thick PVDF film with 80 nm-thick Ni-Cu electrodes on the top and bottom surfaces (piezo film sheets, TE Connectivity). The in-plane stiffness and the strain sensitivity of the solid PVDF film are known as 2-4 GPa and 12 mV per micro-strain, respectively, according to the manufacturer data sheet [56]. Due to insufficient information in the datasheet of the commercial PVDF, we performed our own mechanical and electromechanical characterizations. The in-plane elastic stiffness constant (C_1) of PVDF was measured by uniaxial tensile tests using RSA-G2 digital mechanical analyzer (DMA). Two sets of freestanding straight PVDF ribbons of size 36 mm × 2.25 mm were prepared by cutting along the two orthogonal directions of the

commercial PVDF sheet. Each set, containing three ribbons, was subjected to five cycles of uniaxial loading-unloading up to a strain of 0.8% in a loading rate of 0.05 mm/s. The loading history of one of the ribbons is plotted in Fig. 2.6 (a). It was found that the measured moduli of all six specimens were similar, which confirmed that this commercial PVDF sheet is mechanically isotropic. The C_1 was obtained to be 3.60 ± 0.12 GPa from the slope of this curve.

To characterize the dielectric constant of the commercial PVDF sheet, we used an LCR meter (3532-50 LCR HiTESTER, HIOKI) and measured the capacitance of a 1 cm × 1 cm PVDF square to be 324 pF. Hence the capacitance per area is 324 pF/cm^2. According to the parallel-plate capacitance equation $C = \varepsilon A / h$, where h=28 μm is the thickness of the PVDF, we can calculate the out-of-plane permittivity (ε_3) of PVDF film to be 90.3 pF/m.

The piezoelectric coefficients (d_{31}, d_{32}) were measured by cyclic uniaxial tests. Two sets of straight PVDF ribbons cut in orthogonal direction to each other were prepared to validate the orthotropy in electromechanical properties. The piezoelectric coefficient can be obtained using the following equation:

$$d_{3j} \approx \frac{\varepsilon_3 V}{C_j h s_j} \tag{2.9}$$

where V is the output voltage cross the thickness of the PVDF corresponding to the applied strain s. Using an applied strain of ±0.2%, the output voltage was measured by a DAQ (NI-6225, National Instruments) via a voltage follower circuit (Fig 2.6 (b)) consists of an

operational amplifier (AD548, Analog Devices) with a high-input impedance and found to be 44.46 V after compensation. The measured mechano-electrical conversion sensitivity in stretched direction and transverse direction are to be 11.1 mV per micro-strain and 1.1 mV per micro-strain, respectively, which are close to the values given in the datasheet [56]. It is important to mention that when PVDF is uniaxially stretched during manufacturing process to increase its sensitivity, the sensitivity between the stretched direction and the transverse direction are different, while the material is yet mechanically isotropic under small strains [65]. Thus, d_{31} and d_{32} was computed to be 10 pC/N and 1pC/N, respectively, according to Eq. (2), which is very different from the value listed in the datasheet (23 pC/N) [56].We assume that the mismatch is derived from the difference of elastic stiffness measurement in the datasheet (C_1=2-4 GPa) and our experimental result (C_1=3.6 GPa). PVDF properties offered by the data sheet and measured by ourselves are compared in Table 2.1. Instead of using the properties offered by the data sheet, we used measured PVDF properties as the inputs in all our FEM jobs.

	Datasheet	Measured Value
In-plane stiffness C_{11} (GPa)	2 – 4	3.6
Capacitance per area (pF/cm²)	380	324
Out of plane relative permittivity	12 – 13	10.2
Piezo strain constant d_{31} (pC/N)	23	10
Voltage per μ-strain (mV)	12	11.1

Table 2.1. Comparison between the data sheet and actual measurement of piezofilm.

When presenting the output voltage, the clamped parts of the PVDF sample should be accounted for because $V_m = Q_a/(C_a + C_c)$, where V_m is the measured voltage, Q_a is the charge generated from the freestanding region, and C_a and C_c are the capacitance of the active (red colored in Figure 2.6 (c)) and the clamped (grey colored in Fig. 2.6 (c)) parts, respectively. To obtain the genuine output voltage from the active region, V_a, a compensation factor $f = (C_a + C_c)/C_a$ should be multiplied to V_m, i.e. $V_a = V_m(C_a + C_c)/C_a$. As the thickness and the relative permittivity of the active and clamped PVDF parts are identical (i.e. neglecting the clamping force induced thickness change), f can be simplified as $f = (A_a + A_c)/A_a$. From the given geometry of the straight PVDF ribbon and the FS PVDF vibration sensor, we calculated the compensation factors for each sample to be: f_{ST} = 2.49 and f_{FS} = 1.15.

2.4 APPLICATIONS

For its linear sensitivity, robustness and flexibility, PVDF has been used as a sensor in many biomedical and bio-integrated applications such as pacemaker activity sensors, apnea sensors, pressure sensors, and tactile sensors [72]. Moreover, the processability of polymer-based functional materials including PVDF allows devices to possess smart structures which enhance the sensitivity or robustness of the devices. For example, Zhou et al. created highly sensitive, self-powered wearable pressure sensor based on PVDF-fiber woven fabric [73]. As shown in Fig. 2.7 (a), the PVDF nanofiber coated with poly(3,4-ethylenedioxythiophene) (PEDOT) was drawn by electrospinning process, and then woven in a desired fabric shape, which is merely feasible for solid materials such as silicon or ceramic based materials. Due to nanofiber yarns and the woven structure, the sensor was stretchable up to 60 %, while showing the superior sensitivity (18.4 kPa^{-1}) at low pressure (2-100 Pa). The sensing performance and mechanical properties were sufficient to measure artery pulses at wrists (Fig. 2.7 (b) and (c)).

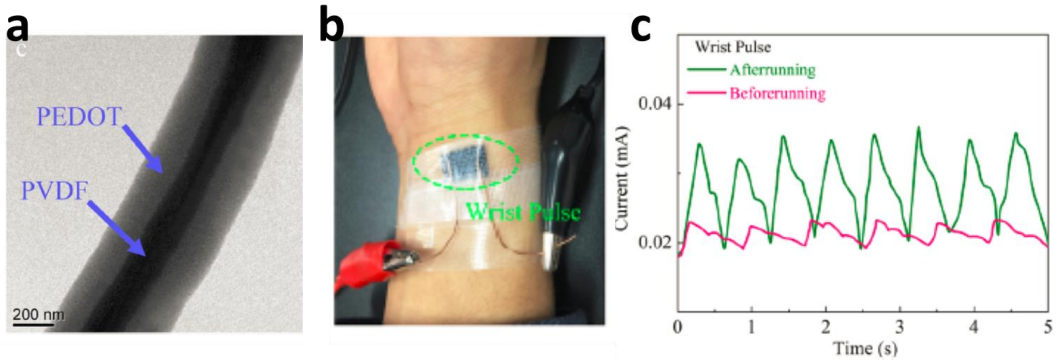

Figure 2.7. (a) Transmission Electron Microscopy image of PEDOT@PVDF nanofiber. (b) Photograph of the sensor on the wrist. (c) Monitoring wrist pulse before and after exercise.

Despite the low power conversion efficiency of PVDF, energy harvesters made of PVDF has been proposed for showing an excellent mechanical robustness comparable with human skin [39, 44]. For example, Duan et al. designed highly stretchable, skin-conformal PVDF nanogenerator [44]. Hundreds of PVDF nanofibers whose diameter is only few micrometers were patterned in self-similar serpentine shape on Ecoflex substrate by electrohydrodynamic printing. As described in Fig. 2.8 (a), the self-similar serpentine shape of patterned PVDF nanofibers and liquid metal connections embedded in Ecoflex substrate provides extremely high stretchability up to 200 %. The electrical output current of the device was up to 200 nA. Figure 2.8 (b) shows the energy harvesting performance of the device when it is on the wrist. As can be seen, PVDF can be applicable to stretchable, skin-conformal energy harvesting device due to its processability and mechanical robustness.

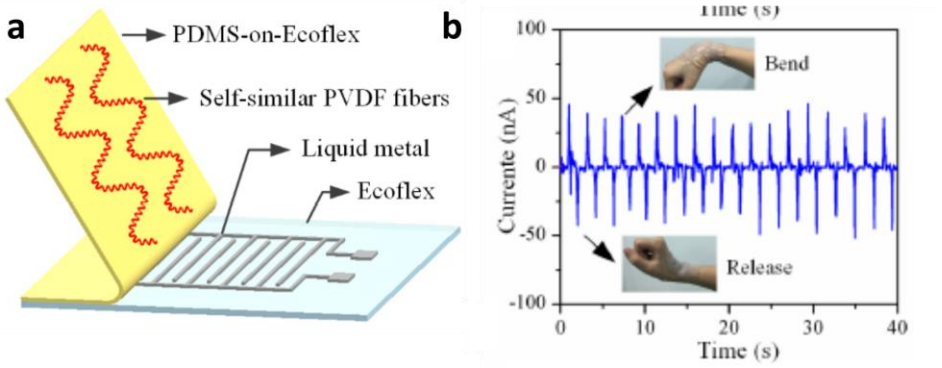

Figure 2.8. Ultra-stretchable piezoelectric nanogenerators fabricated by helix electrohydrodynamic printing. (a) Schematic of the nanogenerator. (b) Energy harvesting/sensing performance of the device when it conforms on the wrist.

Piezoelectric materials are applicable to electro-active devices such as speakers [74, 75], stacked actuators [76], linear motors [77], and ultrasonic motors [78] have also been developed based on the inverse piezoelectric effect. Although most conventional electro-active piezoelectric devices are using ceramic-based piezoelectric materials rather than piezoelectric polymers to achieve stronger propulsion and activation, bio-integrated electronics requires soft, bio compatible materials. Recently, a smart guide wire using polyvinylidene fluoride-trifluoroethylene-chlorotrifluoroethylene (PVDF-TrFE-CTFE) as an actuator has been developed by Ganet et al. [79]. As described in Fig. 2.9, a coaxial structure of PVDF-TrFE-CTFE wire is bidirectionally bendable in a certain degree with respect to the magnitude of applied electric field. Almost 90° of bending was observed

when 60V/μm of electric field was applied to the 65 mm-length PVDF-TrFE-CTFE fiber with 1.4 mm diameter. The suggested material and structure may be an outstanding candidate for endovascular navigation.

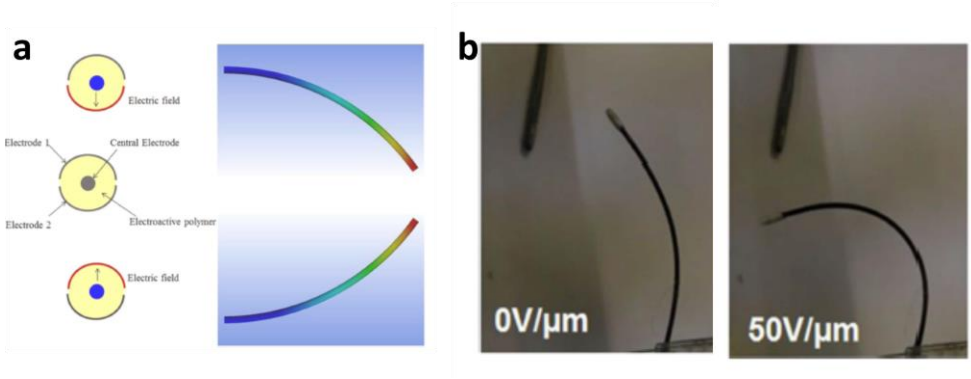

Figure 2.9. Smart guide wire based on PVDF copolymer. (a) bidirectionally bendable actuator. (b) Actuation of real device.

Chapter 3: Thickness Ratio and d33 Effects on Flexible Piezoelectric Unimorph Energy Conversion[1]

Piezoelectric unimorphs are bilayer structures where a blanket piezoelectric film (with top and bottom electrodes) is uniformly laminated on an inactive but flexible substrate. Here we report a comprehensive theoretical framework to investigate the effects of the film-to-substrate thickness ratio on voltage, charge, and energy outputs when the unimorph is subjected to eight different boundary/loading conditions. We show that the analytical and finite element modeling (FEM) results are in excellent agreement. Non-monotonic dependence of voltage and energy generation on thickness ratio has been found in some cases and optimum thickness ratio for unimorph generator can be predicted. When the unimorph is actuated by voltage applied across the piezo-film thickness, non-monotonic maximum deflection versus thickness ratio is also found.

---

[1] T. Ha, J.X.J. Zhang, and N. Lu*. "Thickness ratio and d 33 effects on flexible piezoelectric unimorph energy conversion." Smart Materials and Structures 25.3 (2016): 035037.

Author contributions: T. Ha conducted the numerical and theoretical analysis. J.X.J Zhang and N. Lu supervised and coordinated the project. T. Ha and N. Lu wrote the paper.

3.1 INTRODUCTION

Piezoelectric materials convert electrical pulses from or to mechanical vibrations [28]. Such electromechanical energy conversion is ubiquitous in both inorganic materials and biological systems. Piezoelectric materials in nature can be ceramic or polymeric: ceramic piezoelectric materials including lead zirconate titanate (PZT) [80], zinc oxide (ZnO) [81], barium titanate (BTO) [82] are known to have large intrinsic piezoelectric coefficients but they are mechanically stiff and brittle. Polymeric piezoelectric materials such as polyvinylidene fluoride (PVDF) [24] and porous electromechanical film (EMFi) [25] are intrinsically more compliant, but their piezoelectric coefficients are one order smaller than those of the ceramic ones [26]. Both kinds of piezoelectric materials have found wide applications in sensing, actuation, and energy harvesting [83] because of their unique combination of mechanical form factors and energy transduction capabilities.

Mechanical energy from nature, machines, and human body provides an excellent alternative as clean, non-depletable power sources. Many ambient sources of mechanical energy, including wind [84], water flow [85], and human motion [86], have been collected by piezoelectric devices. With the emergence of wearable electronics and bio-integrated electronics [87], flexible and stretchable generators that can harvest power from the natural processes of the body such as the vibration of muscles, lungs, and heart have attracted growing interest [88]. Examples include ZnO nanowire based nanogenerators [89], buckled PZT nanoribbon based stretchable biocompatible energy harvester [90], and BTO [91] and ZnO [32] thin film based bendable nanogenerators, as well as PVDF based nanogenerators

and biosensors [92-95]. Although the power generated is usually on the order of microwatts to milliwatts, which may not be sufficient to power most wearable or implantable devices, the generators can at least be used to recharge batteries.

Theoretical models for piezoelectric energy harvesters are widely available in the literature [96-99]. Two major threads of energy harvesting optimization theories are resonance frequency analysis and structural analysis. As mechanical activities of human body exhibit low frequency (1-30 Hz) [100], resonance frequency optimization is less relevant here. Instead, structural optimization becomes an important problem due to the dimensional confinement imposed by curvilinear and deformable human body and organs [101]. Constituent equations for a cantilever unimorph under static conditions have been established by Smits and Choi [97]. Using those equations, the effects of thickness ratio and elastic mismatch of a cantilever unimorph have been theoretically investigated by Wang et al. [96], who found non-monotonic relationship between thickness ratio and electrical outputs. Subsequently, several numerical studies on the effect of thickness ratio of unimorphs have been reported [102-104].

Existing unimorph models [96, 97, 105] are mostly limited to cantilever configurations and the d_{33} contribution has been neglected because σ_3 is always assumed to be zero. However, unimorphs can also operate under the boundary conditions of pure bending or simple-simple support and can be subjected to variety types of load or displacement excitations. Moreover, σ_3 is non-zero for thick unimorphs and may have significant contributions to the outputs. To find a remedy for aforementioned deficiencies, we derive closed-form

solutions for unimorphs in eight different boundary/loading conditions. To validate our theory, finite element modeling (FEM) was performed using COMSOL Multiphysics. Non-monotonic electrical outputs versus thickness ratio curves are found for several boundary value problems (BVP). To resolve the discrepancy between theoretical and FEM results for some scenarios, the d_{33} effect had to be taken into consideration. Simple models to determine average σ_3 along beam length has been proposed and turn out to be very effective in accounting for the d_{33} contribution. The d_{33} effect is found to be more significant as piezo-layer thickness increases. When simple-simple and cantilever unimorphs are subjected to voltage excitation, non-monotonic deflection vs. thickness ratio curves are obtained and the d_{33} effect is also revealed. Overall, this work provides new physical insights on flexible unimorphs and analytical solutions that can be used for the structural optimization of unimorphs under different boundary/loading conditions.

3.2 METHOD

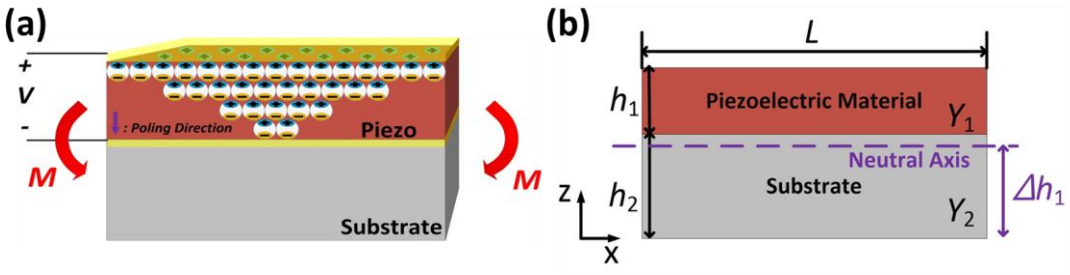

Figure 3.1. (a) A schematic of a unimorph generator. When subjected to bending moment, the polarization density varies linearly along the thickness direction. (b) Illustration of basic variables: the thickness of the piezo-layer and the polymer substrate is h_1 and h_2, respectively, the Young's modulus is Y_1 and Y_2, respectively, and the length of the unimorph is labeled as L. The neutral axis of the bilayer is located Δh_1 away from the bottom of the substrate, where Δ is a dimensionless parameter given in Eq. (3.1).

Figure 3.1 (a) is the schematic of a piezoelectric unimorph generator with the piezoelectric layer poled downward. When a bending moment is applied to this unimorph as illustrated in Fig. 3.1 (a), a dielectric polarization in the same direction as the poling direction will be induced by the bending deformation of the piezoelectric layer. Suppose the piezoelectric layer and the substrate have thicknesses of h_1 and h_2 and Young's moduli of Y_1 and Y_2, as labeled in Fig. 3.1 (b), calculating the voltage, charge, and power output of such a unimorph first requires the determination of the neutral axis and the effective second moment of inertia of the bilayer. The distance from the neutral axis to the bottom surface

of the substrate is represented by Δh_1, as labeled in Fig. 3.1 (b), where Δ has been given by [106]

$$\Delta = \frac{1 + 2\Sigma\eta + \Sigma\eta^2}{2\eta(1 + \Sigma\eta)}, \tag{3.1}$$

where $\Sigma = \bar{Y}_1/\bar{Y}_2$ is the film-to-substrate modulus ratio with $\bar{Y} = Y/(1 - \nu^2)$ being the plane strain modulus, Y being the Young's modulus, ν being the Poisson's ratio, and $\eta = h_1/h_2$ is the film-to-substrate thickness ratio.

The effective second moment of inertia of the bilayer is given by [106]

$$I = Wh_2^3 \left\{ \Sigma \left[\eta(\Delta\eta - 1)^2 - \eta^2(\Delta\eta - 1) + \frac{\eta^3}{3} \right] + \Delta\eta(\Delta\eta - 1) + \frac{1}{3} \right\} = Wh_2^3 \bar{I}, \tag{3.2}$$

where W is the width of structure, $\bar{I}$ represents the non-dimensional second moment of inertia and hence the bending stiffness of the unimorph can be written as $\bar{Y}_2 I$. As we assume the given problem is a plain strain problem, W is considered to be 1. For given piezoelectric and substrate materials (i.e., Σ fixed), the only dimensionless variable in the problem is the thickness ratio η, whose effect is the focus of this study.

For eight different boundary/loading conditions, solutions have been obtained through both 2D plane strain linear piezoelectric theory and FEM. Before describing the theory, the material parameters and model setup in the commercial FEM software, COMSOL Multiphysics 4.4, are summarized here. We choose Kapton as a representative inactive flexible substrate material with Young's modulus of 2.5 GPa, Poisson's ratio of 0.34, and mass density of 1420 kg/m^3, assuming it is isotropic [107] . For the piezoelectric

layer, we choose poly(vinylidene fluoride-co-trifluoro ethylene) (PVDF-TrFE) because of its popularity and mechanical robustness. Furthermore, PVDF-TrFE (75/25) has well-established experimental data of mass density (1879 kg/m^3 [108]), elastic compliance, relative permittivity, and piezoelectric coefficients [69]:

-Elastic Compliance Tensor

$$s^E = \begin{bmatrix} 3.32 & -1.44 & -0.89 & 0 & 0 & 0 \\ -1.44 & 3.24 & -0.86 & 0 & 0 & 0 \\ -0.89 & -0.86 & 3.00 & 0 & 0 & 0 \\ 0 & 0 & 0 & 94.0 & 0 & 0 \\ 0 & 0 & 0 & 0 & 96.3 & 0 \\ 0 & 0 & 0 & 0 & 0 & 14.4 \end{bmatrix} \times 10^{-10} Pa^{-1}, \tag{3.3}$$

where $Y_1 = 1/s_{11}$ and $v_1 = -s_{13}/s_{11}$ are found to be 3GPa and 0.268, respectively.

-Permittivity Matrix

$$\varepsilon^T = \begin{bmatrix} 7.4 & 0 & 0 \\ 0 & 7.95 & 0 \\ 0 & 0 & 7.9 \end{bmatrix} \times \varepsilon_0, \tag{3.4}$$

where $\varepsilon_0 = 8.85\times10^{-12}$ F/m is the vacuum permittivity. Hence the relative permittivity in the thickness direction is $\varepsilon_{\mathrm{p}} = 7.9$.

-Piezoelectric Coupling Tensor

$$d = \begin{bmatrix} 0 & 0 & 0 & 0 & -36.3 & 0 \\ 0 & 0 & 0 & -40.6 & 0 & 0 \\ 10.7 & 10.1 & -33.5 & 0 & 0 & 0 \end{bmatrix} \times 10^{-12} C \cdot N^{-1}. \tag{3.5}$$

When the film is fixed to be PVDF-TrFE and the substrate to be Kapton, then the elastic mismatch $\Sigma = \bar{Y}_1/\bar{Y}_2$ is fixed to be 1.148. To study the effect of the film-to-

substrate thickness ratio, the Kapton thickness is fixed to be 25 μm whereas the thickness of PVDF-TrFE varies from 0.5 μm to 20 μm with an incremental step of 0.5 μm. While the mechanical boundary conditions vary from case to case, the electrostatic boundary conditions remain the same for all eight cases of generators in the following section. The top surface of the piezo-layer is set as the ground and voltage is collected and averaged at the bottom of the piezo-layer. The absolute value of charge on top and bottom surfaces are collected and averaged to yield the total charge. All other boundaries are set to zero charge. When meshing the model in COMSOL, we selected "mapped mesh" method with the maximum element size of 0.5 μm and the minimum element size of 0.01 μm.

3.3 RESULTS

3.3.1 Constant Moment Bending

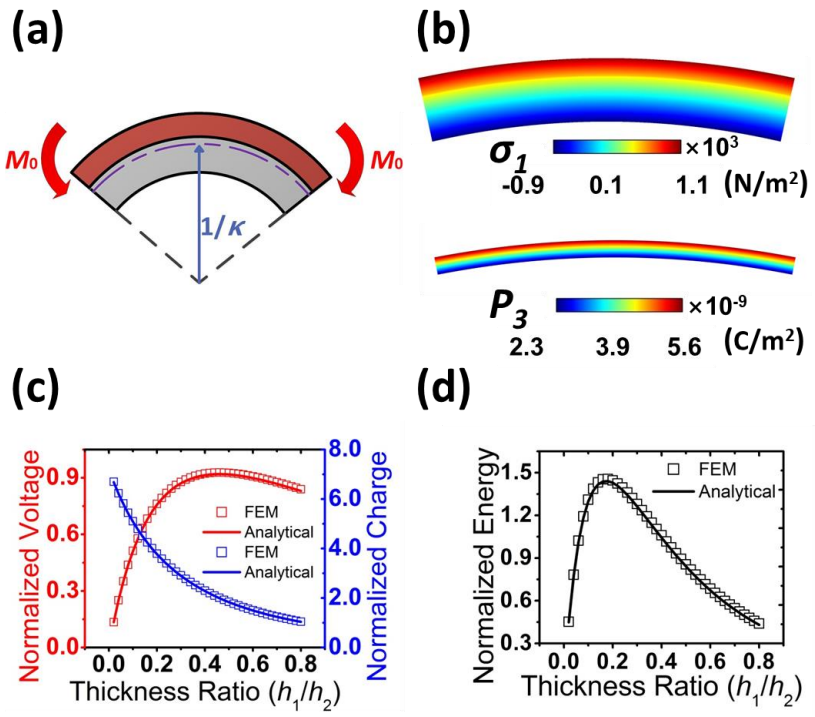

Figure 3.2. (a) A schematic for the pure bending with constant bending moment (PB-M) case. (b) FEM results of σ_1 and P_3 when $M_0 = 1\times10^{-7}$ N·m. (c) The analytical (curves) and FEM (markers) results of normalized voltage and charge density as functions of the thickness ratio ($\eta = h_1/h_2$). (d) The analytical and FEM results of normalized energy density as a function of the thickness ratio.

Figure 3.2 (a) illustrates the boundary and loading conditions of a unimorph subjected to pure bending under constant bending moment M_0 (PB-M). Based on Euler-Bernoulli beam theory, the only non-zero stress component in this unimorph will be bending induced normal stress in *x* direction and its vertical distribution is given by

$$\sigma_1 = \frac{M_0(z-\Delta h_1)}{h_2^{\,3}}\frac{\Sigma}{\bar{I}}, \tag{3.6}$$

where Δ is given in Eq. (3.1) and $\bar{I}$ in Eq. (3.2). The subscript 1 in σ denotes *x* direction and 3 will be used to denote *z* direction, where *x* and *z* directions are defined in Fig. 3.2 (b). Based on the linear piezoelectric theory [109], deformation induced polarization density is proportional to stress through the piezoelectric coefficient, i.e. $P_{\mathrm{i}} = d_{\mathrm{ij}}\sigma_{\mathrm{j}}$ ($\mathrm{i} = 1,2,3,\ \mathrm{j} = 1,2,\ldots,6$), therefore *z* direction polarization density is given by

$$P_3 = \frac{d_{31}M_0(z-\Delta h_1)}{h_2^{\,3}}\frac{\Sigma}{\bar{I}}. \tag{3.7}$$

Since charges are only collected from the top and bottom surface electrodes of the piezo-layer, only top ($z = h_1 + h_2$) and bottom ($z = h_2$) surface polarization density will be considered to calculate the total amount of charges.

As the total amount of charges and polarization density are related through $Q = -\int \bar{a}_{\mathrm{n}} \cdot \bar{P}\mathrm{d}S$, where $\bar{a}_{\mathrm{n}}$ stands for the surface normal vector and *S* stands for the overall surface area ($S = L$ in our plane strain model), the effective charge output, which is defined as $Q_{\mathrm{PB-M}} = (|Q_{\mathrm{Top}}| + |Q_{\mathrm{Bot}}|)/2$ can be expressed as

$$Q_{PB-M} = \frac{d_{31} L M_0}{h_2^{\,2}} \left[\frac{\Sigma}{\bar{I}} \left(1 + \frac{\eta}{2} - \Delta\eta \right) \right]. \tag{3.8}$$

Therefore, surface charge density can be readily given by $\rho = Q/S$, i.e.

$$\rho_{PB-M} = \frac{d_{31} M_0}{h_2^{\,2}} \left[\frac{\Sigma}{\bar{I}} \left(1 + \frac{\eta}{2} - \Delta\eta \right) \right]. \tag{3.9}$$

Through the definition of capacitance $C = Q/V$, voltage is given by $V = Q/C$ where $C = \varepsilon_p' L/h_1$, with ε_p' being the effective permittivity of the piezoelectric material [97]:

$$\varepsilon_p' = \varepsilon_p \left\{ 1 \pm \frac{d_{31}^{\,2}}{6\bar{Y}_1 \varepsilon_p} \left(\frac{\Sigma\eta^3 + 1}{\eta + 1} \right) \left(1 + \frac{\eta}{2} - \Delta\eta \right) \frac{1}{\bar{I}} \right\}, \tag{3.10}$$

where the sign depends on the poling direction. Hence the output voltage is given by

$$V_{PB-M} = \frac{d_{31} M_0}{\varepsilon_p' h_2} \left[\frac{\Sigma\eta}{\bar{I}} \left(1 + \frac{\eta}{2} - \Delta\eta \right) \right]. \tag{3.11}$$

Finally the generated energy density can be calculated by $U = \rho V/2$, i.e.

$$U_{PB\_M} = \frac{1}{2} \frac{d_{31}^{\,2} M_0^{\,2}}{\varepsilon_p' h_2^{\,3}} \left[\eta \left(\frac{\Sigma}{\bar{I}} \right)^2 \left(1 + \frac{\eta}{2} - \Delta\eta \right)^2 \right]. \tag{3.12}$$

It is obvious from Eqs. (3.9)-(3.12) that when film and substrate materials are fixed, i.e. when Σ is fixed, dimensionless ρ, V, and U will just depend on the thickness ratio, η, which will be plotted together with FEM results.

Our FEM model implements the pure bending condition as illustrated by Fig. 3.2 (a) with the substrate being Kapton, piezoelectric layer being PVDF-TrFE and with fixed

h_2 = 25 μm and $M_0 = 1\times10^{-7}$ N·m, which is estimated from the change of heart curvature during heart beat [110, 111] times the bending stiffness of the unimorph. Bending moment was applied on each side wall of the beam through the boundary condition named "rigid connector".The FEM contour plots of stress and polarization density are given in Fig. 3.2 (b) with h_1 = 10 μm. Both stress and polarization density vary linearly with *z*, as predicted by Eqs. (3.7) and (3.8). Charge and voltage can also be directly output from FEM and $U = \rho V/2$ is used to calculate the FEM output of electrical energy density.

Analytical and FEM results are compared in Figs. 3.2 (c) and (d). Excellent overlap between Eqs. (3.9) & (3.11) and FEM results demonstrates a strong validation of our linear piezoelectric theory for unimorphs even without accounting for the d_{33} effect in the formulation (d_{33} is included in FEM). The biggest mismatch between FEM results and Eq. (3.11) in Fig. 3.2 (c) is less than 1.8%, which occurs at the largest η. The mismatch is due to the breakdown of Bernoulli's beam theory: when L and h_2 are fixed and h_1 is increased to increase η, the overall unimorph thickness-to-length ratio increases and σ_3 can no longer be assumed zero. This effect is more pronounced in cantilever and simply supported unimorphs and will be specifically discussed later. It is interesting to see that while the charge density monotonically decays as the piezo-film gets thicker, the voltage output is non-monotonic, with the peak value reached at η = 0.46. This is due to the trade-off that under constant moment, increasing h_1 will enlarge both distance from neutral axis, which enhances the voltage output, and second moment of inertia, which diminishes the voltage output. Normalized energy density is plotted in Fig. 3.2 (d). The optimized thickness ratio

for maximum energy output is η = 0.18, which is different from the optimal η with maximum voltage output. Therefore, choosing the optimum thickness ratio depends on whether maximum voltage output or energy density is desired.

3.3.2 Constant Curvature Bending (PB-κ)

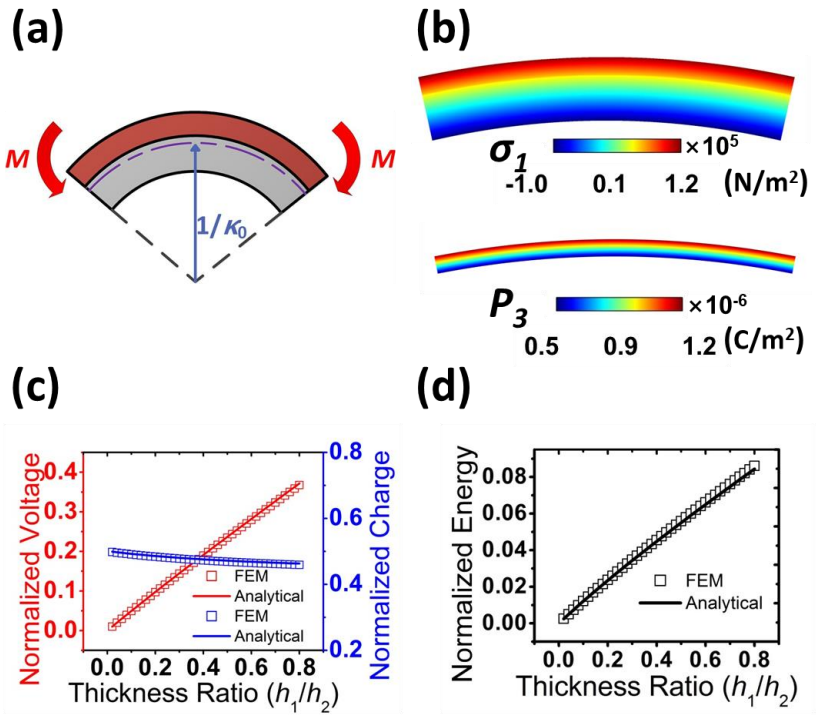

Figure 3.3. (a) A schematic for the pure bending with constant bending curvature (PB-κ) case. (b) FEM results of σ_1 and P_3 when κ_0 = 2 m^{-1}. (c, d) The analytical and FEM results of normalized voltage, charge density, and energy density as functions of the thickness ratio.

Figure 3.3 shows the FEM and analytical solutions for the unimorph subjected to pure bending with constant curvature κ_0 (PB-κ). Following the same way of 3.3.1 and directly substituting $M_0 = \kappa_0 \bar{Y}_2 h_2^3 \bar{I}$ into Eqs. (3.9) and (3.11), analytical expressions for the charge density and the voltage output under PB-κ are

$$\rho_{PB-\kappa} = d_{31} \overline{Y}_1 \kappa_0 h_2 \left(1 + \frac{\eta}{2} - \Delta\eta \right) \tag{3.13}$$

and

$$V_{PB-\kappa} = \frac{d_{31} \overline{Y}_1 \kappa_0 h_2^{\,2}}{\varepsilon_p'} \left[\eta \left(1 + \frac{\eta}{2} - \Delta\eta \right) \right], \tag{3.14}$$

respectively. Figure 3.3 (b) shows the FEM results of σ_1 and P_3 where the piezo-layer is 10 μm thick and κ_0 is fixed as 2 m^{-1}.

Figure 3.3 (c) shows the normalized voltage and charge density under the PB-κ condition. While the charge density monotonically decays with increasing η, which is similar to the PB-M result, the voltage output increases with increasing η, which is very different from the PB-M result. This is because under constant curvature, the second moment of inertia no longer shows up in the denominator of the voltage equation. Figure 3.3 (d) plots the normalized electrical energy density ($U = \rho V/2$) generated under the PB-κ condition, which monotonically increases with η.

3.3.3 Cantilever Bending

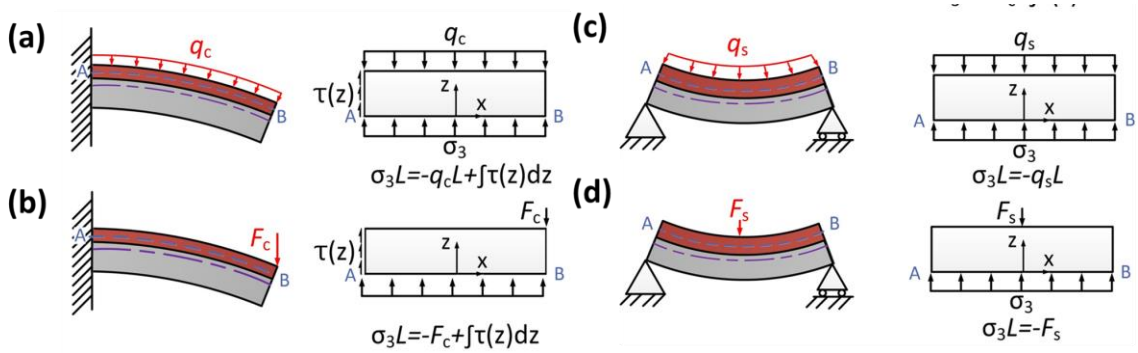

Figure 3.4. Schematics and free body diagrams for calculating average σ_3 in cantilever and simply supported unimorphs: (a) Cantilever unimorph subjected to uniformly distributed load (C-Q case) where shear stress applied by the left wall has a parabolic distribution. (b) Cantilever unimorph subjected to point load (C-F case) where shear stress applied by the left wall also has a parabolic distribution. (c) Simply supported unimorph subjected to uniformly distributed load (SS-Q case) where $\sigma_3 = -q_s$. (d) Simply supported unimorph subjected to point load (SS-F case) where $\sigma_3 = -F_s/L$.

While working on cantilever and simply supported unimorphs, we realized that unlike unimorphs subjected to pure bending, there is non-zero σ_3 in cantilever and simply supported unimorphs. Since σ_3 generates additional P_3 through d_{33}, it is important to account for its contribution when analyzing cantilever and simply supported unimorphs. Figure 3.4 (a) left panel depicts a cantilever unimorph subjected to uniformly distributed load (the C-Q condition). A free body diagram is drawn on the right panel when we make

a cut along Line AB. It is clear that the applied distributed load has to be balanced by the reaction shear force applied by the wall and the normal force on the AB plane. Let σ_3 be the average normal stress on the AB plane, the force balance equation is hence established in the bottom of the free body diagram. Since the shear stress is parabolically distributed along the left surface as

$$\tau(z) = q_c L / (2h_2 \bar{I}) \cdot \left[\left(1 + \eta - \Delta\eta\right)^2 - \left(z / h_2 - \Delta\eta\right)^2 \right], \tag{3.15}$$

σ_3 is a function of z.

Figure 3.4 (b) illustrates the case where a cantilever unimorph is subjected to point load at the end (the C-F condition). Similar to the C-Q condition, the applied point load is fully balanced by the reaction shear force applied by the wall and the normal force on the AB plane. Again, the average normal stress σ_3 on the AB plane can be calculated by the force balance equation in the bottom of the free body diagram where $\tau(z)$ is simply given by Eq. (3.15) with $q_c L$ replaced by F_c.

Similarly, for simply supported unimorphs subjected to uniformly distributed load (SS-Q condition) and point load at the center (SS-F condition), Figs. 3.4 (c) and (d) offer the free body diagrams that help determine the average σ_3 along the AB plane, both of which are constants, which is different from the cantilever unimorphs.

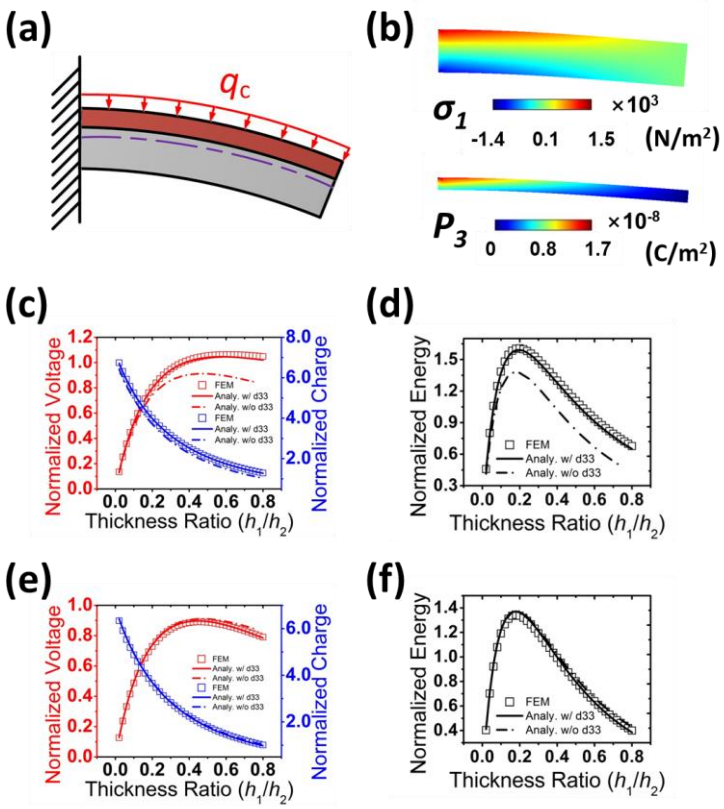

Figure 3.5. (a) A schematic for the cantilever unimorph subjected to uniformly distributed load (C-Q case). (b) FEM results of σ_1 and P_3 when q_c = 15 N/m. (c, d) The analytical and FEM results of normalized voltage, charge density, and energy density as functions of the thickness ratio. Dash-dot curves do not account for d_{33} effects whereas solid curves do. (e, f) The analytical and FEM results of normalized voltage, charge density, and energy density as functions of the thickness ratio when the piezo-layer and substrate are flipped. Dash-dot curves do not account for d_{33} effects whereas solid curves do.

The expression for the moment distribution in C-Q condition is

$$M(x) = \frac{q_c(L^2 - 2Lx + x^2)}{2}, \tag{3.16}$$

where the q_c is the distributed load per unit length, as labeled in Fig. 3.5 (a). The charge density and voltage output can be derived following the same procedure outlined in the previous section:

$$\rho_{C-Q} = \frac{d_{31} q_c L^2}{6 h_2^{\,2}} \left[\frac{\Sigma}{\bar{I}} \left(1 + \frac{\eta}{2} - \Delta\eta \right) \right] \tag{3.17}$$

and

$$V_{C-Q} = \frac{d_{31} q_c L^2}{6 \varepsilon_p' h_2} \left[\frac{\Sigma\eta}{\bar{I}} \left(1 + \frac{\eta}{2} - \Delta\eta \right) \right], \tag{3.18}$$

respectively, where the contribution of σ_3 is not yet considered. Comparing Eq. (3.17) with Eq. (3.9) and Eq. (3.18) with Eq. (3.11), simply substituting $M_0 = q_c L^2/6$ can readily convert the PB-M solution to the C-Q solution. But in the C-Q solution, L is a new variable that does not exist in the PB-M solution.

Figure 3.5 (b) shows the FEM contour plots of σ_1 and P_3 when the piezo-layer thickness is 10 μm under the C-Q condition and d_{33} is included. The uniformly distributed load is chosen such that the average moment in the C-Q condition $M = q_c L^2/6$ equals to the moment applied in the PB-M condition. When we plot Eqs. (3.17) and (3.18) as dash-dot line against FEM results as shown in Fig. 3.5 (c), a clear mismatch can be observed, especially when h_1/h_2 is large. This is because the polarization density due to non-zero σ_3 was not accounted for. According to the equilibrium equation given in Fig. 3.4 (a), average σ_3 in the C-Q condition can be expressed as

$$\sigma_3 = -q_c \left\{ 1 - \frac{1}{\bar{I}} \left[\frac{1}{3}(1+\eta-\Delta\eta)^3 - \frac{1}{2}(1+\eta-\Delta\eta)^2 \left(\frac{z}{h_2} - \Delta\eta \right) + \frac{1}{6} \left(\frac{z}{h_2} - \Delta\eta \right)^3 \right] \right\}. \quad (3.19)$$

Subsequently, the polarization density induced by σ_3 through the d_{33} coefficient is

$$P_{3\_d_{33}} = -d_{33} q_c \left\{ 1 - \frac{1}{\bar{I}} \left[\frac{1}{3}(1+\eta-\Delta\eta)^3 - \frac{1}{2}(1+\eta-\Delta\eta)^2 \left(\frac{z}{h_2} - \Delta\eta \right) + \frac{1}{6} \left(\frac{z}{h_2} - \Delta\eta \right)^3 \right] \right\}. \quad (3.20)$$

Note d_{33} for PVDF-TrFE is a negative value as given in Eq. (3.5).

Finally, the total charge density and voltage output induced by both σ_1 and σ_3 in the C-Q case are

$$\rho'_{C-Q} = \frac{d_{31} q_c L^2}{6 {h_2}^2} \left\{ \frac{\Sigma}{\bar{I}} \left[\left(1 + \frac{\eta}{2} - \Delta\eta \right) - \frac{d_{33}}{d_{31}} \left(\frac{h_2}{L} \right)^2 \left(\frac{12\bar{I} - \eta^2(3 + 2\eta - 3\Delta\eta)}{2\Sigma} \right) \right] \right\} \quad (3.21)$$

and

$$V'_{C-Q} = \frac{d_{31} q_c L^2}{6 \varepsilon_p' h_2} \left\{ \frac{\Sigma\eta}{\bar{I}} \left[\left(1 + \frac{\eta}{2} - \Delta\eta \right) - \frac{d_{33}}{d_{31}} \left(\frac{h_2}{L} \right)^2 \left(\frac{12\bar{I} - \eta^2(3 + 2\eta - 3\Delta\eta)}{2\Sigma} \right) \right] \right\}, \quad (3.22)$$

respectively. Note that in both equations the d_{33} term diminishes as the length of the unimorph increases. Plotting Eqs. (3.21) and (3.22) as solid curves in Fig. 3.5 (c) and $U = \rho' V'/2$ as a solid curve in Fig. 3.5 (d), they have found excellent agreement with the FEM results, until again when h_1 is too large for the beam theory to stay valid as discussed before. The optimal η for the voltage and the energy density are 0.58 and 0.2, respectively. The optimal η for the voltage is slightly shifted compared to PB-M case because of the additional contribution from σ_3.

Figures 3.5 (e) and (f) show the normalized electrical outputs when the boundary and loading conditions stay the same but the piezo-film and the substrate switch position. In this case piezo-layer is still Layer 1 and substrate is still Layer 2, and Σ, η and Λ given by Eq. (3.1) stay the same. In this case the piezo-layer is located below the neutral axis so the sign of σ_1 is changed. The σ_3 equation in Fig. 3.4 (a) is still valid but as the shear force term is larger than the piezo-layer-on-substrate case, the σ_3 is smaller in the substrate-on-piezo-layer case. As a result, the σ_3 contribution will be a smaller effect and it will counteract the σ_1 contribution, as evidenced in Figs. 3. 5(e) and (f). The optimal η for maximum voltage and energy density outputs are 0.44 and 0.18, respectively.

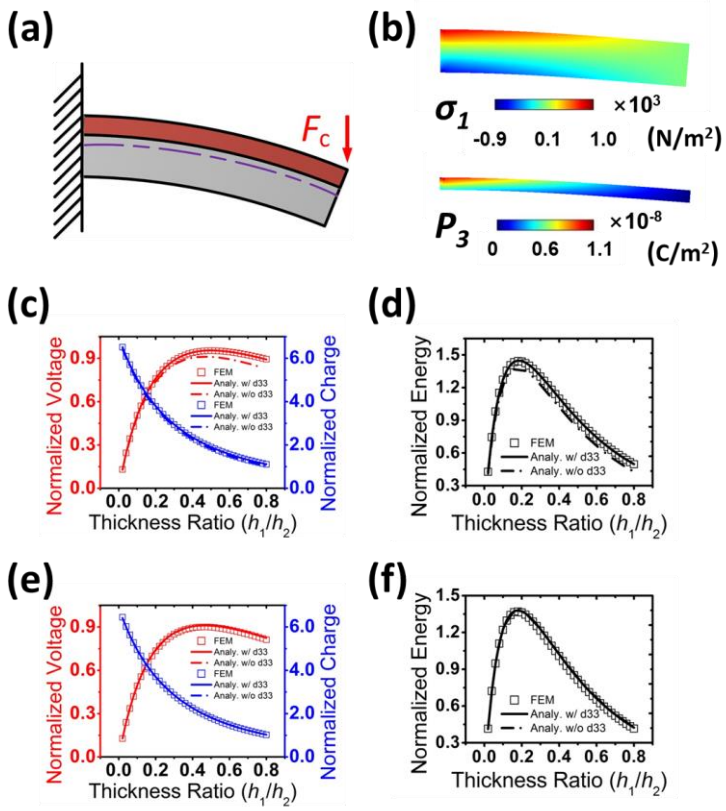

Figure 3.6. (a) A schematic for the cantilever unimorph subjected to point load (C-F case). (b) FEM results of σ_1 and P_3 when F_c = 1 mN. (c, d) The analytical and FEM results of normalized voltage, charge density, and energy density as functions of the thickness ratio. Dash-dot curves do not account for d_{33} effects whereas solid curves do. (e, f) The analytical and FEM results of normalized voltage, charge density, and energy density as functions of the thickness ratio when the piezo-layer and substrate positions are flipped. Dash-dot curves do not account for d_{33} effects whereas solid curves do.

Point load is an easily achievable loading condition in experiment. As depicted in Fig. 3.6 (a), a point load (F_c) is applied at the end of the cantilever unimorph. The moment distribution in the cantilever can be expressed by

$$M(x) = F_c(L - x). \tag{3.23}$$

After averaging Eq. (3.23) over L and substituting the result $F_cL/2$ into M_0 in Eq. (7), the charge density and the voltage output without accounting for σ_3 contribution can be readily obtained as

$$\rho_{C-F} = \frac{d_{31}F_cL}{2h_2^{\,2}}\left[\frac{\Sigma}{\bar{I}}\left(1+\frac{\eta}{2}-\Delta\eta\right)\right] \tag{3.24}$$

and

$$V_{C-F} = \frac{d_{31}F_cL}{2\varepsilon_p{}'h_2}\left[\frac{\Sigma\eta}{\bar{I}}\left(1+\frac{\eta}{2}-\Delta\eta\right)\right]. \tag{3.25}$$

But as illustrated in Fig. 3.4 (b), the C-F case has nonzero σ_3, Based on the equation given in Fig. 3.4 (b), σ_3 and the resulted polarization in the C-F condition are given by

$$\sigma_3 = -\frac{F_c}{L}\left\{1-\frac{1}{\bar{I}}\left[\frac{1}{3}\left(1+\eta-\Delta\eta\right)^3-\frac{1}{2}\left(1+\eta-\Delta\eta\right)^2\left(\frac{z}{h_2}-\Delta\eta\right)+\frac{1}{6}\left(\frac{z}{h_2}-\Delta\eta\right)^3\right]\right\} \tag{3.26}$$

and

$$P_{3\_d_{33}} = -d_{33}\frac{F_c}{L}\left\{1-\frac{1}{\bar{I}}\left[\frac{1}{3}\left(1+\eta-\Delta\eta\right)^3-\frac{1}{2}\left(1+\eta-\Delta\eta\right)^2\left(\frac{z}{h_2}-\Delta\eta\right)+\frac{1}{6}\left(\frac{z}{h_2}-\Delta\eta\right)^3\right]\right\}, \tag{3.27}$$

respectively. The total charge density and voltage output induced by both σ_1 and σ_3 in the C-F case are therefore

$$\rho'_{C-F} = \frac{d_{31}F_cL}{2h_2^2}\left\{\frac{\Sigma}{\bar{I}}\left[\left(1+\frac{\eta}{2}-\Delta\eta\right)-\frac{d_{33}}{d_{31}}\left(\frac{h_2}{L}\right)^2\left(\frac{12\bar{I}-\eta^2(3+2\eta-3\Delta\eta)}{6\Sigma}\right)\right]\right\} \quad (3.28)$$

and

$$V'_{C-F} = \frac{d_{31}F_cL}{2\varepsilon_p' h_2}\left\{\frac{\Sigma\eta}{\bar{I}}\left[\left(1+\frac{\eta}{2}-\Delta\eta\right)-\frac{d_{33}}{d_{31}}\left(\frac{h_2}{L}\right)^2\left(\frac{12\bar{I}-\eta^2(3+2\eta-3\Delta\eta)}{6\Sigma}\right)\right]\right\}. \quad (3.29)$$

Figure 3.6 (b) shows the FEM results of σ_1 and P_3 when the piezo-film is 10 μm thick and the averaged moment equals to the M_0 used in the PB-M case. To reduce the singularity error of FEM, the point load is located $L/200$ away from the end edge of the cantilever because if the point load is applied exactly on the end edge of the unimorph, the COMSOL Multiphysics only applies half of the load to the unimorph. This technique of leaving a small margin towards the end is also applied to other FEM simulations which have loadings applied up to the edge, including distributed loads and applied displacement.

The comparison between FEM and analytical solution is made in Figs. 3.6 (c) and (d). The good agreement also validates our rationale that there is σ_3 contribution in C-F case. Comparing Figs. 3.5(c) and (d) with Figs. 3.6 (c) and (d), it is concluded that the d_{33} effect on the electrical outputs of C-Q is greater than that of C-F. This is because σ_3 of C-Q is three times greater than that of C-F as we dictated $F_cL/2 = q_cL^2/6 = M_0$. The optimal η for the voltage and the energy density were 0.5 and 0.18 respectively.

Similar to Fig. 3.5, Figs. 3.6 (e) and (f) show the normalized electrical outputs when film and substrate are flipped. The σ_3 contribution will again counteract the σ_1 contribution but the effect of σ_3 is much less significant than the C-Q case. The optimal η for the voltage

and the energy density are 0.46 and 0.18, respectively, which are the same as the PB-M case.

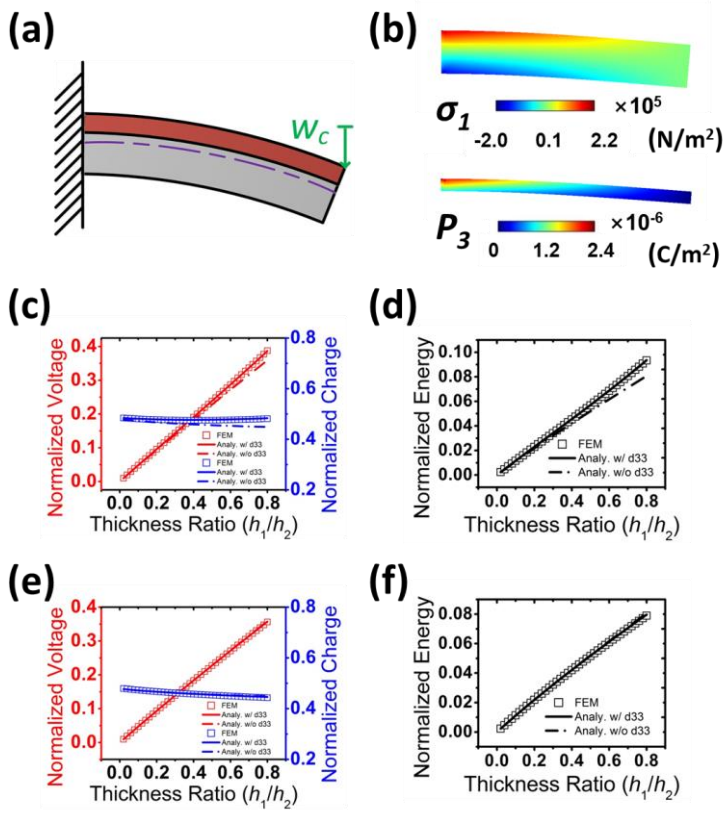

Figure 3.7. (a) A schematic for the cantilever unimorph subjected to end displacement (C-W case). (b) FEM results of σ_1 and P_3 when w_c = 53.3 nm. (c, d) The analytical and FEM results of normalized voltage, charge density, and energy density as functions of the thickness ratio. Dash-dot curves do not account for d_{33} effects whereas solid curves do. (e, f) The analytical and FEM results of normalized voltage, charge density, and energy density as functions of the thickness ratio when the piezo-layer and substrate positions are flipped. Dash-dot curves do not account for d_{33} effects whereas solid curves do.

Figure 3.7 offers the FEM and analytical results for the C-W unimorph as depicted in Fig. 3.7 (a). Plugging the cantilever load-displacement relation: $F = 3\bar{Y}_2 I w_c/(2L^3)$ into Eq. (3.23), the moment in the cantilever can be expressed as

$$M(x) = \frac{3\bar{Y}_2 I w_c}{2L^3}(L - x). \tag{3.30}$$

Now we can apply Eq. (3.30) to calculate the charge density and the voltage outputs just induced by σ_1 as

$$\rho_{C-W} = d_{31}\bar{Y}_1\kappa_1 h_2\left(1 + \frac{\eta}{2} - \Delta\eta\right) \tag{3.31}$$

and

$$V_{C-W} = \frac{d_{31}\bar{Y}_1\kappa_1 h_2^{\,2}}{\varepsilon_p'}\left[\eta\left(1 + \frac{\eta}{2} - \Delta\eta\right)\right], \tag{3.32}$$

respectively. Similar to the C-F case, the modified charge density and voltage of C-W condition with the d_{33} effect included are given by

$$\rho'_{C-W} = d_{31}\bar{Y}_1\kappa_1 h_2\left[\left(1 + \frac{\eta}{2} - \Delta\eta\right) - \frac{d_{33}}{d_{31}}\left(\frac{h_2}{L}\right)^2\left(\frac{12\bar{I} - \eta^2(3 + 2\eta - 3\Delta\eta)}{6\Sigma}\right)\right] \tag{3.33}$$

and

$$V'_{C-W} = \frac{d_{31}\bar{Y}_1\kappa_1 h_2^{\,2}}{\varepsilon_p'}\left\{\eta\left[\left(1 + \frac{\eta}{2} - \Delta\eta\right) - \frac{d_{33}}{d_{31}}\left(\frac{h_2}{L}\right)^2\left(\frac{12\bar{I} - \eta^2(3 + 2\eta - 3\Delta\eta)}{6\Sigma}\right)\right]\right\}, \tag{3.34}$$

respectively.

Figure 3.7 (b) shows the FEM result of σ_1 and P_3 under the C-W condition when the piezo-layer is 10 μm thick, the unimorph is 200 μm long, and w_c = 53.3 nm such that the average curvature, $\kappa_1 = 3w_c/2L^2$, is the same as the $\kappa_0 = 2\ m^{-1}$ used for the PB-κ case.

The normalized voltage, charge and energy density of the piezo-layer-on-substrate case are plotted in Figs. 3.7 (c) and (d) and that of the substrate-on-piezo-layer case are offered in Figs. 3.7 (e) and (f). Although the d_{33} effect is included as solid curves in both cases, the σ_3 contribution is small within the current range of h_1/h_2 and the results are very similar to the PB-κ results. But when h_1/h_2 gets very large (e.g. larger than 4), the voltage and energy density curves in Figs. 3.7 (e) and (f) will become non-monotonic.

It is interesting to notice that the C-F results (Fig. 3.6) are very similar to the PB-M results (Fig. 3.2) and the C-W results (Fig. 3.7) are very similar to the PB-κ results (Fig. 3.3), we can conclude that the pure bending condition and cantilever subjected to end load condition are almost equivalent except that the d_{33} effect in cantilever unimorphs has to be accounted for when h_2/L is large.

3.3.4 Simply Supported Bending

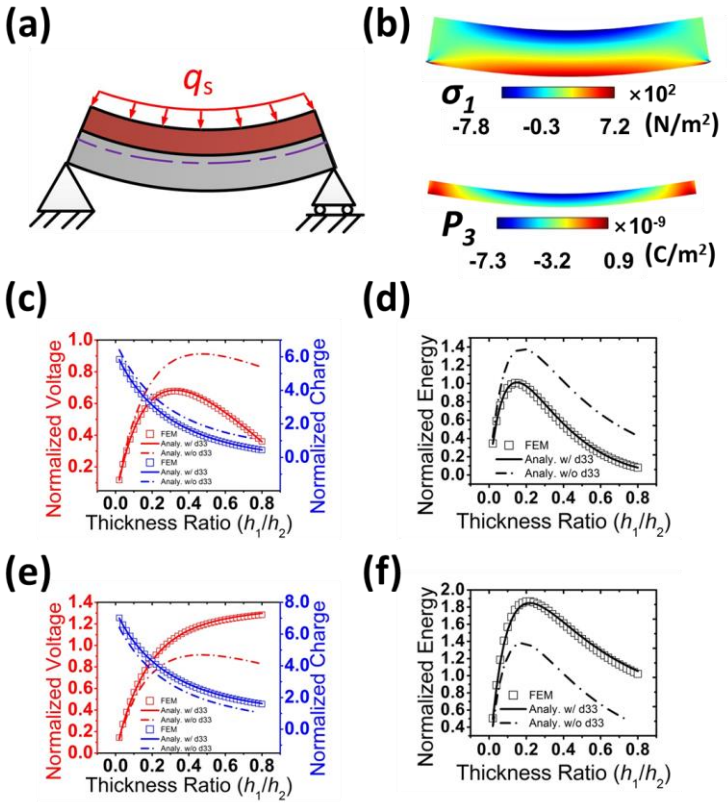

Figure 3.8. (a) A schematic for the simply supported unimorph subjected to uniformly distributed load (SS-Q case). (b) FEM results of σ_1 and P_3 when q_s = 30 N/m. (c, d) The analytical and FEM results of normalized voltage, charge density, and energy density as functions of the thickness ratio. Dash-dot curves do not account for d_{33} effects whereas solid curves do. (e, f) The analytical and FEM results of normalized voltage, charge density, and energy density as functions of the thickness ratio when the piezo-layer and substrate positions are flipped. Dash-dot curves do not account for d_{33} effects whereas solid curves do.

Simple support is another popular boundary condition for beams. When subjected to uniformly distributed load q_s as illustrated in Fig. 3.8 (a), the moment function can be written as

$$M(x) = \frac{q_s x}{2}(L - x). \tag{3.35}$$

Hence the charge density and the voltage output induced by σ_1 are obtained using Eqs. (3.7) and (3.35) as

$$\rho_{SS-Q} = \frac{d_{31} q_s L^2}{12 h_2^{\,2}} \left[\frac{\Sigma}{\bar{I}} \left(1 + \frac{\eta}{2} - \Delta\eta \right) \right] \tag{3.36}$$

and

$$V_{SS-Q} = \frac{d_{31} q_s L^2}{12 \varepsilon_p' h_2} \left[\frac{\Sigma\eta}{\bar{I}} \left(1 + \frac{\eta}{2} - \Delta\eta \right) \right], \tag{3.37}$$

respectively. Comparing Eqs. (3.36) and (3.37) with Eqs. (3.17) and (3.18), SS-Q is equivalent to C-Q if $q_s = q_c/2$. Therefore, similar to the C-Q case, SS-Q should also account for the effect of σ_3 as calculated in Fig. 3.4 (c) and the modified charge density and voltage become

$$\rho'_{SS-Q} = \frac{d_{31} q_c L^2}{12 h_2^{\,2}} \left\{ \frac{\Sigma}{\bar{I}} \left[\left(1 + \frac{\eta}{2} - \Delta\eta \right) + \frac{d_{33}}{d_{31}} \left(\frac{h_2}{L} \right)^2 \left(\frac{12\bar{I}}{\Sigma} \right) \right] \right\} \tag{3.38}$$

and

$$V'_{SS-Q} = \frac{d_{31} q_c L^2}{12 \varepsilon_p' h_2} \left\{ \frac{\Sigma \eta}{\bar{I}} \left[\left(1 + \frac{\eta}{2} - \Delta \eta \right) + \frac{d_{33}}{d_{31}} \left(\frac{h_2}{L} \right)^2 \left(\frac{12 \bar{I}}{\Sigma} \right) \right] \right\}. \qquad (3.39)$$

In Eqs. (3.38) and (3.39), the d_{33} term always vanishes as h_2/L decreases, which is similar to the C-Q case. However, unlike the C-Q case, the d_{33} term minifies both charge density and voltage output since σ_1 in the piezo-layer is negative in the SS-Q case. This effect is clearly observable in Figs. 3.8 (c) and (d), where the solid curves that account for the d_{33} effects are much lower than the dash-dot curves and demonstrate much better agreement with the FEM results. In this case, the optimal η for the voltage and the energy outputs are 0.32 and 0.14, respectively.

Similar to the C-Q case that the d_{33} effect presents in this boundary/loading condition, we also provide the solutions when the piezo-layer and the substrate are flipped, as shown in Figs. 3.8 (e) and (f). Now the d_{33} effect enhances the output as expected and its contribution is as significant as the piezo-layer-on-substrate case. For the given range of h_1/h_2, the voltage curve is monotonic and hence there is no optimal η for the voltage output. If the beam length increases, there would be an optimal η which will be similar to the C-Q case. The optimal η for the energy density is 0.22.

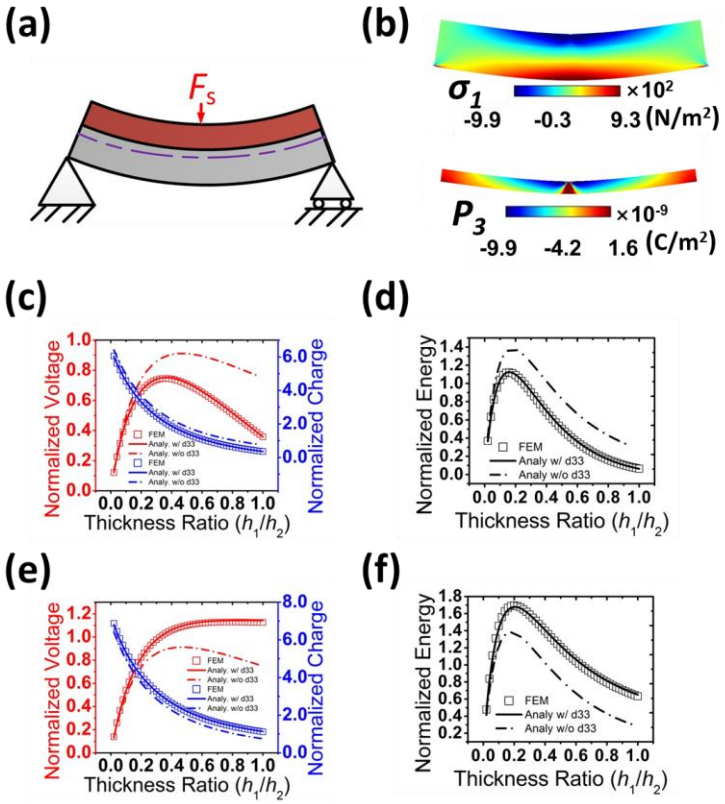

Figure 3.9. (a) A schematic for the simply supported unimorph subjected to point load (SS-F case). (b) FEM results of σ_1 and P_3 when F_s = 4 mN. (c, d) The analytical and FEM results of normalized voltage, charge density, and energy density as functions of the thickness ratio. Dash-dot curves do not account for d_{33} effects whereas solid curves do. (e, f) The analytical and FEM results of normalized voltage, charge density, and energy density as functions of the thickness ratio when the piezo-layer and substrate positions are flipped. Dash-dot curves do not account for d_{33} effects whereas solid curves do.

Figure 3.9 shows the results for the SS-F case. As the point load F_s is applied at the middle of the beam, the analytical expression of the moment is given by

$$M(x)=\begin{cases}\dfrac{F_s x}{2} & for\ \ 0\le x\le \dfrac{L}{2}\\ \dfrac{F_s(L-x)}{2} & for\ \ \dfrac{L}{2}\le x\le L\end{cases}. \tag{3.40}$$

The charge density and voltage outputs just induced by σ_1 are

$$\rho_{SS-F}=\frac{d_{31}F_sL}{8h_2^{\,2}}\left[\frac{\Sigma}{\bar{I}}\left(1+\frac{\eta}{2}-\Delta\eta\right)\right] \tag{3.41}$$

and

$$V_{SS-F}=\frac{d_{31}F_sL}{8\varepsilon_p{}'h_2}\left[\frac{\Sigma\eta}{\bar{I}}\left(1+\frac{\eta}{2}-\Delta\eta\right)\right]. \tag{3.42}$$

The effective moment term in the SS-F case is $F_sL/8$ while that of the C-F case is $F_cL/2$. If the effective moments are required to be equal, then $F_s = 4F_c$. Figure 3.9 (b) shows the FEM results of σ_1 and P_3, when the piezo-layer is 10 μm thick and $F_s = 4F_c$, where F_c is the end point load applied in the C-F case. The magnitude of σ_1 is similar to that in the C-F case, except the sign is opposite. To account for the effect of σ_3 as illustrated in Fig. 3.4 (d), we need to modify Eqs. (3.41) and (3.42) to be

$$\rho'_{SS-F}=\frac{d_{31}q_cL^2}{8h_2^{\,2}}\left\{\frac{\Sigma}{\bar{I}}\left[\left(1+\frac{\eta}{2}-\Delta\eta\right)+\frac{d_{33}}{d_{31}}\left(\frac{h_2}{L}\right)^2\left(\frac{8\bar{I}}{\Sigma}\right)\right]\right\} \tag{3.43}$$

and

$$V'_{SS-F} = \frac{d_{31} q_c L^2}{8\varepsilon_p' h_2} \left\{ \frac{\Sigma\eta}{\bar{I}} \left[\left(1 + \frac{\eta}{2} - \Delta\eta \right) + \frac{d_{33}}{d_{31}} \left(\frac{h_2}{L} \right)^2 \left(\frac{8\bar{I}}{\Sigma} \right) \right] \right\}. \tag{3.44}$$

In Eqs. (3.43) and (3.44), the d_{33} term always vanishes as h_2/L decreases, which is similar to the SS-Q case. However, the polarization density induced by σ_3 in SS-F case is less than that of SS-Q. To achieve the same effective moment, we need $q_s = 3F_s/(2L)$, which means SS-Q case has 1.5 times larger effective σ_3 than SS-F case. The same conclusion can also be made by comparing the coefficient of the d_{33} term between Eqs. (3.38) and (3.43): 12 in SS-Q case vs. 8 in SS-F case. Therefore, the electrical output variation caused by the d_{33} effect in SS-Q is greater than that in SS-F, which can be observed from the comparison between Fig. 3.8 (c) and Fig. 3.9 (c). The optimal η for maximum voltage and the energy density outputs are 0.36 and 0.16, respectively in Figs. 3.9 (c) and (d). When piezo layer and substrate are flipped, Figs. 3.9 (e) and (f) suggest the optimal η are 0.84 for maximum voltage output and 0.2 for maximum energy density output, respectively.

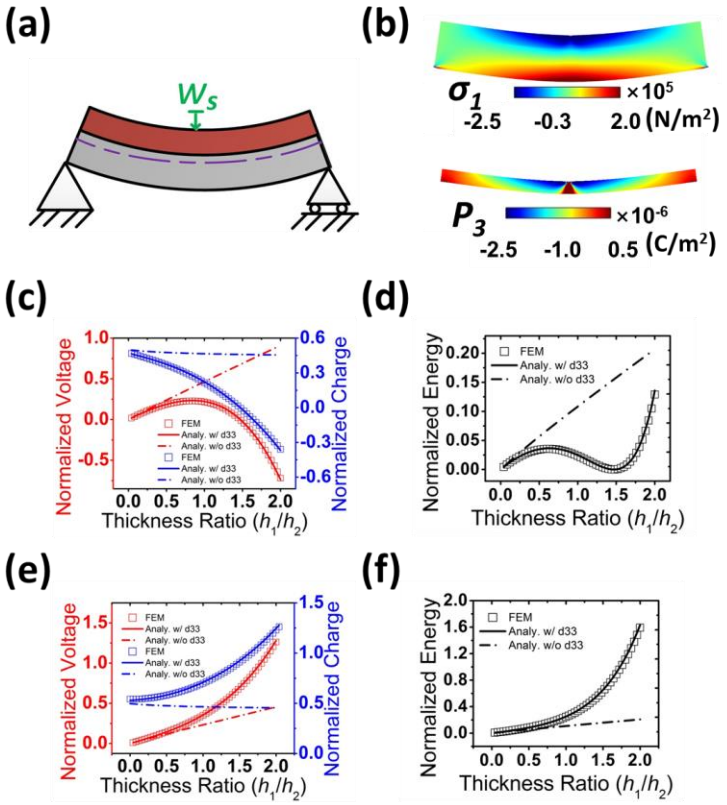

Figure 3.10. (a) A schematic for the simply supported unimorph subjected to central displacement (SS-W case). (b) FEM results of σ_1 and P_3 when w_s = 13.3 nm. (c, d) The analytical and FEM results of normalized voltage, charge density, and energy density as functions of the thickness ratio. Dash-dot curves do not account for d_{33} effects whereas solid curves do. (e, f) The analytical and FEM results of normalized voltage, charge density, and energy density as functions of the thickness ratio when the piezo-layer and substrate positions are flipped. Dash-dot curves do not account for d_{33} effects whereas solid curves do.

Figure 3.10 (a) illustrates the SS-W condition where a simply supported unimorph is subjected to a fixed center displacement, w_s. The load-displacement relation of a simply supported beam subjected to center load or displacement is $F = 48\bar{Y}_2 I w_s / L^3$, therefore the moment function of the SS-W case can be obtained by substituting this new F in Eq. (3.40):

$$M(x) = \begin{cases} \dfrac{24\bar{Y}_2 I w_s}{L^3} x & for \;\; 0 \le x \le \dfrac{L}{2} \\ \dfrac{24\bar{Y}_2 I w_s}{L^3}(L - x) & for \;\; \dfrac{L}{2} \le x \le L \end{cases}. \tag{3.45}$$

As in the SS-F case, the analytical solutions for the charge density and the voltage output for the SS-W case without considering the d_{33} effect are

$$\rho_{SS-W} = d_{31}\bar{Y}_1 \kappa_2 h_2 \left(1 + \frac{\eta}{2} - \Delta\eta\right) \tag{3.46}$$

and

$$V_{SS-W} = \frac{d_{31}\bar{Y}_1 \kappa_2 h_2^{\,2}}{\varepsilon_p{}'} \left[\eta\left(1 + \frac{\eta}{2} - \Delta\eta\right)\right], \tag{3.47}$$

respectively. When the d_{33} effect is considered as in the SS-F case, Eqs. (3.46) and (3.47) have to be modified to

$$\rho'_{SS-W} = d_{31}\bar{Y}_1 \kappa_2 h_2 \left[\left(1 + \frac{\eta}{2} - \Delta\eta\right) + \frac{d_{33}}{d_{31}}\left(\frac{h_2}{L}\right)^2 \left(\frac{8\bar{I}}{\Sigma}\right)\right] \tag{3.48}$$

and

$$V'_{SS-W} = \frac{d_{31}\bar{Y}_1\kappa_2 h_2^{\,2}}{\varepsilon_p'}\left\{\eta\left[\left(1+\frac{\eta}{2}-\Delta\eta\right)+\frac{d_{33}}{d_{31}}\left(\frac{h_2}{L}\right)^2\left(\frac{8\bar{I}}{\Sigma}\right)\right]\right\}, \tag{3.49}$$

respectively. Figure 3.10 (b) shows the FEM results of σ_1 and P_3 distribution under the SS-W condition when w_s = 13.3 nm, which is chosen to ensure that the average curvature $\kappa_2 = 6w_s/L^2$ is the same as the κ_0 = 2 m^{-1} used for the PB-κ case. Without considering the d_{33} effect, the normalized electrical outputs are plotted as dash-dot curves in Figs. 3.10 (c) and (d), which are similar to the solid curves in the PB-κ cases but very different from the FEM results. When the d_{33} effect is considered, the solid curves find much better agreement with the FEM outputs. When piezo-layer is on top of the substrate, the d_{33} effect minifies the outputs as d_{33} is negative. Consequently, the optimal η for maximum voltage output is 0.84 and 0.62 for maximum energy density. Since both voltage and charge density drop below 0 as η increases, we extend the range of η to 2 and find that as η increases, the energy density drops to a minimum after reaching a maximum, and then takes off again. This behavior is distinctly different from PB-κ case where voltage, charge density, and energy density are always monotonically increasing with η. Still, as L increases, the d_{33} effect will diminish according to Eqs. (3.48) and (3.49).

Because there is the d_{33} effect in the SS-W case, swapping piezo-layer and substrate would yield different outputs, as shown in Figs. 3.10 (e) and (f). All three outputs are monotonic in this case because the σ_1 and σ_3 contributions have the same sign. The d_{33} effect is clearly visible in this case, but now enhances the outputs.

3.3.5 Effects of Y_1/Y_2 and h_2/L

Throughout previous sections, the elastic mismatch, $\Sigma = \overline{Y_1}/\overline{Y_2}$, has been fixed to be 1.148 for unimorphs composed of PVDF-TrFE bonded to Kapton. Here we would like to investigate the effects of Σ. As Wang et al. [96] described, the optimal thickness ratio η of unimorph cantilevers also varies with Σ.

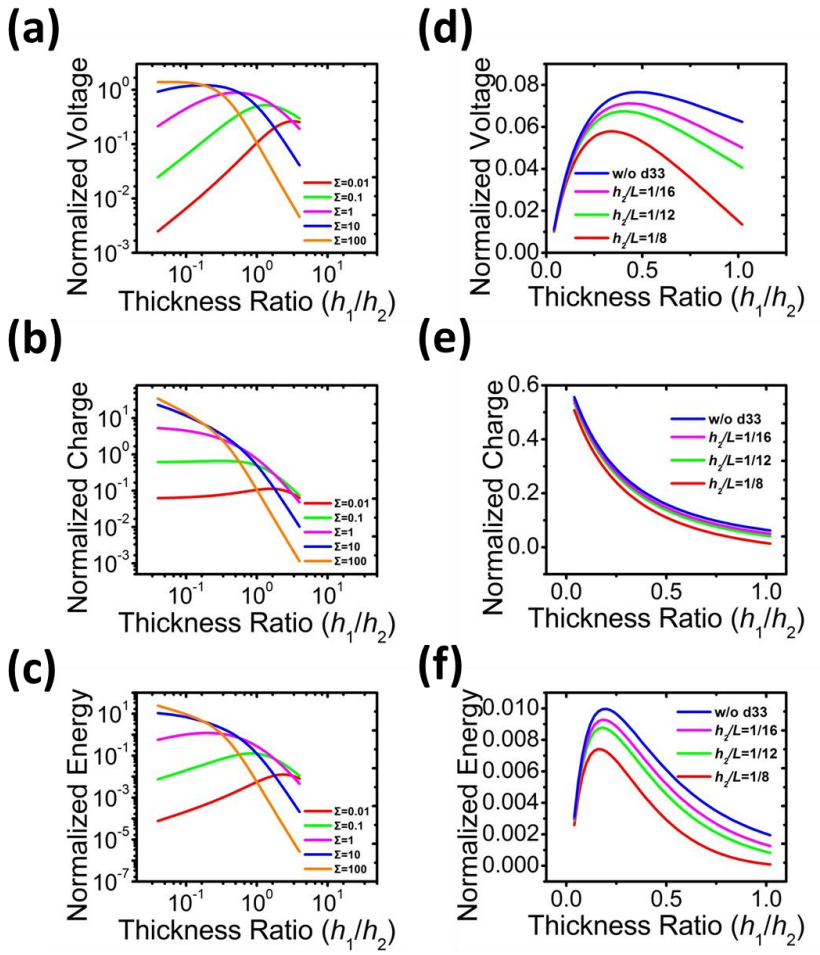

Figure 3.11. (a, b, c) The effects of stiffness ratio on the normalized voltage, charge density, and energy density under the PB-M condition. (d, e, f) The effects of substrate thickness-to-length ratio on the normalized voltage, charge density, and energy density under the SS-Q condition.

Figure 3.11 plots the normalized voltage, charge density, and energy density as functions of η in log-log scale under various Σ for the PB-M condition in which case d_{33}

plays no role. As can be seen in Figs. 3.11 (a) (plotted from Eq. (3.11)), (b) (plotted from Eq. (9)) and (c) (plotted from Eq. (3.12)), the optimal η shifts to the left as Σ increases in all electrical output cases and are in general different for different outputs. When η is small (i.e. $\eta << 1$), the larger Σ always yields the higher output but when η is large, larger outputs are achieved for smaller Σ.

The effect of h_2/L is also investigated because it is a component that always appears in the d_{33} term. When $h_2/L << 1$, the d_{33} effect is negligible but when h_2/L is finite, the d_{33} effect sometimes can become obvious or even overwhelms σ_1 contribution. Figure 3.11 (d), (e), and (f) plot normalized voltage, charge density, and energy density as functions of η under various h_2/L for the SS-Q condition. For voltage and energy density, the optimal η shifts slightly to the right as h_2/L decreases and stabilizes when h_2/L drops below 1/20, which is consistent with the observation in [112]. Similar plots can be constructed for other boundary/loading conditions which have to account for the d_{33} effect.

3.3.6 Unimorph Actuators

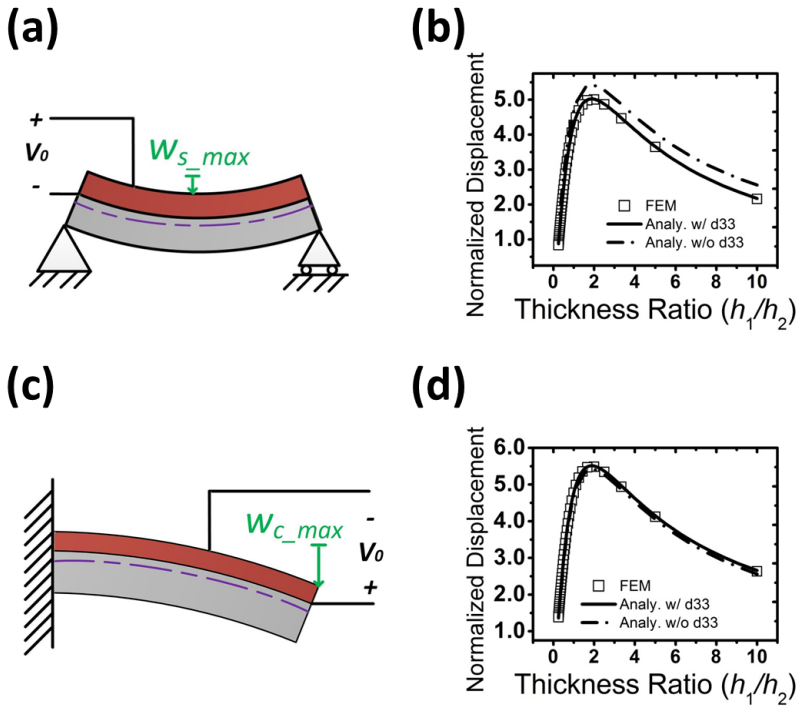

Figure 3.12. (a) A schematic of a simply supported unimorph actuator subjected to constant electric potential (SS-V case). (b) The analytical and FEM results of normalized maximum displacement of the unimorph as a function of the thickness ratio. Dash-dot curves do not account for d_{33} effects whereas solid curves do. (c) A schematic of a cantilever unimorph actuator subjected to constant electric potential (C-V case). (d) The analytical and FEM results of normalized maximum displacement of the unimorph as a function of the thickness ratio. Dash-dot curves do not account for d_{33} effects whereas solid curves do.

Thickness ratio variation also affects the displacement of a unimorph subjected to applied electric field [113] as shown in Fig. 3.12. By applying the electric field $E = V_0/h_1$ across the thickness direction of the piezoelectric layer, a uniform longitudinal strain is induced in the piezoelectric layer. Consequently, the magnitude of the longitudinal stress within the piezoelectric layer is $\sigma_1 = d_{31}\bar{Y}_1 V_0/h_1$, while the stress at the substrate layer remains zero. Therefore, the resultant moment of the unimorph can be written as

$$M_E = \int_{h_2}^{h_1+h_2} d_{31}\bar{Y}_1 V_0 \cdot (\frac{z}{h_1} - \Delta)\, dz\,, \tag{3.50}$$

which is calculated to be

$$M_E = d_{31}\bar{Y}_1 V_0 h_2 \left[\left(1 + \frac{\eta}{2} - \Delta\eta\right)\right]. \tag{3.51}$$

Hence, the maximum displacement of the simply supported unimorph subjected to constant voltage (SS-V) as shown in Fig. 3.12 (a) is

$$w_{s\_\max} = \frac{d_{31}V_0 L^2}{8h_2^{\,2}} \left\{ \frac{\Sigma}{\bar{I}} \left[\left(1 + \frac{\eta}{2} - \Delta\eta\right) + \frac{d_{33}}{d_{31}} \left(\frac{h_2}{L}\right)^2 \left(\frac{8\bar{I}}{\Sigma}\right) \right] \right\}. \tag{3.52}$$

The second term in Eq. (52) accounts for the thickness direction deformation from σ_3 induced by the constant electric potential.

Figure 3.12 (b) plots the normalized maximum actuation displacement obtained from FEM and Eq. (3.52) with respect to the thickness ratio when Σ is fixed to be 1.148. The d_{33} effect slightly diminishes the displacement. The optimal thickness ratio for

maximum displacement is 1.89. Similarly, the maximum displacement of the cantilever unimorph subjected to constant electric potential (C-V) as shown in Fig. 3.12 (c) is

$$w_{c\_max} = \frac{d_{31} V_0 L^2}{2 h_2^{\,2}} \left\{ \frac{\Sigma}{\bar{I}} \left[\left(1 + \frac{\eta}{2} - \Delta\eta \right) - \frac{d_{33}}{d_{31}} \left(\frac{h_2}{L} \right)^2 \left(\frac{2\bar{I}}{\Sigma} \right) \right] \right\}. \tag{3.53}$$

Figure 3.12 (d) plots the normalized maximum displacement with respect to the thickness ratio. The optimal thickness ratio of the maximum displacement of the C-V is 1.89, which is the same as the SS-V case. The σ_3 effect is also considered in this case and it enlarges the displacement but is less significant compared to the SS-V case. Due to symmetry, the actuation of unimorphs under pure bending is identical to the C-V case.

It is worth mentioning that the moment induced by the applied electric potential does not equal to any moment induced by the mechanical loadings since the stress distributions are very different. Therefore, the generation mode and actuation mode of the same unimorph are not reciprocal to each other.

3.4 SUMMARY

We investigate the electromechanical behaviors of flexible unimorph power generators and actuators. Analytical and numerical models are built to unveil the effects of piezo-layer-to-substrate thickness ratio and piezoelectric material constants on energy conversion under eight different boundary/loading conditions. Our theory reveals that when the unimorph is subjected to displacement-controlled loading conditions, the charge,

voltage, and energy outputs are monotonic functions of the thickness ratio whereas when the unimorph is subjected to load-controlled conditions, optimal thickness ratios for maximum voltage and energy outputs exist. Our linear piezoelectric theory has been fully validated by FEM. We have also found that except pure bending conditions, all cantilever and simply supported unimorphs should care about the d_{33} (i.e. σ_3) contribution when the unimorph length is not much larger than the thickness. A simplified average stress model is proven effective in accounting for the d_{33} effect. d_{33} effect may also change the outputs of displacement-controlled problems from monotonic to non-monotonic. The effects of elastic mismatch and thickness-to-length ratio have been discussed and analytical solutions for unimorph based actuators are also offered. This work provides a comprehensive and accurate solution for the design and optimization of unimorph based power generators and actuators.

Chapter 4: A Stretchable PVDF Vibration Sensor for Seismocardiogram (SCG) Monitoring[1]

Seismocardiography (SCG) is a measure of chest vibration associated with heartbeats, which can be recorded on the surface of the human chest. While ultrathin and stretchable electronic tattoos (e-tattoos) have been widely reported for continuous electrocardiogram (ECG) sensing, wearable SCG sensors are still based on either off-the-shelf rigid accelerometers or stiff piezoelectric membranes. I created an ultra-thin and stretchable SCG sensor based on 28-μm-thick PVDF patterned into filamentary serpentine network. The trade-off between the stretchability/compliance and sensitivity of the piezoelectric serpentines was studied through both experimental and computational means. Motion artifact cancellation was realized by subtracting inhomogeneous SCG waveforms from twin sensors.

---

[1] T. Ha, J. Tran, S. Liu, H. Jang, R. Mithbander, Y. Qiu, J. Duong, P. Wang, A. Tandon, J. Sirohi, N. Lu*. "A stretchable piezoelectric E-tattoo for synchronous and beat-to-beat mechano-acoustic-cardiovascular monitoring", to be submitted. Author contributions: T. Ha conducted the device design, fabrication, testing, experiment, and signal processing. J. Tran performed the 3D DIC experiment. S. Liu led the FEM analysis with Y. Qiu's assistance. H. Jang, R. Mithbander, Y.Qiu, J. Duong helped the human subject experiment. N. Lu, P. Wang, A. Tandon, and J. Sirohi supervised and coordinated the project. T. Ha and N. Lu wrote the paper.

4.1 INTRODUCTION

Cardiovascular diseases (CVD) are the leading cause of death in the United States and cost the nation hundreds of billions of dollars each year [114]. Wearable devices are being developed to perform continuous cardiovascular monitoring for outpatients [115-117]. Among all cardiovascular signals, the best known is electrocardiogram (ECG), which indicates the electrical activity of the heart. To track ECG continuously, wearable devices such as Holter monitors have been developed [118]. While ECG reflects myocardial conduction, myocardial contraction is characterized by mechano-acoustic signals [119]. These mechano-acoustic signals provide important insights into cardiovascular health that complements those inferred from ECG. Typical mechano-acoustic signals of the heart include phonocardiogram (PCG, sounds made by the heart) [120], seismocardiogram (SCG, local vibrations of the chest wall as a result of heartbeat) [121], and ballistocardiogram (BCG, whole body movement arising from the sudden ejection of blood into the vasculature) [121]. All three mechano-acoustic signals originate from mechanical activities of the heart but are measured differently. PCG is measured by stethoscopes. SCG can be recorded by wearing a digital accelerometer on the chest [122, 123]. BCG should be measured by a swing bed or a force sensor placed on a weighing scale [121].

Compared to stretchable ECG electrodes, not much progress has been made in the development of stretchable SCG sensors. SCG can be obtained by mounting commercial accelerometers on the human chest [121]. However, the thickness and rigidity of conventional accelerometers make them uncomfortable to wear and susceptible to inertial

motion of the chest [122]. Physical strapping or taping is also required to reduce the acoustic mismatch caused by the air gap between the rigid accelerometer and the skin [122]. To overcome this issue, Liu et al. proposed a soft and stretchable accelerometer using serpentine electrodes and elastomeric encapsulation instead of rigid PCB [122]. Nevertheless, the device thickness of 2 mm is still obstructive, and the polysilicon-based sensor requires rigid package.

Another device that can detect SCG is a piezoelectric transducer, which employs piezoelectric materials to convert mechanical vibrations to electrical pulses [124]. Self-powered sensing is an important advantage of a piezoelectric transducer since it may not require any external power for sensing. In fact, a blanket electromechanical film (EMFi, EMFIT Ltd, Finland) has been taped on the chest for SCG measurement [125]. Yet the in-plane elastic stiffness of EMFi is 0.5-1 GPa [126], which is orders of magnitude higher than that of human skin (130 kPa – 20 MPa [127]). Although stretchable electromechanical devices based on patterned inorganic piezoelectric materials such as lead zirconate titanate (PZT) or zinc oxide (ZnO) have been reported [37, 38, 52, 53], they are intrinsically brittle materials and expensive to manufacture. Polyvinylidene fluoride (PVDF) is a commercially available piezoelectric polymer that is mechanically robust and biocompatible, but is intrinsically stiff (Young's modulus = 3.6 GPa) compared with human skin [56, 57]. Stretchable electromechanical sensors or energy harvesters made out of patterned PVDF are emerging in recent years. For example, line-type micro-patterned PVDF membrane [39], ribbon-like PVDF embedded in Ecoflex [58], and PVDF islands

interconnected by serpentine metal wires [59] have shown stretchability around 30%, but their thinness and softness have not been explicitly addressed. Electrospun PVDF fibers have been employed for wearable sensors and energy harvesters, but so far electrodes could only be placed at the ends of the fiber bundles instead of along each fiber in most cases [60-62].

The work reported here proposes to pattern commercially available metalized PVDF sheets into a filamentary serpentine (FS) shape to make wearable mechano-acoustic sensors, with special emphasis on their thickness, softness, and stretchability. Our previous studies revealed that orders of magnitude reduction in stiffness can be achieved when stiff films are patterned into serpentine ribbons [87, 128]. We have also developed a cost-effective cut-and-paste method to shape metal-on-polymer sheets [46] as well as 2D materials [129]. The created stretchable PVDF vibration sensor with Tegaderm matrix has the stretchability of more than 110 % with the sensitivity of 0.4 mV per micro-strain.

4.2 METHOD

4.2.1 Fabrication of Filamentary Serpentine (FS) Polyvinylidene Fluoride (PVDF) Vibration Sensor

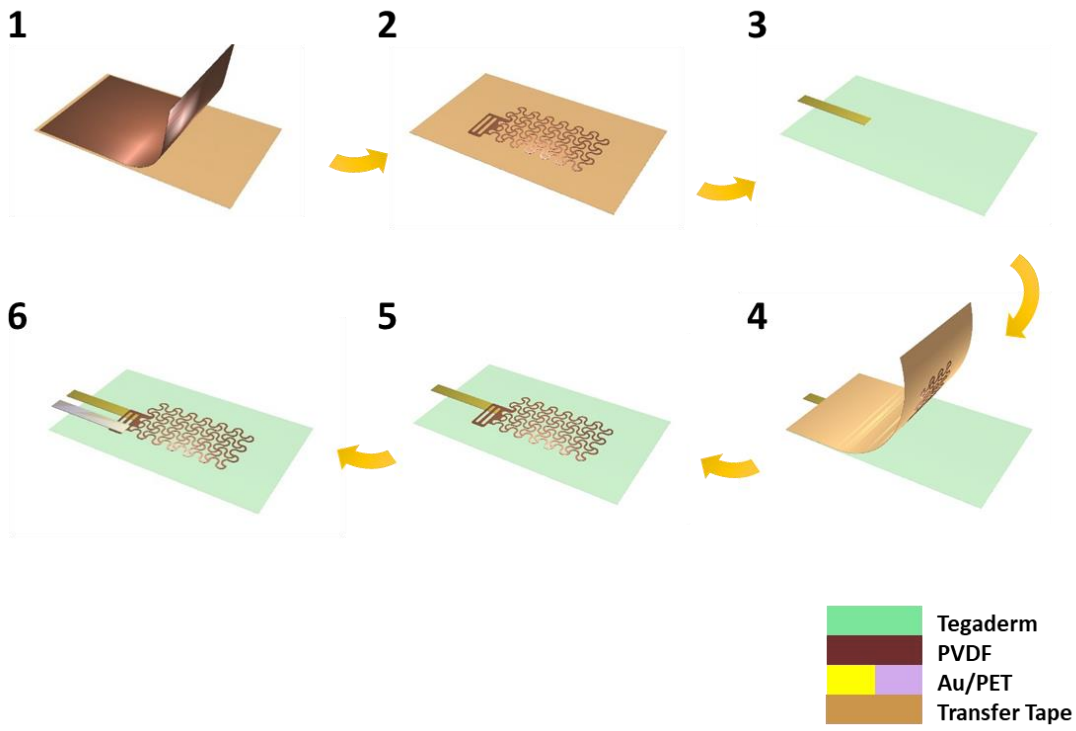

Figure 4.1. Schematics of the cut-and-paste fabrication process of the FS PVDF vibration sensor.

The whole manufacturing process described in Fig. 4.1 is called “cut-and-paste” method, which is chemical- and mask/stencil-free and can be completed within 20 minutes [46]. The fabrication procedure includes four major steps: (i) placing a bare film on a

weakly adhesive transfer tape; (ii) cutting the film by a mechanical cutter plotter; (iii) removing extraneous parts; (iv) transferring remaining parts to a target substrate. An electroded 28.4 μm PVDF film (piezo film sheets, TE connectivity) was attached to a 100-μm-thick weakly adhesive transfer tape (TransferRite Ultra 582U, American Biltrite Inc.) backed by a supporting film (350 GSM, Inkpress Media) (Step 1). Within several minutes, the PVDF film was carved by a mechanical cutter plotter (Cameo, Silhouette) with designed patterns. For optimal cutting quality, the blade setting in software (Silhouette Studio) was established with 5 in blade exposure, 1 in cutting speed, and 3 in depth. Due to the weak adhesion of the transfer tape, extraneous parts of the PVDF film can be easily peeled off by a pair of tweezers after the cutting (Step 2). Then, the pattern remained on the transfer tape is transferrable to the target substrate (Tegaderm tape, 3M^{TM}), due to the huge difference between the adhesive forces of the transfer tape (2.2 N/25 mm, peel adhesion @ 90º) and the Tegaderm tape (35.6 N/60 mm) (Step 3). Before/after the FS PVDF was transferred, a pair of Au/PET connector of 25.4 mm ×3.81 mm backed by a self-adhesive laminating sheet (Avery) were attached to the Tegaderm to extend the top and bottom electrode of the FS PVDF for the connection with a flat flexible connector (FFC, Clincher Flex Connectors, Amphenol FCI) (Step 4). Lastly, a 2nd Tegaderm layer was applied to encapsulate just the FS PVDF to prevent the direct contact of PVDF electrode on human skin (Step 5).

4.2.2 FEM of The Electromechanical Behaviors of FS PVDF Vibration Sensors

We used commercial finite element modeling (FEM) software ABAQUS v6.14 to simulate the output voltage, electric displacement and mechanical deformation of the FS PVDF vibration sensor under uniaxial stretching. The FEM models had the same geometries and measured electromechanical properties as described in the main texts. The FS PVDF model was sandwiched by two 47-μm thick Tegaderm layers whose width was 8 mm. We assumed perfect bonding between PVDF and Tegaderm. The Young's modulus of Tegaderm was set to be 7 MPa according to our previous measurements [46]. Poisson's ratios for PVDF and Tegaderm were 0.34 and 0.49, respectively. The electric potential of one metalized surface was set to be 0 (grounded), while that of the other metalized surface was set to be an unknown constant. In terms of the mechanical boundary conditions, one end of the FS PVDF model was clamped whereas the other end was clamped with tensile strains from 0 % to 2%. No buckling was observed within such small applied strains when Tegaderm provides the constraints to diminish the out-of-plane displacement.

The FS PVDF vibration sensors with different substrates attaching to the skin were applied to investigate the substrate effect. The displacement data at S1 and S2 acquired from the three-dimensional digital image correlation (3D DIC) method was averaged and plugged into the FS PVDF model conformed on a skin-like model. In this case, the skin-like model is assumed to be a bi-layer substrate 25-μm dermis of 20 kPa and 175-μm epidermis of 100 kPa). The device is attached on the epidermis and covered by a substrate with a specific modulus (Tegaderm = 7 MPa, polyethylene terephthalate (PET) = 3GPa).

Twelve grid points were appointed on the substrate of the FS PVDF model with a gap distance of 4.79 mm, which is equivalent to the spatial resolution of 3D DIC. The displacement data was fitted to be polynomial function and applied at the surface of the epidermis. The electrical boundary condition was the same as above.

4.3 RESULTS

4.3.1 SCG Measurement by FS PVDF Vibration Sensor, DIC method, and Accelerometer

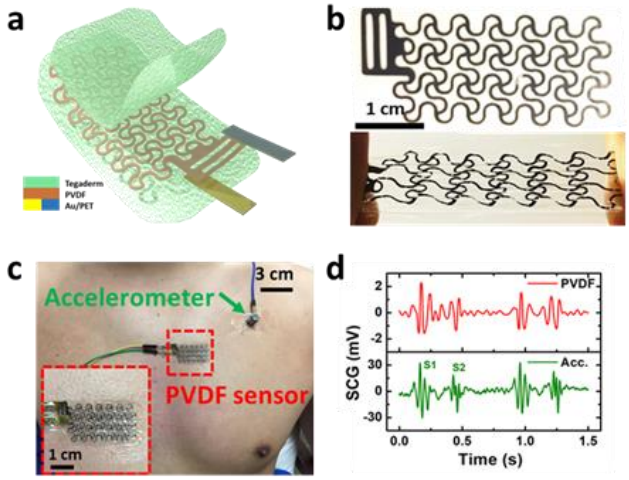

Figure 4.2. FS PVDF vibration sensor and 3D DIC method for SCG measurement. (a) A structure schematic of the FS PVDF vibration sensor. (b) photograph of freestanding/stretched FS PVDF vibration sensor. (c) A FS PVDF vibration sensor (red box, inset) and an accelerometer (green arrow) attached on the chest and (d) corresponding SCG signals measured by the FS PVDF vibration sensor and the accelerometer.

The epidermal sensor system must be sufficiently thin and stretchable to conform to the skin, while the sensitivity is comparable with conventional sensors. The design of sensors must reflect these requirements and be validated. The schematic of FS PVDF

vibration sensor is described in Fig. 4.2 (a). A 28.4-μm-thick PVDF film with 80 nm-thick Ni-Cu electrodes on the top and bottom surfaces (piezo film sheets, TE Connectivity) was trimmed in a serpentine mesh shape by a cutting machine (Cameo®, Silhouette). The size of whole sensor is 38.1 mm × 18.1 mm, and the in-plane waviness defined by width-to-radius ratio is 0.4, when the width is 0.5 mm and non-zero joint angle of 15 º. Instead of using thermal release tape as before, weakly adhesive transfer tape (TransferRite Ultra 582U, American Biltrite Inc.) was used as the temporary support to avoid the thermal deformation of PVDF. Then, the trimmed PVDF film was sandwiched by 47-μm-thick stretchable medical tapes (Tegaderm, 3M^{TM}) to avoid discharging. Figure 4.2 (b) presents a photograph of a FS PVDF vibration sensor without connectors. The tattoo is highly soft and stretchable such that it imposes negligible mechanical constraint when laminated on human skin. To validate its functionality as a SCG sensor, the FS PVDF vibration sensor was compared with an accelerometer with the sensitivity of 100 mV/g (Model 352C65, PCB Piezotronics). Both the FS PVDF vibration sensor and the accelerometer were attached on the chest (Fig. 4.2 (c)). As described in Fig. 4.2 (d), SCG signals captured by the PVDF sensor and the accelerometer have comparable waveforms and well-aligned S1 and S2 features.

4.3.2 FS PVDF Vibration Sensor Characterization

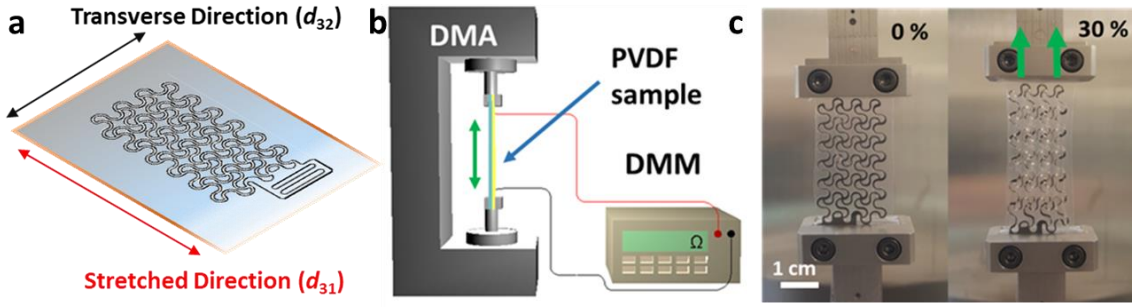

Figure 4.3. (a) The pattern of FS PVDF sensor with respect to the stretched direction and the transverse direction of PVDF sheet. (b) A schematic of a PVDF sample subjected to tensile test with in situ electrical measurements. (c) A photograph of a FS PVDF vibration sensor under the tensile test, from 0 % to 30 %.

It is necessary to remind that piezoelectric coefficient of PVDF film we used are different in terms of the stretched direction, as shown in Fig. 4.3 (a). Therefore, when the FS PVDF is patterned to have a longer shape in the stretched direction, it is more sensitive to strains in the stretched direction than the transverse direction. The parameters derived from straight PVDF ribbons in Section 2.3 are not directly applicable to properties of the FS PVDF vibration sensor, since the sensor possesses new electromechanical performances derived from its mesh-like FS shape. Although an analytical solution for characterizing serpentine ribbons based on elasticity was reported previously [130], the analytical solution is not directly applicable to the piezoelectric mesh-like FS. To examine

electromechanical properties of the FS PVDF vibration sensor, the sensor was uniaxially stretched by a RSA-G2 DMA, while the electrical resistance of electrodes on both sides was measured *in situ* using a Rigol digital multimeter (DMM), as illustrated in Fig. 4.3 (b) and (c).

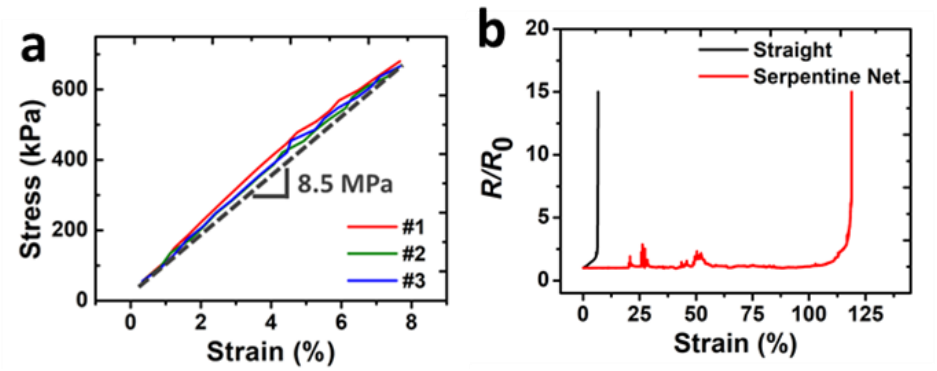

Figure 4.4. (a) A stress-strain curve of three different FS PVDF sensors. (b) The stretchability of a straight PVDF ribbon and a FS PVDF sensor.

Figure 4.4 (a) presents the strain-stress curve of the FS PVDF vibration sensor, and the effective modulus E_1 is measured to be 8.5 MPa from three different samples, of which Young's modulus is only 0.24 % of the solid PVDF film modulus. Another well-known index for estimating mechanical robustness is stretchability. Here, the stretchability of devices can be defined by the critical uniaxial tensile strain where the electrical resistance explodes [131]. Figure 4.4 (b) shows that the FS PVDF has the stretchability of 112.9 %, which is approximately 20 times higher than the straight PVDF ribbon (5.8 %). Although the stretchability of Cu-Ni is known to be less than 2.3 % [132], the FS design

allows huge stretchability. In addition, the early rupture of Cu-Ni on the straight PVDF ribbon was prevented by polymer encapsulation.

PVDF film patterned into the mesh-like FS shape has enhanced stretchability and compliance; however, the variation in geometry also affects its electromechanical performance. Therefore, we carried out electromechanical characterization of the FS PVDF to quantitatively reveal the trade-off between stretchability and sensitivity. To measure the electromechanical response of the FS PVDF, we adopted the oscillation mode of the DMA and conducted a cyclic test, while the electrical output of the FS PVDF sample was collected by DAQ. A voltage follower was connected between the PVDF sample and DAQ to amplify the current with the same voltage output. The 1 GΩ resistor was placed right before the voltage follower to remove the low frequency fluctuation.

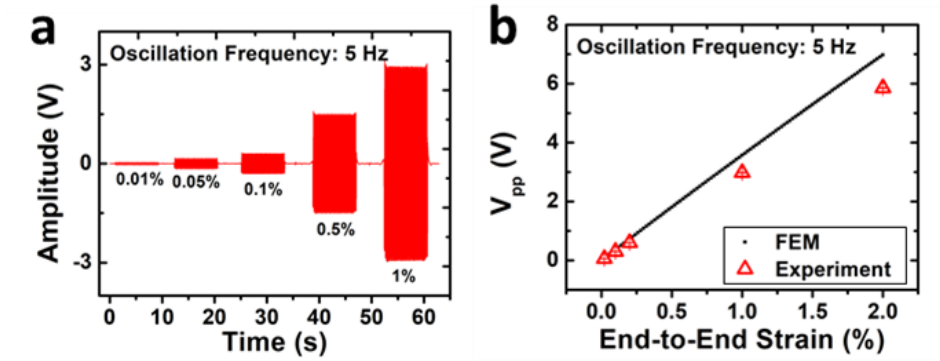

Figure 4.5. (a) Generated voltage output from the FS PVDF sensor under 5 Hz sinusoidal tensile strain with amplitude from 0.01 % to 1 %. (b) Experimental and FEM results of compensated peak-to-peak voltage output with respect to applied end-to-end strains.

Figure 4.5 (a) shows the output voltage generated from a FS PVDF when stretched by five different strain amplitudes, ranged from 0.01 % to 1%, at 5 Hz of oscillation. Output voltage was measured across the thickness direction. To fully understand the electromechanical behaviors of piezoelectric serpentine mesh, we also performed finite element modeling (FEM) using commercial FEM software ABAQUS. The model setup can be found in Materials and Methods and the input material properties were those measured by ourselves. The output voltage can be calculated based on the stress distribution through the following equation:

$$V = -\frac{h}{\varepsilon_3 A}\int_{\Omega} d_{3j}\sigma_j dS \tag{4.1}$$

where Ω represents one of the metalized surfaces, A is the total area of Ω, h is the thickness of the PVDF film, and ε_3 is the out-of-plane permittivity of the PVDF film, which was calculated to be 90.31 pF/m based on our capacitance measurement. Plotting the experimentally measured and compensated peak-to-peak output voltages (red) and those independently computed by FEM (black) in Fig. 4.5 (b), we found a good agreement between the two. The calculated mechano-electrical conversion sensitivity of the FS PVDF in the stretched direction is about 0.4 mV per micro-strain, which is only 3.6% of the solid PVDF. As a piezoelectric material, PVDF converts mechanical stress to electric displacement. Since serpentine is a well-known stress-relieving structure, the voltage output is expected to be lower than its straight counterpart. In summary, high stretchability of the serpentine PVDF mesh is achieved at the cost of electromechanical sensitivity. For

measuring SCG by a sensor attached on the chest, high compliance of the sensor is essential to reduce constraint on arbitrary skin deformation. Therefore, we adopted the FS PVDF as our SCG sensor for their softness and stretchability, which is comparable with the stratum corneum of human skin [133]. Despite such detriment in sensitivity, the FS PVDF vibration sensor can measure SCG from the chest, as confirmed in Fig. 4.2 (d).

4.3.3 Dual FS PVDF Vibration Sensor System for Motion Artifact Cancellation

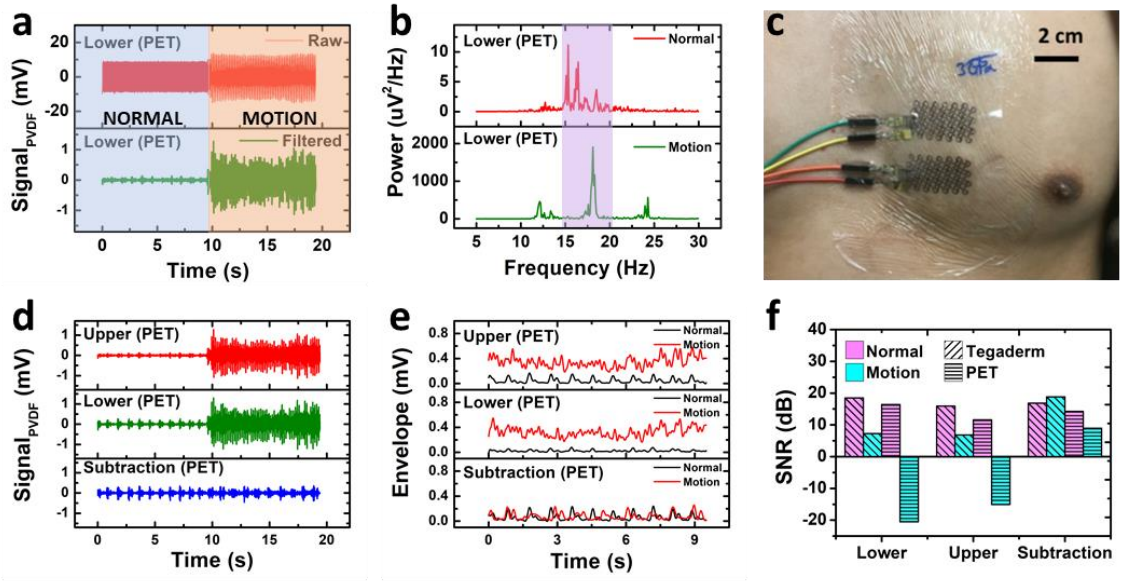

Figure 4.6. Dual-sensor based motion artifact cancellation. (a) Raw and filtered SCG signals captured by a PET-covered FS PVDF vibration sensor under normal/motion condition. (b) A periodogram of filtered SCG signals captured by the PET-covered FS PVDF vibration sensor under normal/motion condition. (c) A photograph of the dual FS PVDF sensing system (PET covered) attached on the chest of a subject. (d) Filtered SCG signals and (e) corresponding envelope signals recorded by upper and lower FS PVDF vibration sensors and their subtraction result under normal/motion condition. (f) Signal-to-noise ratio (SNR) of single/dual mode sensing system with different substrates under normal/motion condition.

Since piezoelectric materials including PVDF transduce mechanical signals to electrical signals, and vice versa, the FS PVDF vibration sensor may gauge any mechanical signals such as motion artifacts rather than SCG, despite its conformability to human skin. Generally, motion artifacts or power noises outside of the signal frequency range are removable by signal processing. The normal section in Fig. 4.6 (a) shows an example of signal processing. Eroded by the power noise, the SCG waveform is unrecognizable from the raw signal measured by the sensor with PET substrate. In this case, the SCG waveform can be extracted from the raw signal using a band pass filter with the frequency range of 12 – 40 Hz, as the filter suppresses signals outside of the frequency range, including the power noise at 60 Hz. However, the noise within the signal frequency range is almost inseparable with conventional filters. As observed in the motion section of Fig 4.6 (a), motion artifacts are not restrained although the same filter is applied. The reason can be found in the Fig. 4.6 (b) that most signal components of motion artifacts lies within the frequency range of SCG, with 200 times higher power than the power of SCG.

Different approaches have been introduced to solve the motion artifact issue through software such as smoothing [134], adaptive filtering [135], threshold algorithm [136]. Recently, Chenxi Yang suggested a hardware approach of the motion artifact cancellation using the dual-accelerometer system [137]. According to his paper, when two accelerometers are placed at different locations around the chest, SCG detected from each accelerometer has a unique waveform, while motion artifacts from two accelerometers are highly correlated. When signals from two accelerometers are subtracted, due to the

assumption above, motion artifacts will be eliminated without losing SCG features. From the previous DIC results, it is visually confirmed that SCG waveforms vary with locations on the chest. Hence, based on the assumption and our findings, two FS PVDF vibration sensors were attached on the chest surface of a subject with a centimeter distance to test the motion artifact cancellation using dual-sensor system, as shown in Fig. 4.6 (c). Then, a muscle-stimulating device (Rechargeable TENS Unit Muscle Stimulator, AUVON) attached to a leg of the subject, delivered random motion artifacts with an almost consistent amplitude to the subject for 10 seconds, followed by 10 seconds of resting time. Figure 4.6 (d) shows signals measured by two sensors and their subtraction result during the experiment within the frequency range of 12- 40 Hz. Compared to signals from each sensor, features of SCG waveforms are detectable in the subtraction result regardless of motion artifacts. Comparisons of signal envelopes between the resting state (Normal) and the leg-shaking state (Motion) in Fig 4.6 € also suggest that only the subtraction result can provide the accurate SCG peak detection during the leg-shaking state. In Fig. 4.6 (f), the performance of the single sensor and the dual sensor system is quantitively evaluated by signal-to-noise ratio (SNR). Here, the signal power of Normal state S_n is the power within 12-40 Hz of the Normal state, which is equivalent to the signal power of Motion state S_m, as both states were recorded from a single experiment ($S = S_n = S_m$). Then, the noise power N_i and the SNR value of each case were calculated as follows:

$$\begin{cases} N_{\mathrm{i}} = P_{\mathrm{i}} - S \\ SNR_{\mathrm{i}}\,(\mathrm{dB}) = 10\log_{10}\left(\dfrac{S}{N_{\mathrm{i}}}\right) \end{cases} \quad \mathrm{i} = \mathrm{n}, \mathrm{m} \tag{4.2}$$

where P_{i} is the total power. Similar to previous results, a vast improvement of SNR was achieved by the dual sensor system compared with the single sensor system, exceptionally with motion artifacts.

According to our findings, the sensor with the stiff substrate tend to experience more motion artifacts than the sensor with the soft substrate. As can be seen in Fig. 4.6 (f), with a similar power level of motion artifacts, SCG is undetectable for the single sensor with PET case (negative SNR), whereas the single sensor with Tegaderm has a lower SNR than the Normal state but positive. This implies that the stiffness of the vibration sensor only affects to the sensitivity in SCG, not to the sensitivity in motion artifacts, which may arise from the difference in deformation mode between SCG and motion artifacts. To sum up, the dual sensor system can exclude motion artifacts within the target frequency range; therefore, using the dual sensor system with soft substrates may contribute to realizing robust, ambulatory SCG monitoring.

4.4 SUMMARY

PVDF sheets were mechanically patterned into FS mesh for enhanced stretchability and compliance. FS PVDF vibration sensors are able to measure high quality SCG just like a commercial rigid accelerometer, despite a trade-off between the stretchability and the

sensitivity. We also proved that motion artifacts within the signal frequency range are removable by virtue of the inhomogeneity of SCG waveforms from dual sensors at different locations.

Chapter 5: Three-Dimensional Digital Image Correlation (3D DIC) for Full-Field Seismocardiogram (SCG) and Characterization of Skin-Mounted PVDF Sensors[1]

Full-field analysis of the chest motion is required to investigate the chest deformation originated from SCG and to best locate the SCG sensors. Three-dimensional digital image correlation (3D DIC) method was used to explore the motion of the human chest derived from respiration vs. the cardiac movement. The effect of skin-sensor elastic mismatch on measured SCG quality was also studied via 3D DIC. It was found that stiff substrate diminishes the sensitivity of filamentary serpentine PVDF network.

[1] T. Ha, J. Tran, S. Liu, H. Jang, R. Mithbander, Y. Qiu, J. Duong, P. Wang, A. Tandon, J. Sirohi, N. Lu*. "A stretchable piezoelectric E-tattoo for synchronous and beat-to-beat mechano-acoustic-cardiovascular monitoring", to be submitted. Author contributions: T. Ha conducted the device design, fabrication, testing, experiment, and signal processing. J. Tran performed the 3D DIC experiment. S. Liu led the FEM analysis with Y. Qiu's assistance. H. Jang, R. Mithbander, Y.Qiu, J. Duong helped the human subject experiment. N. Lu, P. Wang, A. Tandon, and J. Sirohi supervised and coordinated the project. T. Ha and N. Lu wrote the paper.

5.1 INTRODUCTION

The location dependency of SCG is renowned and reported in several studies, yet it has not been thoughtfully investigated. Most researchers place an accelerometer on the sternum [138], while some reports suggest that left mid-sternal region of the chest could provide much stronger signal [139, 140]. Distinctive SCG waveforms were detected in four different cardiac valve auscultation sites, according to Wen-Yen Lin et al. [141]. Although SCG monitoring using multiple sensors are also proposed [142, 143], a spatial resolution from a sensor array is not sufficient to illustrate high quality mapping, and the installation of a sensor array is arduous. Herein, 3D DIC method, which is a non-contact, simple, and full-field surface deformation measurement method, was applied to acquire the morphology of SCG on the chest and to investigate the best location for SCG sensors. Furthermore, three-dimensional (3D) deformation with a superior spatial and temporal resolution is attainable with a high-speed stereo camera system. Although this method has been frequently used to investigate mechanical properties of biological tissues [144-146] and skin deformation of human body [147-150], using 3D DIC method for the SCG measurement is the first time.

5.2 METHOD

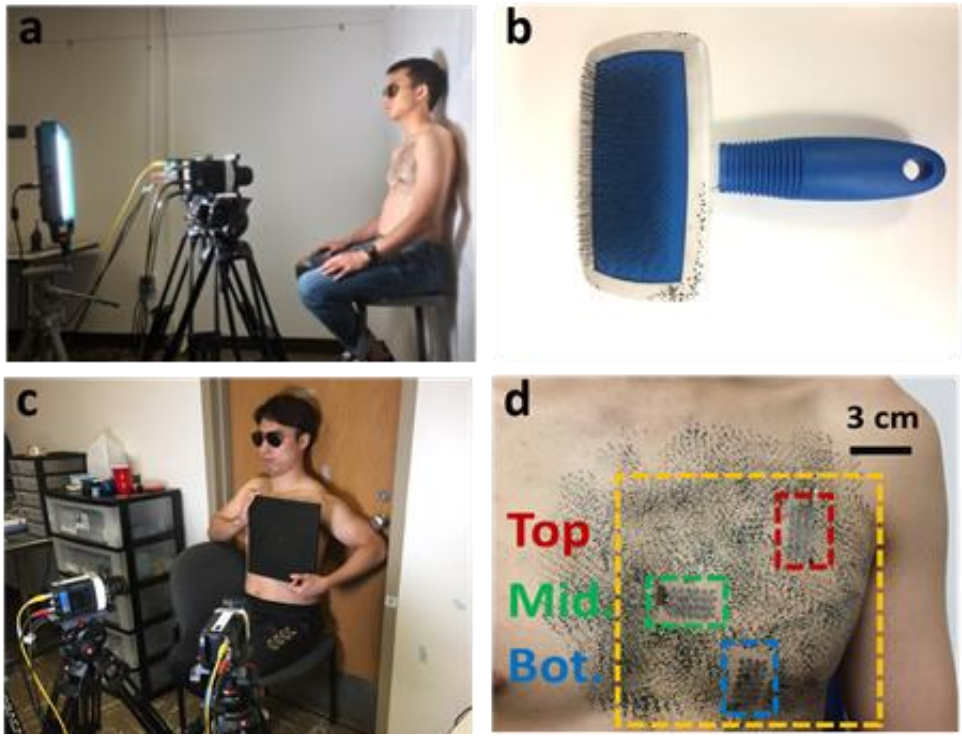

Figure 5.1. (a) A photograph of the 3D DIC method experiment configuration for recording SCG. (b) A photograph of a pet brush for scattering pattern. (c) A photograph of a subject holding a calibration plate for 3D DIC method. d) A photograph of the chest surface of a subject painted with the pattern of random dots. Each FS PVDF vibration sensor is attached on different locations: Top, Mid, and Bot.

After the installation of 3D DIC system, a subject was properly located within the sight of high-speed cameras (Phantom Miro 310, AMETEK), and the cameras were

adjusted to capture the chest surface of the subject (Fig. 5.1 (a)). The distance between the subject and the cameras was approximately 55 cm, and the angle between the cameras was 30 º. To improve the accuracy of the measurement, a random black-dot pattern was painted on the chest surface by a metal pet brush (Fig. 5.1 (b)). The subject wore sunglasses to avoid any ocular damage from the LED panel light, which increases the contrast of the target surface and thus improves the quality of the DIC measurement. Before recording images, the spatial configuration was calibrated using a two-level calibration plate (Fig. 5.1 (c)). Then, the image of the chest surface was captured for 16 seconds at 500 Hz frame rate. Figure 5.1 (d) shows the chest surface with the pattern of random dots, while the yellow box indicates the region of interest captured by the high-speed cameras. Three FS PVDF vibration sensors were attached to validate the location dependency of the SCG amplitude and the correlation of SCG signals measured by the sensors and the 3D DIC method. When FS PVDF vibration sensors are placed on the chest surface, we adjusted its strain sensing orientation based on the postulation that the chest surface deforms equibiaxially. The captured images were processed by software (StrainMaster, LaVision) to calculate 3D displacement and in-plane strain of the chest surface. The displacement vector and the in-plane strain value were mapped into a 2D array of coordinate points within the area of 200 mm × 180 mm, whereas the distance between each coordinate point was 4.79 mm.

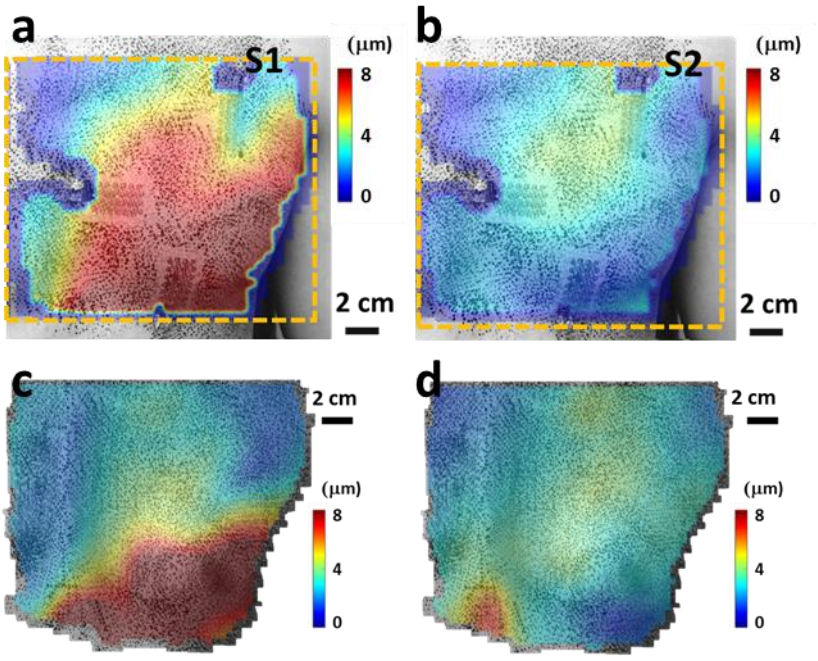

Figure 5.2. The out-of-plane displacement map averaged in peak times, particularly at (a) S1 and (b) S2. (c, d) The out-of-plane displacement map averaged in peak times at S1 and S2 from the other subject.

Based on the coordinate points, the average out-of-plane displacement maps at peak timings of S1 and S2 are illustrated in Fig. 5.2 (a) and (b). Although each subject had slightly different distinct locations for S1 and S2 (Fig. 5.2 (c) and (d)), S1 is strong around the left corner of the chest, while S2 is strong at the upper-middle of the chest. This outcome may be originated from the difference in closing timing of cardiac valves, as S1 and S2 are related to mitral valve closure (MC) and aortic valve closure (AC), respectively

[151, 152]. A corresponding full-field 3D morphology of a single SCG period is described in Fig. 5.3.

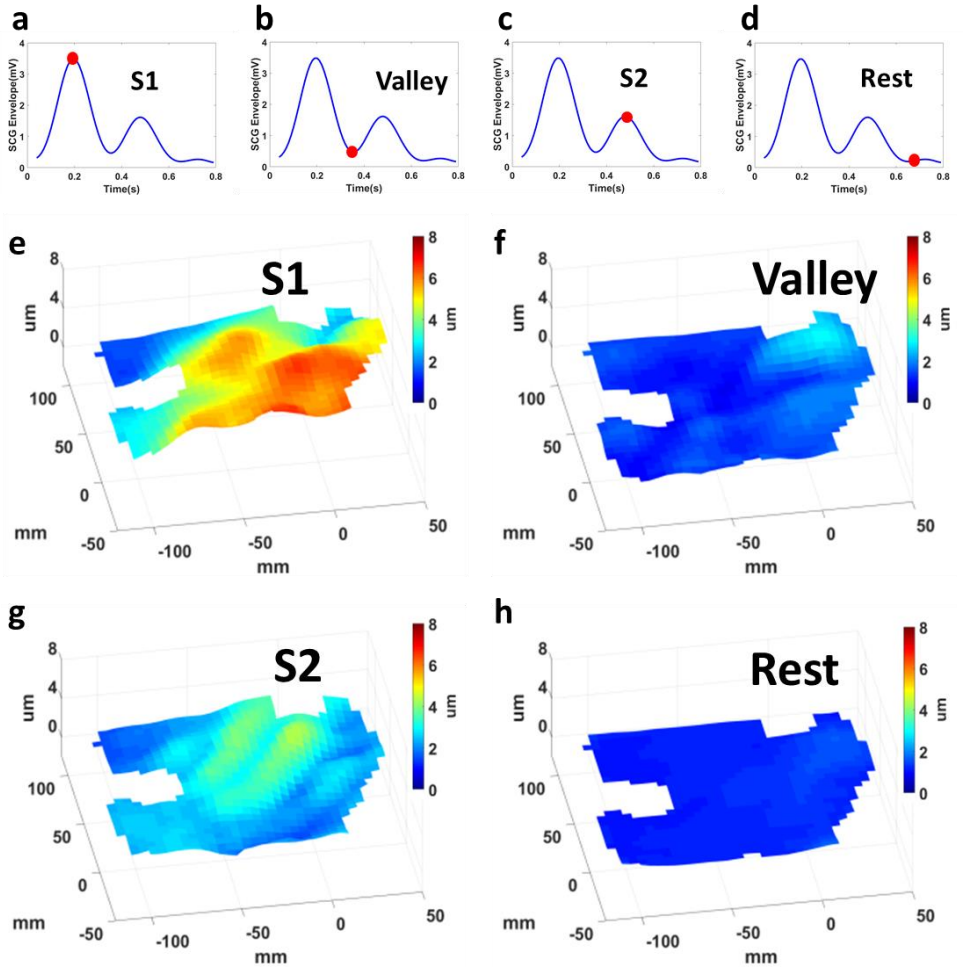

Figure 5.3. (a-d) A periodic cycle of SCG (S1-Valley-S2-Rest) and (e-h) corresponding full-field 3D map.

5.3 RESULTS

5.3.1 SCG Measurement by 3D DIC Method and FS PVDF

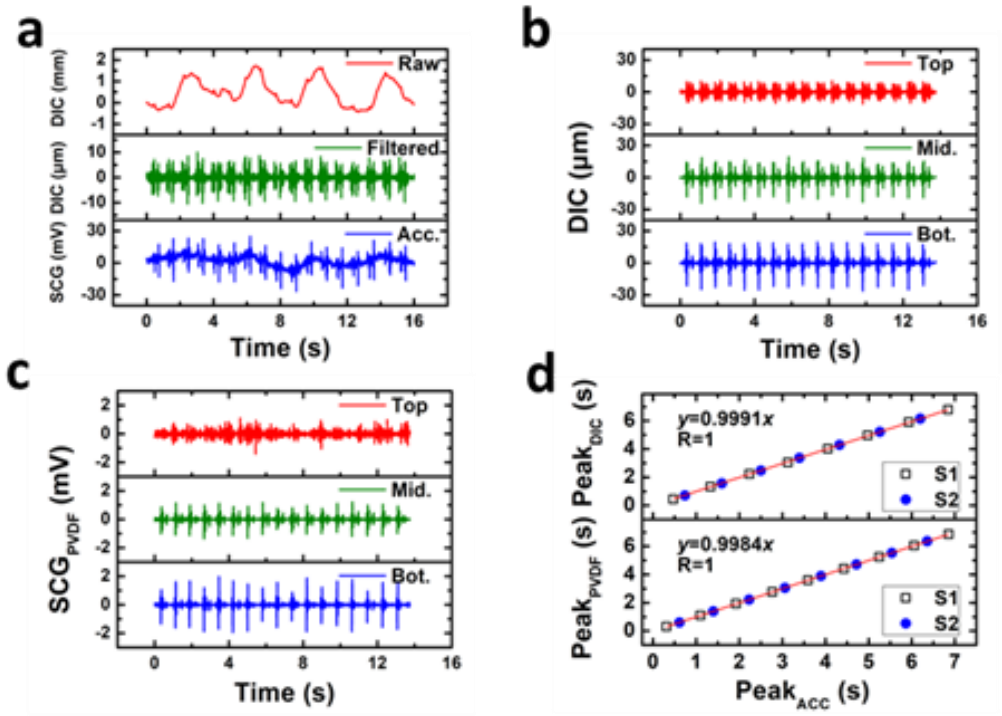

Figure 5.4. (a) Measured signals by 3D DIC method (Raw, Filtered) and the accelerometer (Acc.) from the chest. (b, c) SCG signals at three different locations (Top, Mid, and Bot) captured by (b) 3D DIC method and (c) FS PVDF vibration sensors. (d) The correlation of SCG peak times (S1 and S2) measured by the 3D DIC method, PVDF sensor, and the accelerometer.

The first row of Fig. 5.4 (a) shows the raw out-of-plane displacement at an arbitrary coordinate near the upper right chest captured by 3D DIC method. Here, the displacement signal with roughly 2 mm amplitude includes normal breathing and heartbeat movements of the chest. To extract SCG signal from the raw out-of-plane displacement, the 4^{th} order Butterworth filter with 12 – 40 Hz bandwidth was applied. Compared to SCG measured by an accelerometer (Model 352C65, PCB Piezotronics), the filtered displacement signal measured by 3D DIC method shows almost identical tendency, especially for S1 and S2 peaks, as described in the second and third row of Fig. 5.4 (a). Again, 3D DIC method could distinguish SCG although it was in few micrometers scale.

The SCG measurement comparison between the FS PVDF vibration sensor and DIC method is shown in Fig. 5.4 (b) and (c). The out-of-plane displacement at three different chest locations is described in Fig. 5.4 (b). As can be seen, S1 and S2 features were clearly visible, and few micrometers of displacement were detectable at each point. Out of SCG signals from three locations, the bottom SCG signal has the strongest S1, followed by the middle SCG signal. However, S2 was stronger at the top and the middle than the bottom. The signals measured by sensors placed at the same locations exhibit a similar trend, according to Fig. 5.4 (c). In this respect, the middle location is the best location for the sensor as both S1 and S2 are distinctively measurable.

The first row of Fig. 5.4 (d) shows the correlation between the SCG peaks captured by a conventional accelerometer and the SCG peaks captured by the 3D DIC method. A perfect correlation was observed between the out-of-plane displacement measured by the 3D DIC

method and SCG measured by an accelerometer. Accordingly, 3D DIC method is comparable with the accelerometer in terms of detecting S1 and S2 features of SCG. Likewise, SCG peak times (S1 and S2) captured by the FS PVDF sensor and the accelerometer were almost identical. As such, the FS PVDF vibration sensor is able to detect important SCG features as reliably as the DIC method or the commercial accelerometer with the perfect conformability on the skin.

5.3.2 Substrate Effect on FS PVDF Sensor

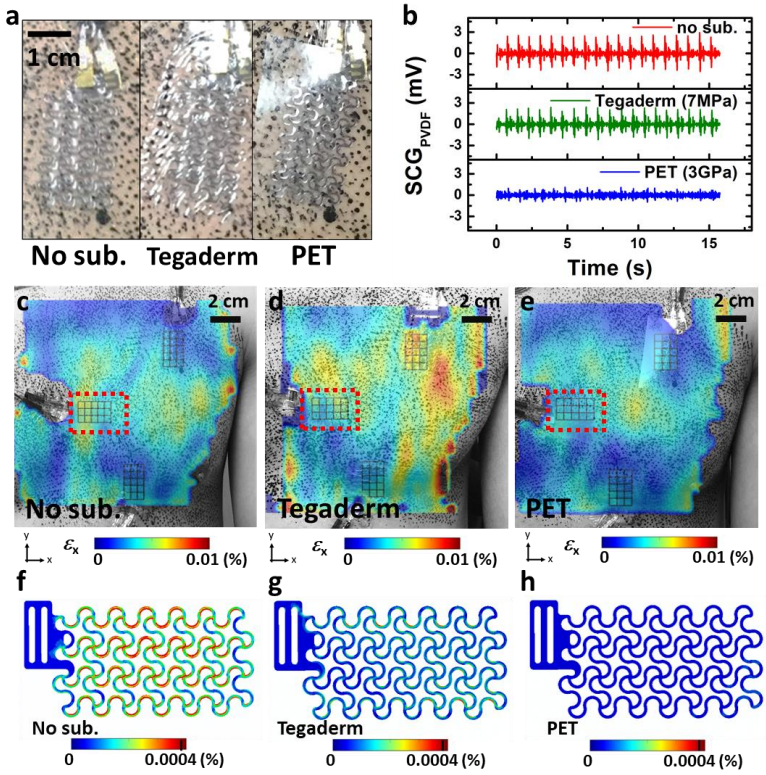

Figure 5.5. The substrate effect on the FS PVDF sensor. (a) Photograph of FS PVDF sensors covered by no substrate, 47 μm-thick Tegaderm, and 50 μm-thick PET. (b) SCG signals recorded by FS PVDF sensors with three different types of substrates at the middle location. The full-field, x-direction strain maps of (c) no substrate case, (d) Tegaderm case, and (e) PET case, derived from the average of chest deformation at S1 peaks. FEM results of x-directional strains on the FS PVDF sensors with (f) no substrate, (g) Tegaderm substrate, and (h) PET substrate.

A skin-conformal sensor with a stiff substrate may not only constrain human skin, but also lower the sensitivity of the sensor. To investigate the effect of the substrate stiffness to the sensitivity of the FS PVDF vibration sensor, 3D DIC system was used for visualizing in-plane strains when sensors with different substrates were attached on the chest. Figure 5.5 (a) shows three types of sensors attached on the chest with different conditions of substrates; no substrate, 47 μm-thick Tegaderm, and 50 μm-thick PET. A thin layer (~ 1 μm) of rosin-based adhesive (De-Hesive Sparay, Cramer) was applied to the insulation and adhesion between the sensor and the skin surface. For each trial of measuring in-plane strains with 3D DIC method, three vibration sensors with the same type of substrate were attached to specific locations (Top, Middle, and Bottom). For 16 seconds at 500Hz, in-plane strains of the chest surface were obtained by DIC while SCGs at different locations were measured *in situ* by the FS PVDF vibration sensors. Figure 5.5 (b) depicts the SCG signal captured by sensors with three different types of substrates at the middle location. Among three types of sensors, the sensor without a substrate exhibited the strongest SCG signal, followed by the sensor with Tegaderm substrate. This indicates that the stiffer the substrate is, the less sensitivity the FS PVDF vibration sensor has. This is because strains generated on the chest surface unlikely to be transferred to the sensor when the sensor is significantly stiffer than human skin [153, 154]. We also observed that the substrate stiffness was mostly irrelevant to the out-of-plane deformation.

The skin constraint effect by substrates is also confirmed by the strain map derived from 3D DIC. Fig. 5.5 (c), (d), and (e) shows the x-direction strains derived from the

average of chest surface deformation at S1 peaks. Note that the sensor has the stronger sensitivity in longer direction due to the anisotropy of the purchased PVDF film; therefore, x-direction strain map is correlated with the sensor output. Compared to the strain map for the sensors with no substrate, contour changes of strains are observed around sensors in the strain map for the sensors with substrates, which indicates that the sensor with a substrate stiffer than human tissue constrains the skin deformation.

The correlation between the sensitivity of sensors and the skin deformation constraint by stiff substrates is further supported by FEM analysis. For each substrate case, the displacement of the middle sensor area, measured by DIC system, was averaged in time, particularly peak timings of S1 and S2. The averaged displacement was then entered into a FEM model of the FS PVDF vibration sensor. Strains of sensors with different substrates are described in Fig. 5.5 (f), (g), and (h), which accounts for the sensor with soft or no substrate is more stretchable than the sensor with stiff substrates. It is worth mentioning that in-plane is much larger than out-of-plane strain in the case of the chest deformation. Based on the strain FEM result, estimated voltage outputs of the sensor with no substrate, Tegaderm, and PET were 2.74 mV, 2.20 mV, and 0.86 mV, respectively, which are similar to the experimental result shown in Fig. 5.5 (b). The similarity of electrical outputs from the FEM and the experiment proves the validity of the electrical output from the sensor and provides the estimated range of the chest surface strain by SCG, which is few micro strain. In conclusion, the substrate for the FS PVDF vibration sensor should be as soft as possible so that the sensor does not constrain the skin deformation

without losing its strain sensitivity. The FS PVDF vibration sensor with no substrate performs the best; yet, it may not be the best option considering the difficulty in installation, stability, etc.

5.4 SUMMARY

Using the DIC method, the chest surface deformation during a cycle of SCG was analyzed and described in full-field displacement and strain map. Based on the displacement mapping on the chest at S1 and S2 peaks, the left side of the sternum is considered to be an optimal SCG sensing spot. The study on the substrate stiffness of the sensor reveals that a low elastic mismatch between human skin and a sensor enhances the sensing performance

Chapter 6: Stretchable E-tattoo for Synchronous Electro- & Mechano-Acoustic Cardiovascular Monitoring

This chapter introduces an electro- and mechano-acoustic cardiovascular (EMAC) sensing tattoo with a dimension of 63.5 mm × 38.1 mm × 0.122 mm, a total mass of 150 mg, an effective modulus of 8.5 MPa, and a stretchability of 100%. Synchronous ECG and SCG measurements can be performed through customized data acquisition (DAQ) circuits and denoising schemes. Strong negative correlations were found between RAC intervals (a.k.a. systolic time intervals) and systolic/diastolic blood pressures. Thus, the EMAC sensing tattoo has a potential for non-invasive and continuous estimation of blood pressure.

---

[1] T. Ha, J. Tran, S. Liu, H. Jang, R. Mithbander, Y. Qiu, J. Duong, P. Wang, A. Tandon, J. Sirohi, N. Lu*. "A stretchable piezoelectric E-tattoo for synchronous and beat-to-beat mechano-acoustic-cardiovascular monitoring", to be submitted. Author contributions: T. Ha conducted the device design, fabrication, testing, experiment, and signal processing. J. Tran performed the 3D DIC experiment. S. Liu led the FEM analysis with Y. Qiu's assistance. H. Jang, R. Mithbander, Y.Qiu, J. Duong helped the human subject experiment. N. Lu, P. Wang, A. Tandon, and J. Sirohi supervised and coordinated the project. T. Ha and N. Lu wrote the paper.

6.1 INTRODUCTION

Unlike the well-known correlation between the pulse transit time (PTT) and blood pressure (BP) [155-158], only few papers mentioned the correlation between the duration of systole and BP [125, 159-163]. Tang and co-authors have noticed strong negative correlation between systolic blood pressure (SBP) and systole through measurements on six subjects using a conventional ECG sensor and a microphone for PCG. Their explanation was that exercise elevated the heart rate and cardiac muscle contractility in the first phase, which would result in shorter valve closure time intervals [162]. In the following work, he conducted animal experiment to investigate the correlation between the systole (RAC) and the blood pressure of the left ventricle (LVBP) [163]. The variation of blood pressure ranged from 90 mmHg to 282mmHg changed by different dose of epinephrine was measured by an invasive catheter inserted into the left ventricle. The result indicates that RAC and SBP possess significant correlation and the correlation is applicable to accurate, continuous, and non-invasive SBP estimation. In addition, strong correlations between the individual BP and the duration of systole in 16 subjects were found using a custom stethoscope for both ECG and PCG, according to Zhang's paper[161]. They attributed the correlation to the change in peripheral resistance, heart rate, and contractility of the heart [161]. Nevertheless, neither of the mechano-acoustic sensors were wearable nor stretchable.

To utilize RAC-SBP correlation with epidermal electronics technology, an integrated stretchable E-tattoo for synchronous electro- and mechano-acoustic

cardiovascular (EMAC) sensing is presented. It consists of a pair of stretchable ECG electrodes made of Au NMs with a shape of FS and the FS PVDF sensor for SCG. The integrated E-tattoo does not contain any rigid components, has a dimension of 63.5 mm × 38.1 mm × 0.122 mm, a total mass of 150 mg, an effective modulus of 8.5 MPa, and a stretchability of 100 %, which constitutes the thinnest and lightest EMAC sensing platform ever reported. It can be applied conformably and unobstructively on the human chest without acoustic impedance mismatch with the skin. High fidelity ECG and SCG can be simultaneously measured. The following describes the key features of this stretchable EMAC sensing tattoo and its capability of synchronous and beat-to-beat ECG and SCG measurements as well as BP estimation.

6.2 METHOD

6.2.1 Fabrication and Design of EMAC Sensing E-Tattoo

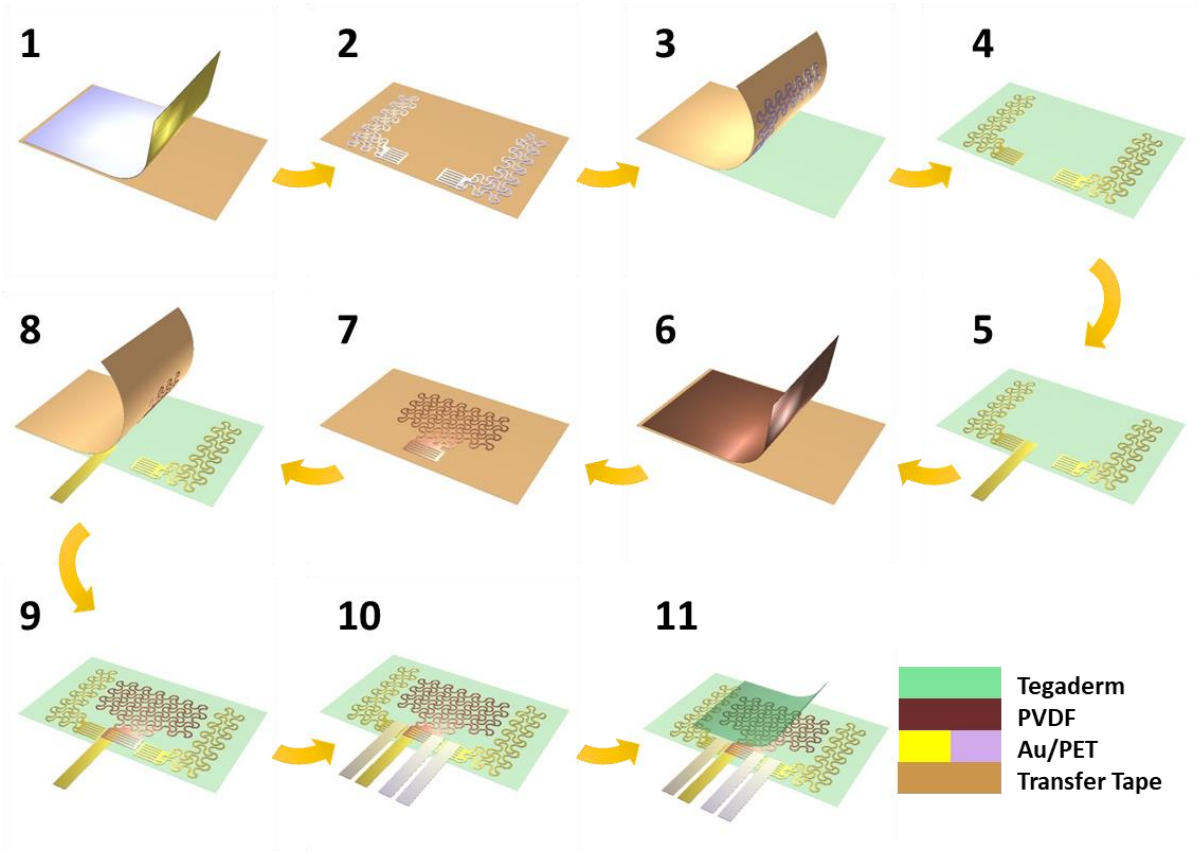

Figure 6.1. The fabrication process of the EMAC sensing tattoo.

The incorporation of ECG sensors and the FS PVDF vibration sensor grants us to create an integrated stretchable E-tattoo that is capable of EMAC sensing when attached on the human chest. With equivalent serpentine geometry of the FS PVDF vibration sensor,

Au/ PET (Rotex Tech.) were used as ECG sensors, which are 3 cm apart for high fidelity ECG measurement. A detailed manufacturing process is described in Fig. 6.1. A 76.2 mm × 50.8 mm large 100-nm-Au-on-12.5-μm-PET bilayer (Rotex Tech.) was cut-and-pasted on the Tegaderm tape (Step 1-4). Then, an Au/PET connector was placed to the Tegaderm with Au facing up (Step 5) for the bottom electrode extension of the to-be-pasted FS PVDF. In the same manner above, a FS PVDF was patterned from an electroded PVDF film (Step 6-7). After the FS PVDF sensor was transferred (Step 8-9), three more Au/PET connecters were added such that the two ECG electrodes and the top electrode of PVDF can be connected to the FFC (Step 10). Finally, the FS PVDF was encapsulated by a 2nd Tegaderm layer (Step 11). Dimensions of the final EMAC tattoo were 63.5 mm × 38.1 mm × 0.122 mm.

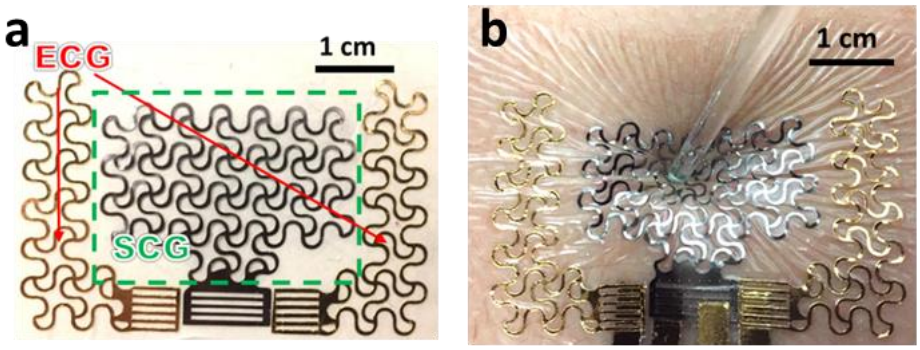

Figure 6.2. (a) A photograph of EMAC tattoo without connectors. (b) Tattoo-like behavior on human skin.

A picture of a prototype EMAC sensing tattoo is presented in Fig. 6.2 (a). The stretchability of EMAC, limited by the FS Au/PET, is about 100 % (Figure S10, Supplementary Information), while the effective modulus is 8.5 MPa, similar to the FS PVDF vibration sensor. When laminating it on human skin, it imposes negligible mechanical constraint on arbitrary skin deformation as illustrated in Fig. 6.2 (b). Even after severe skin deformation, the device remains fully conformed to the skin without delamination, slippage or mechanical failure, which ensures high fidelity sensing.

6.2.2 Data Acquisition and Signal Processing

Our experimental measurements involve the synchronous measurements of ECG and SCG by the EMAC sensing tattoo, an independent measurement of SCG by a commercial accelerometer (ADXL335, Analog Devices), and an independent continuous BP estimation by SOMNOtouch™ NIBP. The SOMNO estimates beat-to-beat BP through the PTT method, which requires three gel electrodes on the chest for one channel ECG and one rigid PPG sensor clipped on the index finger. Before each use, the SOMNO was calibrated using a sphygmomanometer (EW3153 Upper Arm Blood Pressure Monitor, Panasonic). Synchronization among different DAQ systems was ensured by aligning the starting time recorded by each device.

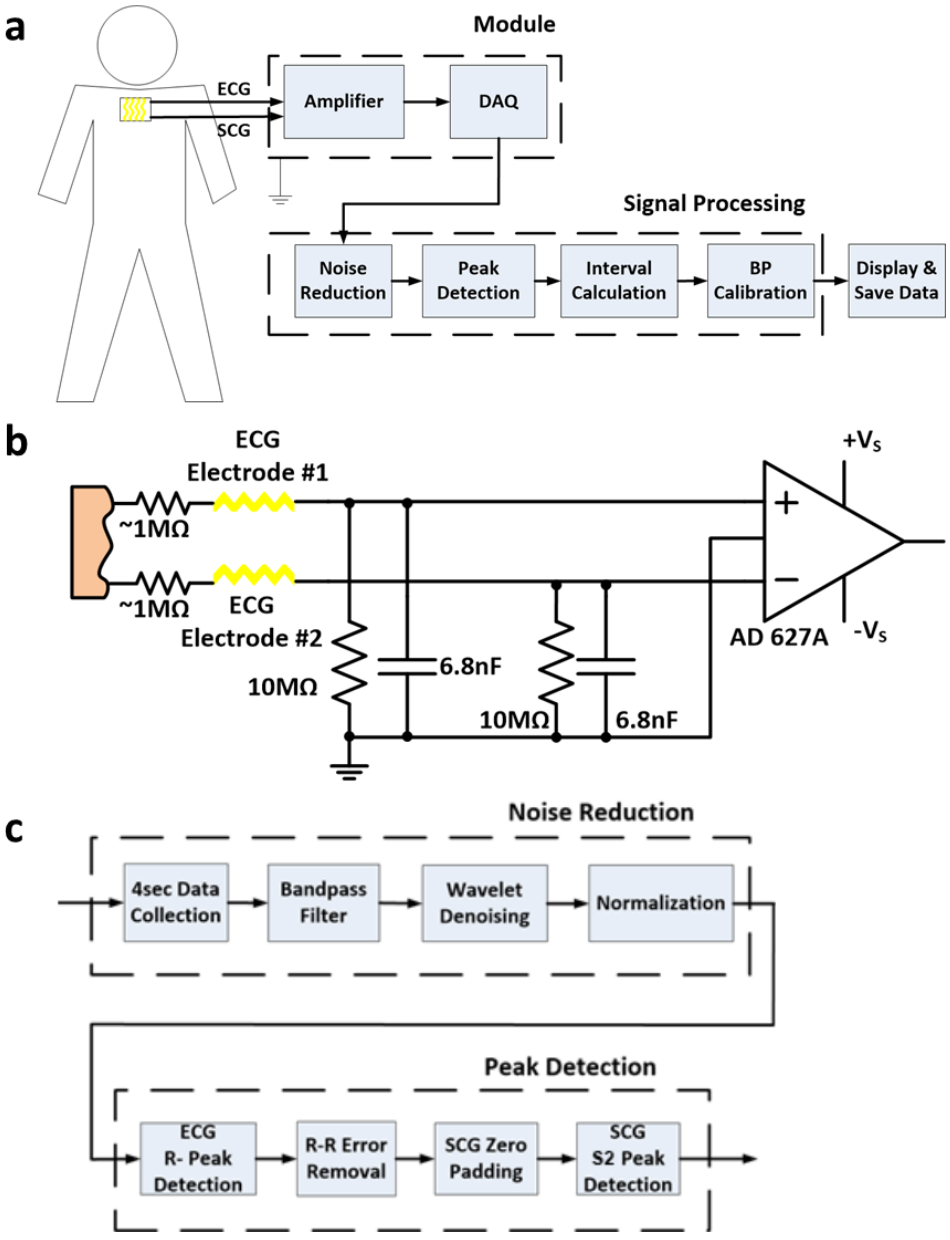

Figure 6.3. Illustrations of the system for ECG and SCG acquisition and signal processing. (a) System flow chart. (b) Custom circuits for ECG measurement. (c) Noise reduction and peak detection algorithm flow chart.

A system for EMAC sensing and BP estimation is described in Fig. 6.3 (a). First, raw ECG signals sensed by the tattoo were first passed through the instrumentation amplifier (AD627A, Analog Devices), which is widely used for its advantages of large common mode noise reduction and high input impedance (Figure 6.3 (b)). The ECG and SCG signals were both acquired by a multichannel NI-6225 DAQ box. After collecting 5 beats of ECG and SCG, the signals were filtered by a 4^{th} order Butterworth band pass filters with the range of 2-40 Hz for ECG and 12-40 Hz for SCG, respectively (Figure 6.3 (c)). Raw and processed ECG and SCG signals from the E-tattoo and the accelerometer are plotted in Fig. 6.4.

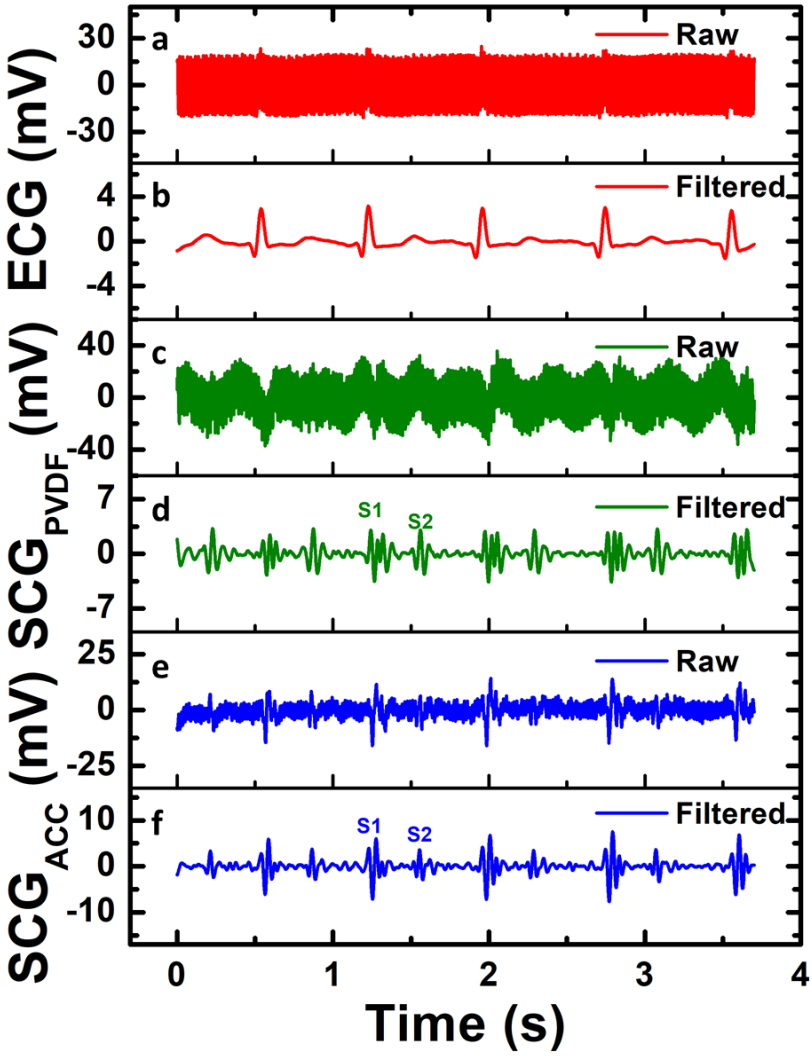

Figure 6.4. Collected and filtered signals from an EMAC sensing tattoo and an accelerometer on the chest. (a) Raw ECG signal measured by a Au/PET sensor. (b) Filtered ECG Signal. (c) Raw SCG measured by a FS PVDF sensor (SCG-PVDF). (d) Filtered SCG-PVDF signal. (e) Raw SCG signal measured by an ADXL-335 accelerometer (SCG-ACC). (f) Filtered SCG-ACC signal.

6.3 RESULTS

6.3.1 Cardiovascular Activities and Correlations

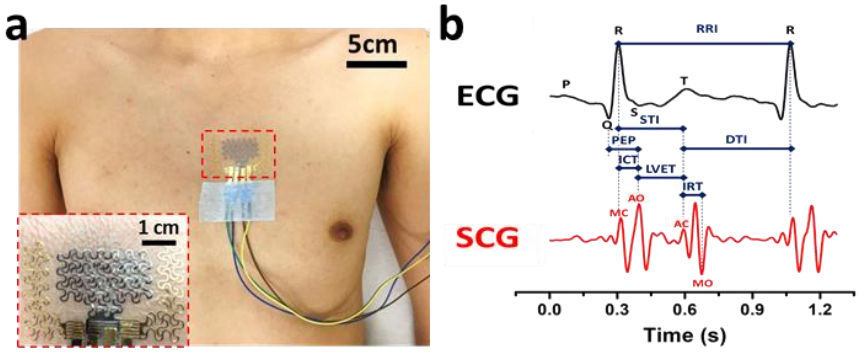

Figure 6.5. (a) A photograph of an EMAC sensing tattoo on the human chest with wire connections. (b) Synchronously measured ECG (navy) and SCG (red) by EMAC tattoo with RAC interval illustrated.

The stretchable EMAC sensing tattoo can be adhered to the human chest as shown in Fig. 6.5 (a). The inset offers a magnified view of the tattoo. Placement of the tattoo was optimized because we discovered that the strongest strain-based SCG signals can be measured near the sternum-chest area [138]. Figure 6.5 (b) displays synchronously measured ECG (black) and SCG (red) signals by the tattoo after signal processing. The DAQ and processing will be described with more details in the next section. The Q, R, and

S peaks of the ECG, and the MC, AO (Aortic valve opening), AC, and MO (Mitral valve opening) peaks of the SCG waveforms are labeled in Fig. 6.5 (b). Among the labeled features, we will focus on the R peak of the ECG and the AC peak of SCG [151, 152]. because the time interval between the R and AC, i.e. the RAC interval, represents systole, which consists of the isovolumetric contraction time (ICT, the time from mitral valve closure to aortic valve opening) and the left ventricular ejection time (LVET, the time between the aortic valve opening and closure) [164]. A Wiggers diagram (Fig. 6.6), which illustrates major cardio-physiological events and their corresponding peaks in ECG and PCG [165], clearly elucidates that the R peak of the ECG is the signature of the closure of the mitral valve [151] and the onset of 2^{nd} PCG feature reflects the closure of the aortic valve, which is identical to the AC peak of SCG [152].

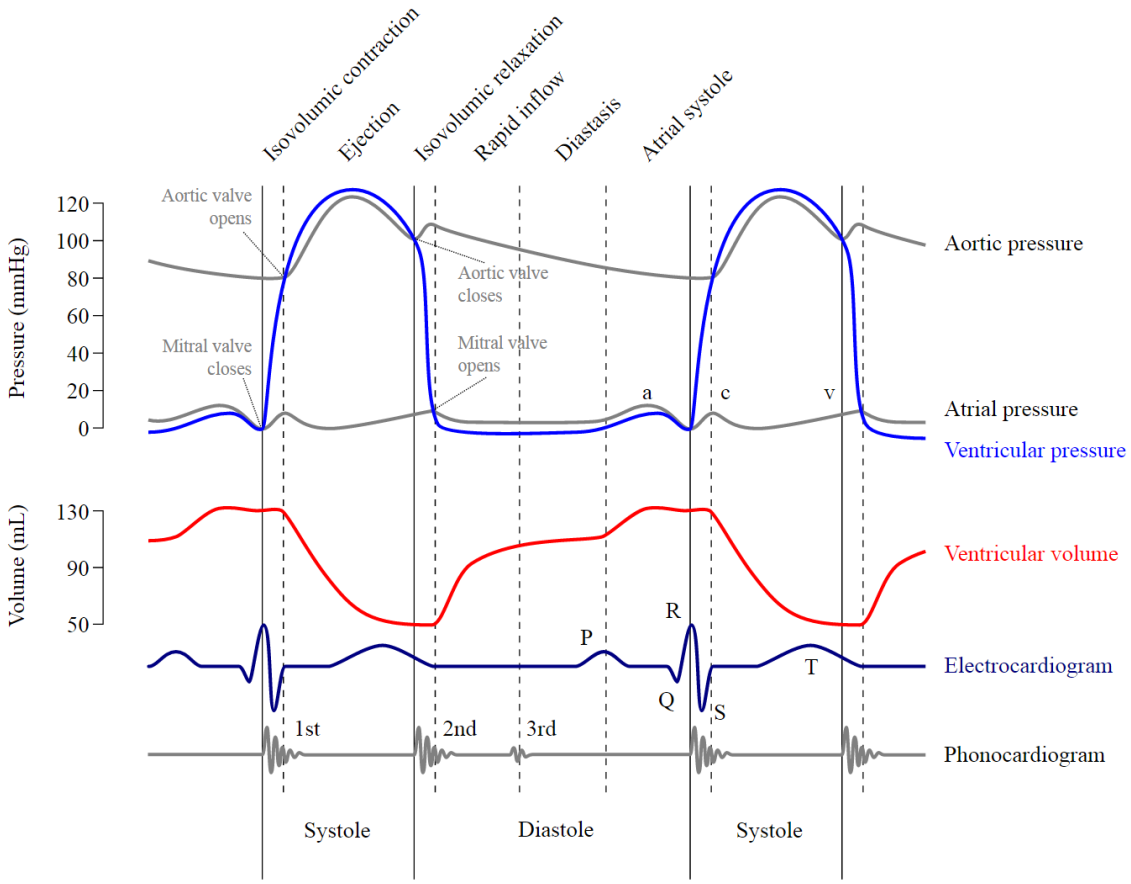

Figure 6.6. Wigger's diagram by DanielChangMD who revised original work of DestinyQx; Redrawn as SVG by xavax, 2012, via Wikimedia Commons. Used under a Creative Commons Attribution-Share Alike 4.0 International license.

To calculate the RAC intervals out of filtered ECG and SCG signals, R peaks from ECG signals were first collected because of their uniqueness. Based on a time of an arbitrary R peak, next R peak within 0.27 seconds (calculated from the maximum possible human heart rate, 220 bpm) were neglected [166]. For each remaining R peak, a correlated

S1 peak was excluded and only a S2 peak was picked up from a period of SCG. Based on the location of S2 peaks, the location of AC peaks was determined. Subsequently, beat-to-beat RAC intervals were attainable, as described in Fig. 6.7 (a). For accurate measurement, mean values of RAC intervals over 5 heartbeats were calculated (Fig. 6.7 (b)) to remove erroneous RAC intervals.

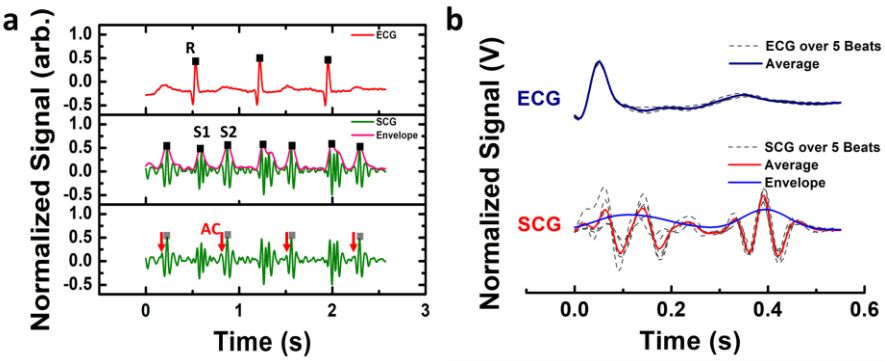

Figure 6.7. (a) RAC interval detection. 1st row) Normalized ECG signal. Black dots indicate R peaks of ECG. 2nd row) Normalized SCG signal. Black dots indicate S1 and S2 peaks of SCG. 3rd row) Normalized, S1-padded SCG signal. Gray dots indicate S2 peaks of SCG only. AC peaks can be detected based on the location of S2 peaks. (b) Averaged ECG and SCG signals over 5 heartbeats.

6.3.2 Correlation between Hemodynamic Parameters and BP

To vary the subject's BP within a short time, we adopted a procedure named the Valsalva maneuver, which is a half-minute test during which the test subject makes a

forceful attempt of exhalation with a closed mouth and nose. Dynamic variation of BP and HR can be observed during such tests [167, 168]. In our experiment, each subject was asked to perform the Valsalva maneuver in a sitting posture, as described in Movie S1 (Supplementary Information). First, SOMNO and the tattoo DAQ were started simultaneously. After 30 seconds of rest with normal breathing, the subject would execute the Valsalva maneuver for 30 seconds, followed by a minute of relaxation with normal breathing. A couple of Valsalva maneuver experiments were repeated with at least a ten-minute break in between for each subject. During those experiments, beat-to-beat SBP and diastolic blood pressure (DBP) were estimated by SOMNO while beat-to-beat RAC intervals were measured by our tattoo via LabView.

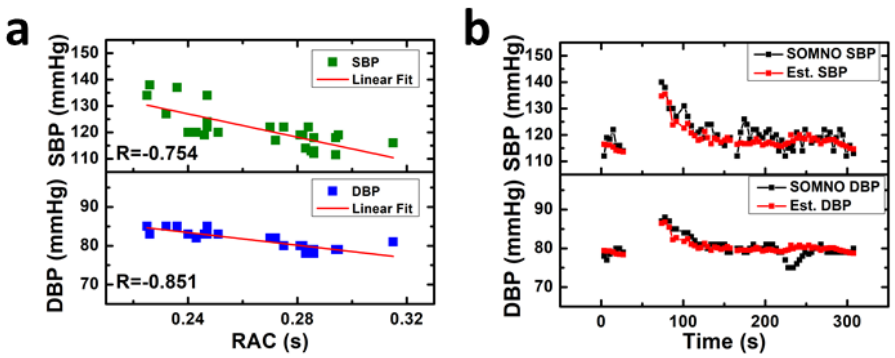

Figure 6.8. (a) The correlation between SBP/DBP measured by SOMNOtouchTM and RAC measured by an EMAC sensing tattoo for a subject, and (b) estimated blood pressure from an independent experiment based on the corresponding calibration.

Four subjects were recruited for the tests and a result from a subject is displayed in Fig. 6.8 (a) and (b). Figure 6.8 (a) shows the correlation between BP and RAC through a linear fit using the formula $y = ax + b$. The correlation coefficient (R) is labeled in the plot. Our results suggest that both SBP and DBP have reasonable negative correlations with RAC, but the fitting parameters and determination coefficients varied among subjects. With the calibration equation obtained for each subject, we can calculate their BP out of the measured RAC in a new set of Valsalva maneuver experiments. Figure 6.8 (b) presents the comparison between BP estimated by the EMAC sensing tattoo vs. SOMNO. Data during the Valsalva maneuver was omitted as both the SOMNO and SCG signals suffered from excessive noise, induced by the shivering of the subject body, as evident in Fig. 6.9. When the subject is at rest, Fig. 6.8 (b) shows reasonably good agreement between the SOMNO and the tattoo. Recognizable mismatches are likely derived from motion or posture change. Results from other subjects can be found in Fig. 6.10 and Table 6.1.

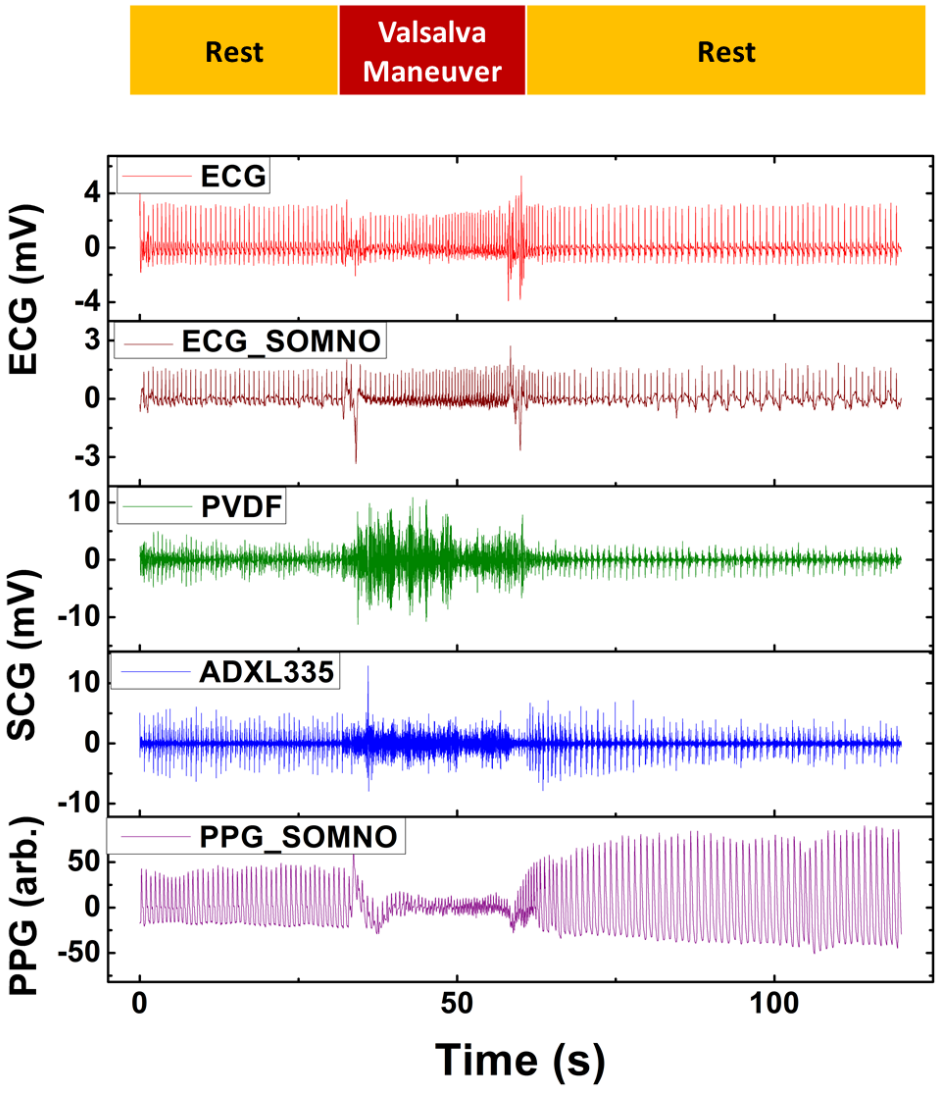

Figure 6.9. Entire ECG, SCG, and PPG signals collected from both EMAC sensing tattoo and SOMNOtouch^{TM} NIBP during the Valsalva maneuver experiment.

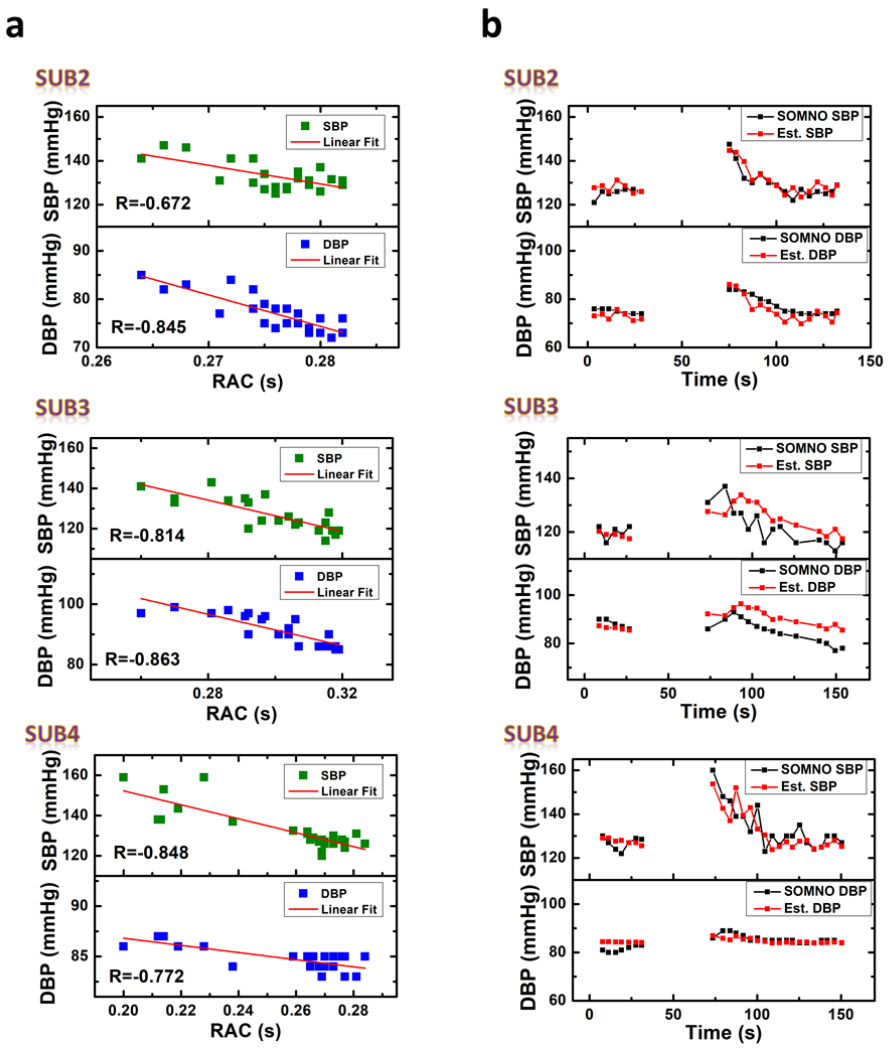

Figure 6.10. (a) SBP/DBP vs RAC correlation chart and its Pearson correlation coefficient (R) from the first experiment of each subject. Red line represents the fitting curve, $y = ax + b$. Fitting parameters of each subject were decided from the chart. (b) Comparison between SBP(DBP) measured by SOMNO NIBP and EMAC sensing patch. Estimated SBP/DBP was calculated as a function of the mean RAC of the second experiment with the fitting parameters of the first experiment.

To study whether there is a general trend of BP vs. RAC, we compiled data for all four subjects in Fig. 6.11 and listed their correlation coefficients in Table 6.1. It is evident that while the compiled SBP and RAC still shows a correlation, the compiled DBP and RAC does not. We also confirmed that the pulse blood pressure (PBP), which is the difference between SBP and DBP, is less pertinent to RAC. Note that we could not derive master fitting parameters for BP estimation from the compiled SBP-RAC plot as there is a huge difference between the overall and individual fitting parameters. Thus, the inference is that there is a unique relationship between RAC and BP for each individual, and calibration for each individual will be necessary, just like the SOMNOtouch™ NIBP.

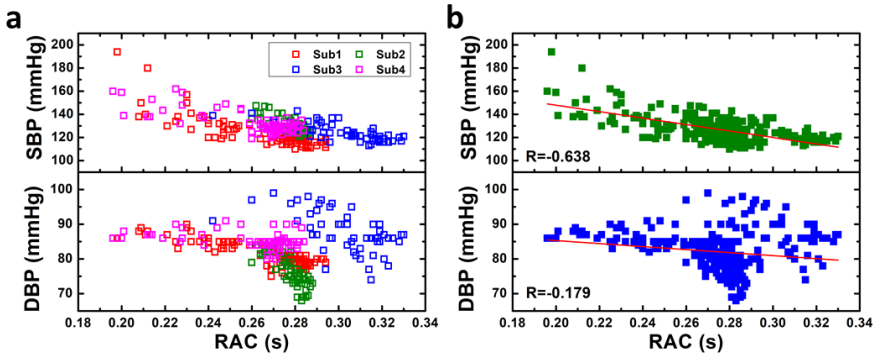

Figure 6.11. (a) SBP/DBP and RAC correlation chart among four different subjects. (b) SBP/DBP and RAC correlation of all subjects.

Subject	SBP,RAC	DBP, RAC	PBP, RAC
Sub1	-0.754	-0.851	-0.618
Sub2	-0.672	-0.845	-0.24
Sub3	-0.814	-0.863	-0.471
Sub4	-0.848	-0.872	-0.823
Average	**-0.772**	**-0.858**	**-0.538**

Table 6.1. Association among SBP(DBP), PBP, RAC

6.4 SUMMARY

A hair thin, self-powered, feather light, highly stretchable, and continuous cardiovascular monitoring device is invented, which can measure ECG and SCG synchronously, and offers a possibility for continuous and unobstructive BP estimation. This stretchable and wearable EMAC sensing tattoo may also be useful in other medical settings where mechano-acoustic signatures are important, such as obstructive sleep apnea.

Chapter 7: Stretchable PVDF Energy Harvester Enhanced by Engraved Electrode

In addition to being stretchable vibration sensors, serpentine-shaped PVDF could also serve as stretchable energy harvester. The stretchability and the electromechanical characteristics of the serpentine PVDF ribbons were evaluated by FEM analysis and experiment. However, due to the co-existence of tensile and compressive strains developed in a serpentine ribbon, charges could cancel out and the electrical output is limited. To eliminate such counter effect, I selectively removed electrode in the regime of compressive strains using a mechanical engraving method. The engraved serpentine ribbon exhibits comparable result with the straight PVDF ribbon in terms of the maximum attainable electrical outputs while maintaining much higher stretchability.

7.1 INTRODUCTION

In the last few decades, emerging research on flexible and stretchable electronics have changed the paradigm of electronic systems. Wearable electronics, innovated from the advancement of flexible and stretchable electronics, are applied in various fields including healthcare [169], entertainment [170], and wireless communication [171]. Flexible and stretchable piezoelectric sensors [61] and energy harvesters [39] are one of the most frequently referred research area because of their simplicity, sustainability, and feasibility with the human body. Although most piezoelectric materials are neither flexible nor stretchable, novel structural approaches enable them to be flexible and stretchable, such as the wavy buckling structure of thin PZT ribbons [37], the woven textile structure of piezoelectric ribbons [172], and electrospun fibers [60]. However,stretchability induced by out-of-plane deformation is limited by the device thickness and the critical curvature. Electrospun fibers intrinsically exhibit excellent stretchability, although the electrode deposition is a challenging issue to achieve higher efficiency.

In previous work, we reported a cardiovascular monitoring device that includes a serpentine structured PVDF piezoelectric film sensor to monitor SCG. By the benefit from its novel structure, the sensor was flexible and stretchable, allowing sufficient conformity onto the chest surface. Even so, we observed that there was a trade-off between stetchability and sensitivity, not only because of the effective stiffness, but also because of the counter charge cancellation effect. As shown in Fig. 7.1, when the serpentine structured piezoelectric ribbon is stretched in plane, the inner curve experiences tension that generates

positive charges, while the outer curve generates compression induced negative charges. The black dot curve shows the boundary between positive and negative charges. As the charges exist on the same side of the electrode, they cancel each other out and result in a diminished electrical output.

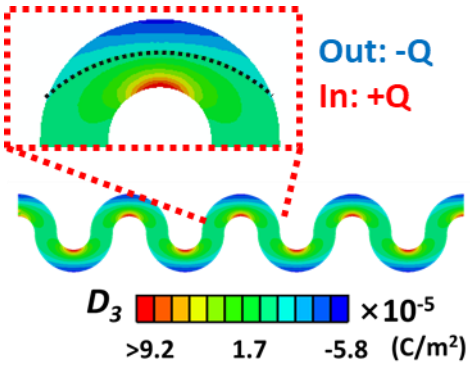

Figure 7.1. Counter charge cancellation effect.

To solve the counter charge cancellation effect without losing the stretchability, we proposed a serpentine structured PVDF film with separated electrodes. By separating electrodes on the inner curve and the outer curve, we can collect charges without experiencing the counter charge effect. In this method, however, the overlapping of the inner electrode and the outer electrode at the intersection point is inevitable. Furthermore, most area of serpentine PVDF experiences positive stress (inner curve) rather than negative stress (outer curve) when stretched. For this reason, we concluded that collecting charges

only from the inner curve of serpentine PVDF is most efficient, in terms of the fabrication method.

To collect charges solely from the inner curve of serpentine PVDF ribbons, the electrode on the outer curve must be excluded. The conventional way of patterning electrodes on a specific area of a sample is to cover a mask on the non-targeted area and deposit metals on the sample. In the case of serpentine ribbons, however, several limitations prohibit such an approach. First, it is inefficient to prepare a mask and deposit metals on a new bare PVDF film, while fully electroded PVDF films are already prepared. Secondly, a bare PVDF film requires extra process, including poling for piezoelectricity and flipping, to deposit electrodes on the top and bottom surfaces. For high-quality devices, well-controlled photolithography and electrode deposition are necessary, while the design suggested above simply requires the disconnection of electrodes from pre-electroded serpentine PVDF ribbons.

Here we suggest an engraving method to scratch out the metal from an electrode surface in a programmed pattern by a cutting machine (Cameo, Silhouette) that costs only $300. By changing the cutter to an engraver, the machine can chisel the surface of metal on a polymer substrate without causing a critical damage. The depth of engraved pattern relies on the number of passes,where each pass can create a trench of depth is less than 1 μm. The width of the trench is roughly 10 μm, and a reasonably controllable pitch is about 100 μm. Using the engraving method, we successfully isolated the electrode surface of the outer curve area from the whole electrode surface. In the following sections, the detailed

fabrication process including engraving method will be introduced. Furthermore, the electrical output generated by the normal serpentine PVDF ribbons and the engraved serpentine PVDF ribbons will be compared by FEM and experiment.

7.2 METHOD

7.2.1 Properties of Normal Serpentine PVDF Ribbons

To investigate electromechanical characteristics of FS PVDF ribbons, the same approach used for measuring characteristics of FS PVDF vibration sensors was performed. we patterned the 28.4-μm-thick commercial PVDF sheet into serpentine ribbons of different widths and sandwiched them by two 47-μm-thick Tegaderm tapes. Uniaxial tensile tests and cyclic tests were conducted to characterize their stretchability and electromechanical behaviors.

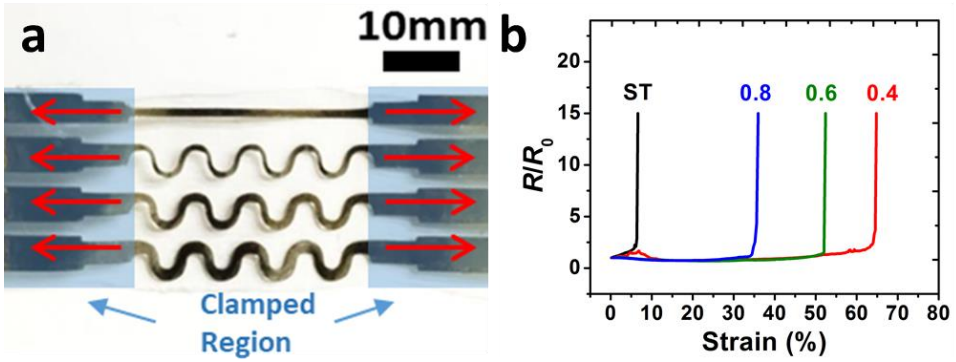

Figure 7.2. (a) Photograph of a straight PVDF ribbon and serpentine PVDF ribbons with different width-to-radius ratios. (b) Stretchability of four PVDF ribbons in terms of the electrode failure.

Figure 7.2 (a) is a photograph showing one straight and three serpentine-shaped PVDF ribbons. The three serpentine ribbons have the same in-plane waviness (radius of curvature R = 2 mm) but different ribbon widths w = 0.8 mm, 1.2 mm, and 1.6 mm. As such, they have different width-to-radius ratios w/R = 0.4, 0.6, 0.8. Existing mechanics models predict that the narrower ribbons should be more stretchable [49, 50]. To test their stretchability, or more precisely, the stretchability of the Ni-Cu electrodes on the top and bottom surfaces of the PVDF ribbons, we adopted a validated method that during stretching, the explosion of electrical resistance can sufficiently indicate the mechanical failure of the metal electrodes [51]. The Tegaderm-sandwiched PVDF ribbons were stretched by RSA-G2 DMA while the electrical resistance of the electrode on one side of the PVDF was measured *in situ* using a Rigol DMM. Figure 7.2 (b) plots the resistance of

PVDF electrodes normalized by their initial resistance (R/R_0) as a function of the applied tensile strain. It is evident that the stretchability of the electrode of the straight PVDF ribbon is only 6.3%, at which point PVDF is still intact. When patterned into serpentine shapes, even the widest ribbon we tested (w/R = 0.8) can be stretched up to 35.5%, which is higher than the widely accepted skin stretchability (20 %). As the width shrinks, the stretchability increases as expected. The narrowest ribbon we tested (w/R = 0.4) can be stretched more than 64.5% without mechanical failure.

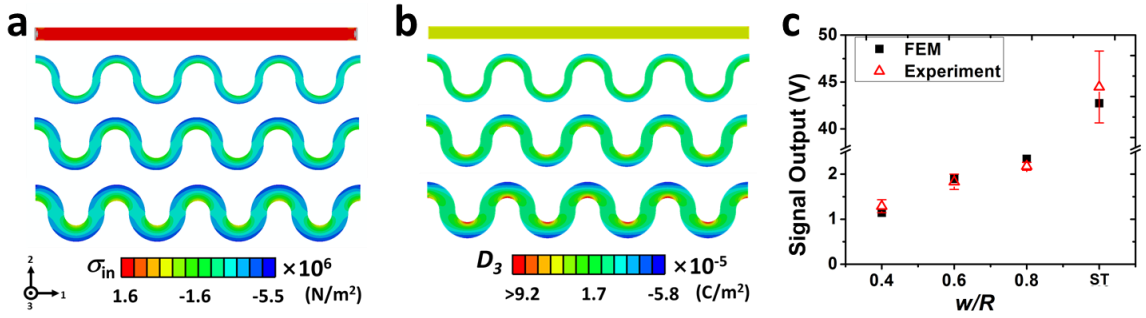

Figure 7.3. FEM simulation result of PVDF ribbons under 0.4 % uniaxial tension by ABAQUS. (a) In plane strain distribution and (b) out of plane polarization distribution. (c) Experiment and FEM comparison of the peak-to-peak voltage output generated from PVDF ribbons under 0-0.4 % uniaxial tension with residual region compensation.

We also performed FEM using ABAQUS to compare with the experimental result. The FEM results of stress and electric displacement distribution are offered in Fig. 7.3 (a) and (b), respectively. By Comparing the two different types of contour plots, we could

identify a strong correlation between stress and electric displacement which was expected as the electric displacement field should be proportional to the sum of in-plane dilatational stress $\sigma_{in} = \sigma_{11} + \sigma_{22}$ under open circuit condition. Figure 7.3 (a) suggests an inverse correlation between the width of the serpentine and stress relief; hence the less electric displacement field as displayed in Fig. 7.3 (b).

In Plotting the experimentally measured and compensated peak-to-peak output voltages (red) and those independently computed by FEM (black) in Fig. 7.3 (c), we found a good relationship between the two sets of data. It is clear that under the same applied strain, the straight ribbons can generate the highest output voltage. In comparison, the output voltage of the serpentine ribbons is one order lower. The output voltage also declines monotonically as the width of the serpentine ribbon decreases. Among serpentines of different widths, the narrower ones are more stretchable, meaning they are under less stress and thus generate less voltage output. However, we expect that serpentine PVDF ribbons can generate comparable voltage with straight PVDF ribbons when they are stretched up to their maximum stretchability, and the maximum attainable voltage is a key factor for stretchable energy harvesting applications.

7.2.2 Counter Charge Cancellation Effect and Electrode Design

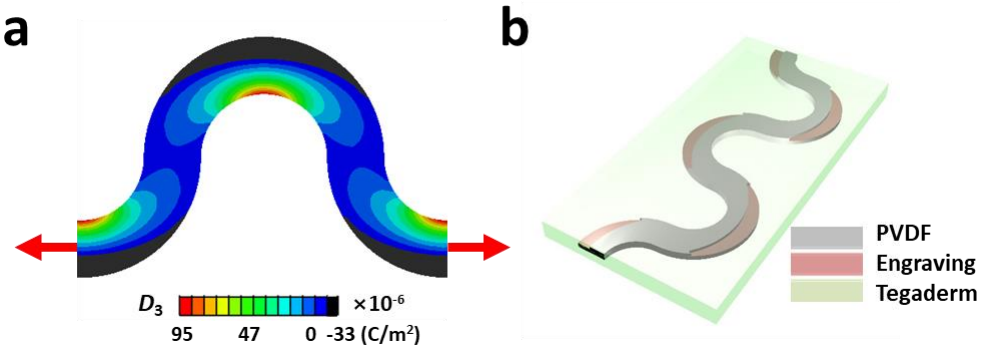

Figure 7.4. (a) Electric displacement FEM of a serpentine PVDF ribbon with w/R=0.625 when it is stretched by 0.4 %. (b) A schematic of the electrode-separated serpentine PVDF ribbon.

As we discussed previously, the trade-off between stretchability and sensitivity of the serpentine PVDF ribbon relies on the effective stiffness, but the counter charge cancellation effect further degrades the electrical output, which can be inhibited by the electrode separation method. The key criterion that determines the dividing line for the electrode separation is finding the boundary where the sign of generated charges is changed. it is difficult to find the boundary from empirical approaches, however, since collected charges are instantly combined and equally distributed over the electrode. Therefore, measurable electrical outputs do not provide any information about originally induced charges. It is for this reason that we determined the boundary from FEM results, which can describe originally induced charges. Figure 7.4 (a) illustrates the electric

displacement FEM result of a serpentine PVDF ribbon of which width-to-radius ratio is 0.625 when it is stretched from 0 to 0.4 %. The setting of the color contour is changed to neglect negative charges so that we can discover the charge-separation boundary. Based on the FEM result in Fig. 7.4 (a), the electrode pattern is designed to collect positive charges only, as described in Fig. 7.4 (b).

7.2.3 Engraving Method

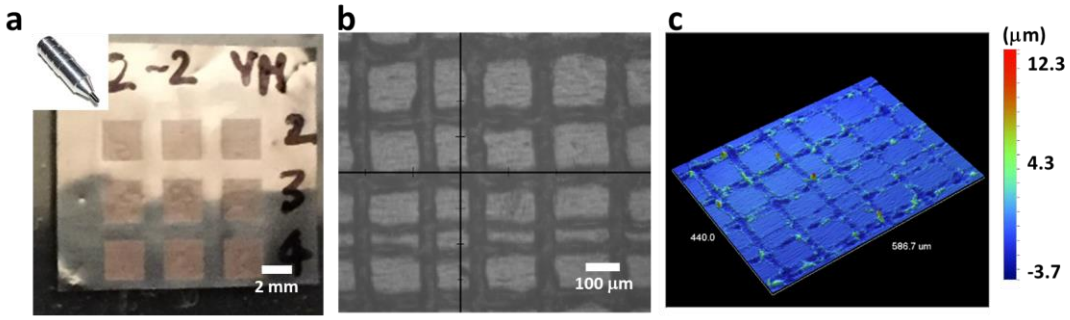

Figure 7.5. Engraving on a PVDF film by a cutting machine. (a) Photograph of an engraved PVDF film. (b) 10x magnified microscope image of the engraved PVDF film. (c) 3D Surface profile of the engraved PVDF film measured by an optical profilometer. Average depth of trenches is about 1 µm.

To separate electrodes with the design derived from the electric displacement FEM result, we utilized the engraving function of the Cameo cutting machine. By changing the tip module from a cutter to a metal engraver (the inset figure in Fig. 7.5 (a)), the cutting machine functioned as a mechanical engraving machine. we also changed the cutting mode to sketch mode through software in order to achieve a higher resolution. The reliable engraving resolution of the pitch in the sketch mode was approximately 100 μm (Fig. 7.5 (b)). Since the target material of the engraving function was the metals, we had to reduce the engraving force by adjusting the mount position of the metal engraver to be higher. The mounting height of the metal engraver was empirically but systematically adjusted by laying several layers of rigid films on the cutting mat right below the tip of the metal engraver, pushing down the module holder, and locking the metal engraver. If the engraving force was still too harsh, more layers of rigid films were added. In this way, we could achieve the engraving force that scratches the surface of metalized PVDF film only about 1 μm for each trace (Fig. 7.5 (c)). The depth of trenches can be deeper by increasing the number of engraving traces by software.

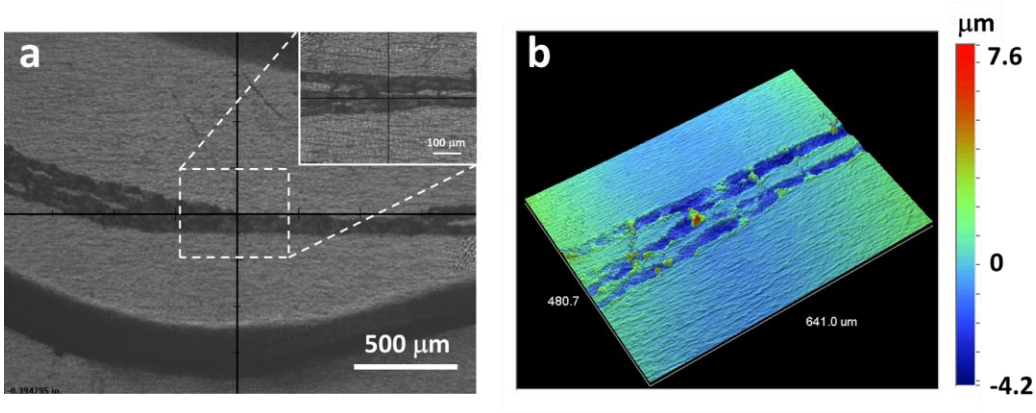

Figure 7.6. (a) Microscope image (x2.55) of engraved ribbon. (inset: x10) (b) 3D Surface profile of the engraved serpentine PVDF ribbon measured by an optical profilometer.

Figure 7.6 (a) shows the microscope image of the engraved serpentine PVDF ribbon manufactured by the optimized engraving and cutting settings of the machine. The inset figure in Fig. 7.6 (a) is the 10x microscope image that magnifies the engraved area of the serpentine PVDF ribbon. The boundary was engraved until the conductivity between separated areas thoroughly disappeared. A couple of engraving were not sufficient to disconnect the separated areas though the engraving depth exceeded the thickness of the electrode (80 nm), as the metal residuals remained on the engraved path. To overcome this issue, two lines were engraved along with the boundary with a 100 µm pitch. Figure 7.6 (b) shows the 3D surface profile of the engraved area, which shows that the boundary was separated by multiple shallow trenches (< 4 µm).

7.3 RESULTS

7.3.1 Comparison between Normal Serpentine PVDF and Engraved Serpentine PVDF Ribbons

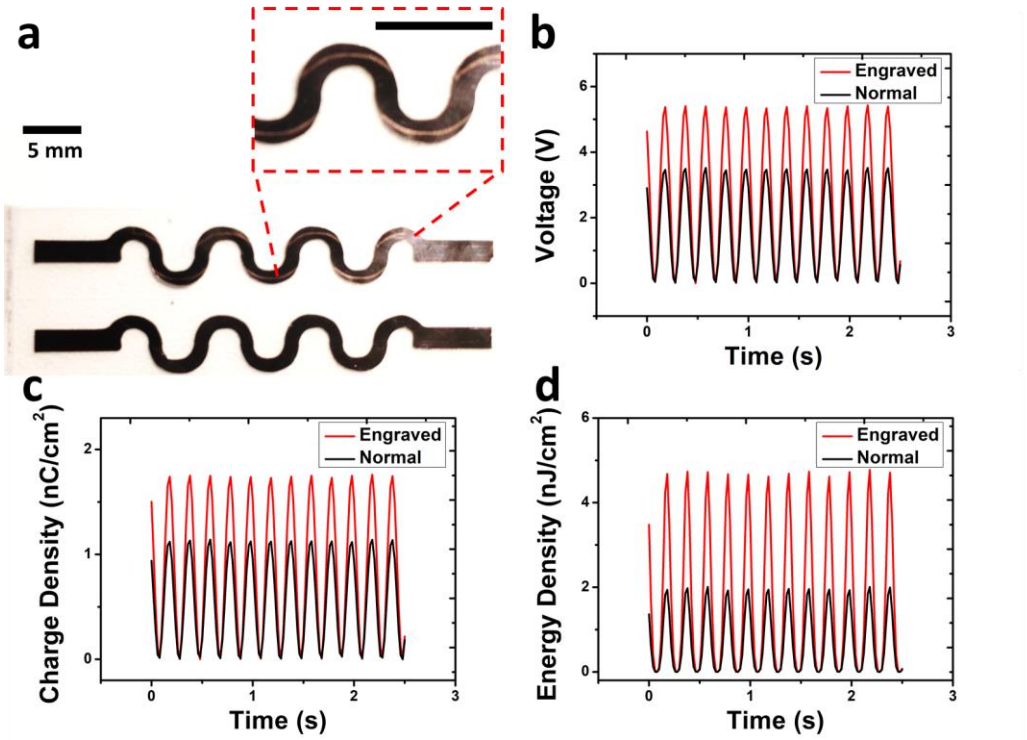

Figure 7.7. (a) Photograph of engraved (top) and normal(bottom) serpentine PVDF ribbons. Scale bar represents 5 mm. (b) Voltage output of normal and engraved serpentine PVDF ribbons from 0 to 0.4 % strain. (c) Charge density output of normal and engraved serpentine PVDF ribbons from 0 to 0.4 % strain. (d) Energy density output of normal and engraved serpentine PVDF ribbons from 0 to 0.4 % strain.

To confirm the counter charge cancellation effect by experiment and measure the improvement in electrical outputs, we prepared the engraved serpentine PVDF ribbon and the normal serpentine PVDF ribbon, which have the equivalent geometry, as shown in Fig. 7.7 (a). The radius, width-to-radius ratio, and thickness of two ribbons were 2 mm, 0.625, and 28 μm, respectively. The samples were then sandwiched by Tegaderm (7 MPa, 47 μm) and Hydrocolloidal Tegaderm (3.5 MPa, 300 μm) to insulate samples and suppress the out-of-plane buckling. Before the encapsulation, the top and the bottom electrode surfaces were connected to Au/PET extension electrodes. Similar to Section 7.2.1, we measured the voltage output of the two samples when samples were stretched by DMA with strain from 0 to 0.4 %. Figure 7.7 (b), (c), and (d) shows the result of electrical outputs from the normal serpentine PVDF ribbon and the engraved serpentine PVDF ribbon. The voltage amplitude of the normal ribbon and the engraved ribbon at the strain of 0.4 % were 3.34 V and 5.38 V, respectively (Fig. 7.7 (b)). To ensure the experimental result is valid, we also derived the voltage output from FEM, which were 3.21 V and 5.27 V for the normal ribbon and the engraved ribbon, respectively, which are similar to experiment results. The charge density output was calculated from $\rho = CV/A$, where the *C/A* (capacitance per area) is 324 pF/cm^2. Subsequently, the charge density output of the normal ribbon and the engraved ribbon at the strain of 0.4 % were 1.76 nC/cm^2 and 1.14 nC/cm^2 (Fig. 7.7 (c)). It is worthwhile to mention that the generated charge density output increased, which implies that the counter charge cancellation effect diminished the generated output charge for the normal case. Figure 7.7 (d) shows the energy density output calculated from $U = \rho V/2$.

The peak energy density output generated from the engraved ribbon was 4.78 nJ, which is more than the twice of the energy density generated from the normal ribbon (2.01 nJ). As can be seen, a simple engraving method doubled the energy generation of the serpentine PVDF ribbon without changing its mechanical properties.

7.3.2 Energy Harvesting Estimation

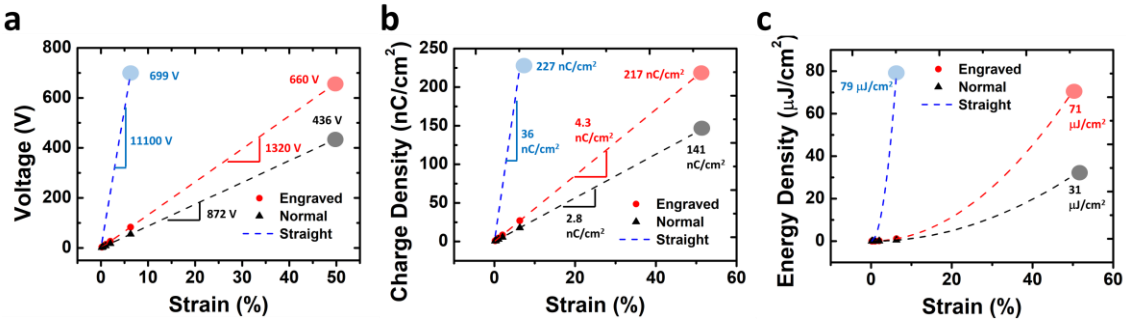

Figure 7.8. Strain-induced (a) voltage, (b) charge density, and (c) energy density output of straight, normal, and engraved serpentine PVDF ribbons.

Using DMA, we changed the applied strain to serpentine PVDF ribbons from 0.2% to 2% and measured the voltage output, as described in Fig. 7.8. Based on the experimental result, the mechano-electrical sensitivity of serpentine ribbons was obtained, which are 1320 V per strain for the engraved ribbon and 872 V per strain for normal ribbons. Although the sensitivity was improved by 50 % from the normal ribbon to the engraved ribbon, the sensitivity of the engraved ribbon was still only 12 % of the straight ribbon, of

which sensitivity is 11100 V per strain. However, it is more reasonable to compare the maximum attainable voltage with respect to stretchability. Assuming the voltage per strain is linear, we can estimate the output voltage at the maximum strain of serpentine PVDF ribbons without the electrode rupture. For the serpentine PVDF ribbons of which width-to-radius ratio is 0.625, the maximum strain without the electrode failure is roughly 50 %, while the straight PVDF ribbon can stretchable up to 6.3 %. Consequently, the maximum attainable voltage of the engraved serpentine PVDF ribbon is 660 V, which is comparable with the straight ribbon, of which maximum attainable voltage is 699 V. Similarly, the maximum attainable charge density and energy density of the engraved serpentine PVDF ribbon are 217 nC/cm^2 and 71 $\mu J/cm^2$, which are similar to the straight PVDF ribbon. However, in terms of the efficiency of the device within a limited area, the straight PVDF ribbon has much higher efficiency than serpentine ribbons. the serpentine PVDF ribbon should be minimized and placed as an array to increase the area efficiency.

7.4 SUMMARY

The engraved serpentine ribbon was created by the economical cutting machine and the engraving method, to suppress the counter charge cancellation effect. The result the electromechanical response experiment shows that the engraved serpentine PVDF ribbon exhibited 2.5 times higher energy density than the normal serpentine PVDF ribbon. Considering the maximum attainable energy density, the engraved serpentine PVDF ribbon

was comparable with the straight PVDF ribbon. In conclusion, we could increase the energy generation efficiency by simple manufacturing method. This work will suggest a way to develop an efficient and low cost in-plane stretchable energy harvester.

Chapter 8: Conclusions and Future Work

In this chapter, the dissertation is summarized and some future ideas are suggested.

8.1 CONCLUSIONS

Recalling Chapter 1, the purpose of this dissertation is to develop bio-integrated devices made of PVDF via a simple and cost-effective manufacturing method, examine the devices on human subjects, and optimize the device design. First, basic electromechanical properties of PVDF were measured for further applications and the theoretical frameworks for PVDF unimorph under various boundary conditions were analyzed. As a practical bio-integrated device made of PVDF, the filamentary serpentine PVDF vibration sensor was created to monitor SCG on the surface of the human chest. The sensor performance of monitoring SCG signals was comparable with a commercial accelerometer. Furthermore, the dual sensor method was used to cancel out the motion artifact while measuring SCG signals. The motion artifact such as shaking legs were eliminated while SCG signals were cleanly captured. To optimize the location of SCG on the chest, full-field SCG was visualized via the 3D DIC method. The sternum seems the best location for capturing both S1 and S2 features. The effect of the substrate stiffness to the sensitivity of FS PVDF sensor was also validated; The stiffer the substrate, the lower the signal-to-noise ratio of SCG. Integrated with ECG sensors made of Au/PET, FS PVDF SCG sensor was used for cardiovascular monitoring. Using E-tattoo for electro- and mechano-acoustic cardiovascular monitoring (EMAC) and the correlation between the systolic interval and the blood pressure, the blood pressure of four subjects were successfully estimated. Lastly, stretchable PVDF energy harvester was developed based on the serpentine structure and

improved by suppressing the counter charge cancellation effect. A simple engraving method was applied to separate the electrodes.

In conclusion, my research provides systematic and empirical criteria to design bio-integrated devices made of PVDF such as a vibration sensor for SCG and a stretchable energy harvester. The performance of devices was systematically investigated through numerical analysis and experimentation. For high throughput and low-cost manufacturing process of devices, a novel fabrication method was developed such as the engraving method, based on the "cut-and-paste" method. The performance of E-tattoo for EMAC sensing made of PVDF was demonstrated as a blood pressure estimation device via testing on human subjects. As a different application, a stretchable PVDF energy harvester was developed, which was enhanced by the electrode separation to reduce the counter charge cancellation effect.

8.2 FUTURE WORK

Related to the results of the research in this dissertation, several thoughts and questions remain for further studies. First, bio-integrated devices must be wireless to realize a genuine unobstructive system. Near field communication technology might be the closest available solution for now, while stretchable, highly efficient batteries and energy harvesters with low-power wireless communication devices can also be an innovative solution for wireless bio-integrated devices.

For mechanical problems, the analytical solutions for the buckling and post buckling of serpentine structures will be beneficial to design a stretchable device under a large strain. For piezoelectric devices with serpentine structures, it is a critical issue since the energy relief via buckling reduces electrical energy output, which is hardly predictable with the linear, non-buckling analytical solution.

In terms of the blood pressure estimation using bio-integrated EMAC sensing system, various cardiovascular parameters must be considered, as the given BP-STI correlation model is excessively simplified and may not reflect a sophisticated control mechanism of the human cardiovascular system. Many scholars are working on modeling the cardiovascular system, yet it is applicable to explain real nature of living organs. In this case, the machine learning may be a solution for developing a successful BP estimation derived from various cardiovascular factors including BP-STI correlation. For this work, however, a tremendous reliable data of cardiovascular factors, which requires a high quality of sensing system and the cooperation with a medical department, are mandatory.

When it comes to PVDF applications, it might be worthy to research the feasibility of PVDF actuator. On one hand, piezoelectric materials are less considerable as actuators due to their low electrical-to-mechanical transduction efficiency at a large scale. For small scale and low power devices, on the other hand, piezoelectric actuators are more efficient than electro-magnetic motors [173]. There are several types of piezoelectric actuators, including stacked piezo actuators [174], traveling wave motors [175, 176], and inch-worm actuators [177]. Although few researchers reported about flexible actuators made out of

piezoelectric materials [178], piezoelectric soft, flexible, and stretchable actuators have not been discussed as much as sensors or energy harvesters. Mimicking a bio-structure may provide a feasible or efficient approach to increase the functionality of soft actuators. Although the fabrication and the miniaturization of the actuator would be challenging, the soft actuator can be used in many fields.

References

[1] F. Jiao, C.-a. Di, Y. Sun, P. Sheng, W. Xu, and D. Zhu, "Inkjet-printed flexible organic thin-film thermoelectric devices based on p-and n-type poly (metal 1, 1, 2, 2-ethenetetrathiolate) s/polymer composites through ball-milling," *Phil. Trans. R. Soc. A,* vol. 372, p. 20130008, 2014.

[2] D. Shen, M. Xiao, G. Zou, L. Liu, W. W. Duley, and Y. N. Zhou, "Wearable Electronics: Self-Powered Wearable Electronics Based on Moisture Enabled Electricity Generation (Adv. Mater. 18/2018)," *Advanced Materials,* vol. 30, 2018.

[3] W. Wu, S. Bai, M. Yuan, Y. Qin, Z. L. Wang, and T. Jing, "Lead zirconate titanate nanowire textile nanogenerator for wearable energy-harvesting and self-powered devices," *ACS nano,* vol. 6, pp. 6231-6235, 2012.

[4] S. Wang, Y. Xie, S. Niu, L. Lin, and Z. L. Wang, "Freestanding triboelectric-layer-based nanogenerators for harvesting energy from a moving object or human motion in contact and non-contact modes," *Advanced Materials,* vol. 26, pp. 2818-2824, 2014.

[5] F.-R. Fan, Z.-Q. Tian, and Z. L. Wang, "Flexible triboelectric generator," *Nano energy,* vol. 1, pp. 328-334, 2012.

[6] Q. Zheng, H. Zhang, B. Shi, X. Xue, Z. Liu, Y. Jin*, et al.*, "In vivo self-powered wireless cardiac monitoring via implantable triboelectric nanogenerator," *ACS nano,* vol. 10, pp. 6510-6518, 2016.

[7] Q. Zheng, B. Shi, F. Fan, X. Wang, L. Yan, W. Yuan*, et al.*, "In vivo powering of pacemaker by breathing-driven implanted triboelectric nanogenerator," *Advanced Materials,* vol. 26, pp. 5851-5856, 2014.

[8] A. Delnavaz and J. Voix, "Flexible piezoelectric energy harvesting from jaw movements," *Smart Materials and Structures,* vol. 23, p. 105020, 2014.

[9] S. Schneegass and O. Amft, "Energy Harvesting Smart Textiles," in *Smart Textiles*, ed: Springer, 2017.

[10] Q. Zheng, B. Shi, Z. Li, and Z. L. Wang, "Recent progress on piezoelectric and triboelectric energy harvesters in biomedical systems," *Advanced Science,* 2017.

[11] T. Kobayashi, T. Yamashita, N. Makimoto, S. Takamatsu, and T. Itoh, "Ultra-thin piezoelectric strain sensor 5× 5 array integrated on flexible printed circuit for structural health monitoring by 2D dynamic strain sensing," in *Micro Electro Mechanical Systems (MEMS), 2016 IEEE 29th International Conference on*, 2016, pp. 1030-1033.

[12] K. Lu, W. Huang, J. Guo, T. Gong, X. Wei, B.-W. Lu*, et al.*, "Ultra-Sensitive Strain Sensor Based on Flexible Poly (vinylidene fluoride) Piezoelectric Film," *Nanoscale research letters,* vol. 13, p. 83, 2018.

[13] W. Choi, J. Lee, Y. Kyoung Yoo, S. Kang, J. Kim, and J. Hoon Lee, "Enhanced sensitivity of piezoelectric pressure sensor with microstructured polydimethylsiloxane layer," *Applied Physics Letters,* vol. 104, p. 123701, 2014.

[14] J. H. Lee, H. J. Yoon, T. Y. Kim, M. K. Gupta, J. H. Lee, W. Seung*, et al.*, "Micropatterned P (VDF-TrFE) Film-Based Piezoelectric Nanogenerators for Highly Sensitive Self-Powered Pressure Sensors," *Advanced Functional Materials,* vol. 25, pp. 3203-3209, 2015.
[15] Q. Shi, T. Wang, and C. Lee, "MEMS based broadband piezoelectric ultrasonic energy harvester (PUEH) for enabling self-powered implantable biomedical devices," *Scientific reports,* vol. 6, p. 24946, 2016.
[16] Z. Chen, X. Song, L. Lei, X. Chen, C. Fei, C. T. Chiu*, et al.*, "3D printing of piezoelectric element for energy focusing and ultrasonic sensing," *Nano Energy,* vol. 27, pp. 78-86, 2016.
[17] J. Li, X. Zhou, H. Zhao, M. Shao, P. Hou, and X. Xu, "Design and experimental performances of a piezoelectric linear actuator by means of lateral motion," *Smart materials and structures,* vol. 24, p. 065007, 2015.
[18] J. Li, R. Sedaghati, J. Dargahi, and D. Waechter, "Design and development of a new piezoelectric linear Inchworm® actuator," *Mechatronics,* vol. 15, pp. 651-681, 2005.
[19] T. Karaki, K. Yan, and M. Adachi, "Subgrain microstructure in high-performance BaTiO3 piezoelectric ceramics," *Applied physics express,* vol. 1, p. 111402, 2008.
[20] B. Jaffe, *Piezoelectric ceramics* vol. 3: Elsevier, 2012.
[21] Z. L. Wang and J. Song, "Piezoelectric nanogenerators based on zinc oxide nanowire arrays," *Science,* vol. 312, pp. 242-246, 2006.
[22] E. Vogel, "Technology and metrology of new electronic materials and devices," *Nature nanotechnology,* vol. 2, p. 25, 2007.
[23] T. Akiba, H. Bennetto, J. Stirling, and K. Tanaka, "Electricity production from alkalophilic organisms," *Biotechnology letters,* vol. 9, pp. 611-616, 1987.
[24] H. Kawai, "Piezoelectricity of Poly (Vinylidene Fluoride)," *Japanese Journal of Applied Physics,* vol. 8, pp. 975-&, 1969.
[25] M. Paajanen, J. Lekkala, and K. Kirjavainen, "ElectroMechanical Film (EMFi) - a new multipurpose electret material," *Sensors and Actuators a-Physical,* vol. 84, pp. 95-102, Aug 1 2000.
[26] K. S. Ramadan, D. Sameoto, and S. Evoy, "A review of piezoelectric polymers as functional materials for electromechanical transducers," *Smart Materials and Structures,* vol. 23, p. 033001, Mar 2014.
[27] "Introduction to Piezoelectric Actuators and Transducers," International Center for Actuators and Transducers, Penn State University, University Park, PA 168022003.
[28] J. Tichy, *Fundamentals of piezoelectric sensorics : mechanical, dielectric, and thermodynamical properties of piezoelectric materials*, 1st ed. New York: Springer, 2010.
[29] Y. Jung, *Piezoelectric Energy Harvesting Prospects and Latest Technological Trends*. Seoul, South Korea: Ha-Yeon, 2012.

[30] I. Patel, "Ceramic Based Intelligent Piezoelectric Energy Harvesting Device," in *Advances in Ceramics - Electric adn Magnetic Ceramics, Bioceramics, Ceramics and Environment*, C. Sikalidis, Ed., ed Rijeka, Croatia: InTech, 2011.

[31] H. Wu, Y. A. Huang, F. Xu, Y. Q. Duan, and Z. P. Yin, "Energy Harvesters for Wearable and Stretchable Electronics: From Flexibility to Stretchability," *Advanced Materials,* vol. 28, pp. 9881-9919, Dec 7 2016.

[32] C. Dagdeviren, B. D. Yang, Y. W. Su, P. L. Tran, P. Joe, E. Anderson*, et al.*, "Conformal piezoelectric energy harvesting and storage from motions of the heart, lung, and diaphragm," *Proceedings of the National Academy of Sciences of the United States of America,* vol. 111, pp. 1927-1932, Feb 4 2014.

[33] S. I. Park, J. H. Ahn, X. Feng, S. Wang, Y. Huang, and J. A. Rogers, "Theoretical and experimental studies of bending of inorganic electronic materials on plastic substrates," *Advanced Functional Materials,* vol. 18, pp. 2673-2684, 2008.

[34] D.-H. Kim, J.-H. Ahn, W. M. Choi, H.-S. Kim, T.-H. Kim, J. Song*, et al.*, "Stretchable and foldable silicon integrated circuits," *Science,* vol. 320, pp. 507-511, 2008.

[35] S. P. Lacour, J. Jones, S. Wagner, T. Li, and Z. Suo, "Stretchable interconnects for elastic electronic surfaces," *Proceedings of the IEEE,* vol. 93, pp. 1459-1467, 2005.

[36] Y. Liu, M. Pharr, and G. A. Salvatore, "Lab-on-skin: a review of flexible and stretchable electronics for wearable health monitoring," *ACS nano,* vol. 11, pp. 9614-9635, 2017.

[37] Y. Qi, J. Kim, T. D. Nguyen, B. Lisko, P. K. Purohit, and M. C. McAlpine, "Enhanced piezoelectricity and stretchability in energy harvesting devices fabricated from buckled PZT ribbons," *Nano letters,* vol. 11, pp. 1331-1336, 2011.

[38] X. Feng, B. D. Yang, Y. Liu, Y. Wang, C. Dagdeviren, Z. Liu*, et al.*, "Stretchable ferroelectric nanoribbons with wavy configurations on elastomeric substrates," *Acs Nano,* vol. 5, pp. 3326-3332, 2011.

[39] J. H. Lee, K. Y. Lee, M. K. Gupta, T. Y. Kim, D. Y. Lee, J. Oh*, et al.*, "Highly Stretchable Piezoelectric-Pyroelectric Hybrid Nanogenerator," *Advanced Materials,* vol. 26, pp. 765-769, Feb 5 2014.

[40] H. Khan, A. Razmjou, M. Ebrahimi Warkiani, A. Kottapalli, and M. Asadnia, "Sensitive and Flexible Polymeric Strain Sensor for Accurate Human Motion Monitoring," *Sensors,* vol. 18, p. 418, 2018.

[41] D. Chen, M. Hang, K. Chen, K. Brown, and J. X. Zhang, "Piezoelectric PVDF thin films with asymmetric microporous structures for pressure sensing," in *SENSORS, 2015 IEEE*, 2015, pp. 1-4.

[42] N. A. Hoque, P. Thakur, S. Roy, A. Kool, B. Bagchi, P. Biswas*, et al.*, "Er3+/Fe3+ Stimulated Electroactive, Visible Light Emitting, and High Dielectric Flexible PVDF Film Based Piezoelectric Nanogenerators: A Simple and Superior Self-Powered Energy Harvester with Remarkable Power Density," *ACS applied materials & interfaces,* vol. 9, pp. 23048-23059, 2017.

[43] H. Shaik, S. Rachith, K. Rudresh, A. S. Sheik, K. T. Raman, P. Kondaiah*, et al.*, "Towards β-phase formation probability in spin coated PVDF thin films," *Journal of Polymer Research,* vol. 24, p. 35, 2017.
[44] Y. Duan, Y. Ding, J. Bian, Z. Xu, Z. Yin, and Y. Huang, "Ultra-Stretchable Piezoelectric Nanogenerators via Large-Scale Aligned Fractal Inspired Micro/Nanofibers," *Polymers,* vol. 9, p. 714, 2017.
[45] R. I. Haque, R. Vié, M. Germainy, L. Valbin, P. Benaben, and X. Boddaert, "Inkjet printing of high molecular weight PVDF-TrFE for flexible electronics," *Flexible and Printed Electronics,* vol. 1, p. 015001, 2015.
[46] S. X. Yang, Y. C. Chen, L. Nicolini, P. Pasupathy, J. Sacks, B. Su*, et al.*, ""Cut-and-Paste" Manufacture of Multiparametric Epidermal Sensor Systems," *Advanced Materials,* vol. 27, pp. 6423-+, Nov 4 2015.
[47] J. C. P. Curie, "Dévelopment, par pression, de l'électricité polaire dans les cristaux hémièdres
à faces inclinées.," *C. R. Acad. Sci.,* vol. 91, pp. 294–295 1880.
[48] L. Pinna, R. S. Dahiya, F. De Nisi, M. Valle, and Ieee, "Analysis of Self-Powered Vibration-Based Energy Scavenging System," *Ieee International Symposium on Industrial Electronics (Isie 2010),* pp. 402-408, 2010.
[49] H. Allik, K. M. Webman, and J. T. Hunt, "VIBRATIONAL RESPONSE OF SONAR TRANSDUCERS USING PIEZOELECTRIC FINITE-ELEMENTS," *Journal of the Acoustical Society of America,* vol. 56, pp. 1782-1791, 1974.
[50] D. K. Cheng, *Fundamentals of engineering electromagnetics*. Reading, Mass.: Addison-Wesley Pub. Co., 1993.
[51] R. S. Dahiya, *Robotic tactile sensing : technologies and system*, 1st ed. New York: Springer, 2012.
[52] T. Ma, Y. Wang, R. Tang, H. Yu, and H. Jiang, "Pre-patterned ZnO nanoribbons on soft substrates for stretchable energy harvesting applications," *Journal of Applied Physics,* vol. 113, p. 204503, 2013.
[53] C. Dagdeviren, Y. Shi, P. Joe, R. Ghaffari, G. Balooch, K. Usgaonkar*, et al.*, "Conformal piezoelectric systems for clinical and experimental characterization of soft tissue biomechanics," *Nature materials,* vol. 14, pp. 728-736, 2015.
[54] H. Kawai, "The piezoelectricity of PVDF," *Jpn. J. Appl. Phys.,* vol. 8, pp. 975–976, 1969.
[55] R. S. Dahiya, L. Lorenzelli, G. Metta, M. Valle, and Ieee, "POSFET Devices Based Tactile Sensing Arrays," *2010 Ieee International Symposium on Circuits and Systems,* pp. 893-896, 2010.
[56] M. Specialties, "Piezo Film Sensors Technical Manual," *Measurement,* 2013.
[57] G. Laroche, Y. Marois, R. Guidoin, M. W. King, L. Martin, T. How*, et al.*, "Polyvinylidene Fluoride (Pvdf) as a Biomaterial - from Polymeric Raw-Material to Monofilament Vascular Suture," *Journal of Biomedical Materials Research,* vol. 29, pp. 1525-1536, Dec 1995.

[58] W. Y. L. Lionel and G. K. Fedder, "Elastic ribbon-like piezoelectric energy harvester for wearable devices with stretchable surfaces," *2016 38th Annual International Conference of the Ieee Engineering in Medicine and Biology Society (Embc),* pp. 4816-4819, 2016.

[59] W. Dong, L. Xiao, W. Hu, C. Zhu, Y. Huang, and Z. Yin, "Wearable human–machine interface based on PVDF piezoelectric sensor," *Transactions of the Institute of Measurement and Control,* vol. 39, pp. 398-403, 2017.

[60] L. Persano, C. Dagdeviren, Y. W. Su, Y. H. Zhang, S. Girardo, D. Pisignano*, et al.*, "High performance piezoelectric devices based on aligned arrays of nanofibers of poly(vinylidenefluoride-co-trifluoroethylene)," *Nature Communications,* vol. 4, Mar 2013.

[61] Y. Q. Duan, Y. A. Huang, Z. P. Yin, N. B. Bu, and W. T. Dong, "Non-wrinkled, highly stretchable piezoelectric devices by electrohydrodynamic direct-writing," *Nanoscale,* vol. 6, pp. 3289-3295, 2014.

[62] C. E. Chang, V. H. Tran, J. B. Wang, Y. K. Fuh, and L. W. Lin, "Direct-Write Piezoelectric Polymeric Nanogenerator with High Energy Conversion Efficiency," *Nano Letters,* vol. 10, pp. 726-731, Feb 2010.

[63] Y. Zhao, W. Yang, Y. Zhou, Y. Chen, X. Cao, Y. Yang*, et al.*, "Effect of crystalline phase on the dielectric and energy storage properties of poly (vinylidene fluoride)," *Journal of Materials Science: Materials in Electronics,* vol. 27, pp. 7280-7286, 2016.

[64] M. E. Lines and A. M. Glass, *Principles and applications of ferroelectrics and related materials*: Oxford university press, 1977.

[65] J. Sirohi and I. Chopra, "Fundamental understanding of piezoelectric strain sensors," *Journal of Intelligent Material Systems and Structures,* vol. 11, pp. 246-257, Apr 2000.

[66] J. K. Yuan, Z. M. Dang, S. H. Yao, J. W. Zha, T. Zhou, S. T. Li*, et al.*, "Fabrication and dielectric properties of advanced high permittivity polyaniline/poly(vinylidene fluoride) nanohybrid films with high energy storage density," *Journal of Materials Chemistry,* vol. 20, pp. 2441-2447, 2010.

[67] W. Heywang, K. Lubitz, and W. Wersing, *Piezoelectricity: evolution and future of a technology* vol. 114: Springer Science & Business Media, 2008.

[68] H. S. Nalwa, *Ferroelectric polymers : chemistry, physics, and applications*. New York: M. Dekker, Inc., 1995.

[69] H. Wang, Q. M. Zhang, L. E. Cross, and A. O. Sykes, "Piezoelectric, Dielectric, and Elastic Properties of Poly(Vinylidene Fluoride Trifluoroethylene)," *Journal of Applied Physics,* vol. 74, pp. 3394-3398, Sep 1 1993.

[70] M. Li, I. Katsouras, C. Piliego, G. Glasser, I. Lieberwirth, P. W. Blom*, et al.*, "Controlling the microstructure of poly (vinylidene-fluoride)(PVDF) thin films for microelectronics," *Journal of Materials Chemistry C,* vol. 1, pp. 7695-7702, 2013.

[71] V. Sencadas, R. Gregorio Jr, and S. Lanceros-Méndez, "α to β phase transformation and microestructural changes of PVDF films induced by uniaxial stretch," *Journal of Macromolecular Science®,* vol. 48, pp. 514-525, 2009.
[72] P. F. P. Guide and P. List, "Measurement Specialities," *Inc., http://www. meas-spec. com,* 1999.
[73] Y. Zhou, J. He, H. Wang, K. Qi, N. Nan, X. You*, et al.*, "Highly sensitive, self-powered and wearable electronic skin based on pressure-sensitive nanofiber woven fabric sensor," *Scientific reports,* vol. 7, p. 12949, 2017.
[74] Y. Tokuhisa, T. Tomita, H. Hamada, S. Ishii, Y. Doshida, and Y. Watanabe, "Piezoelectric speaker and electroacoustic transducer," ed: Google Patents, 2016.
[75] M. Sharifzadeh Mirshekarloo, C. Y. Tan, X. Yu, Z. Lei, S. Chen, K. Yao*, et al.*, "Active noise mitigation window employing transparent piezoelectric film speakers," in *INTER-NOISE and NOISE-CON Congress and Conference Proceedings*, 2017, pp. 2511-2519.
[76] S. Z. Mansour and R. Seethaler, "Design of a test setup to independently vary displacement and force of piezoelectric stack actuators," in *SENSORS, 2017 IEEE*, 2017, pp. 1-3.
[77] Q. Pan, E. Miao, B. Wu, W. Chen, X. Lei, and L. He, "Bio-inspired piezoelectric linear motor driven by a single-phase harmonic wave with an asymmetric stator," *Review of Scientific Instruments,* vol. 88, p. 075002, 2017.
[78] N. W. Hagood and A. J. McFarland, "Modeling of a piezoelectric rotary ultrasonic motor," *IEEE Transactions on Ultrasonics, Ferroelectrics, and Frequency Control,* vol. 42, pp. 210-224, 1995.
[79] F. Ganet, M. Q. Le, J. F. Capsal, P. Lermusiaux, L. Petit, A. Millon*, et al.*, "Development of a smart guide wire using an electrostrictive polymer: option for steerable orientation and force feedback," *Scientific Reports,* vol. 5, Dec 17 2015.
[80] B. Jaffe, W. Cook, and H. Jaffe, *Piezoelectric Ceramics* New York: Academic, 1971.
[81] Z. L. Wang and J. H. Song, "Piezoelectric nanogenerators based on zinc oxide nanowire arrays," *Science,* vol. 312, pp. 242-246, Apr 14 2006.
[82] W. H. Ma and L. E. Cross, "Flexoelectricity of barium titanate," *Applied Physics Letters,* vol. 88, p. 2902, Jun 5 2006.
[83] M. S. Vijaya, *Piezoelectric Materials and Devices: Applications in Engineering and Medical Sciences*: CRC Press, 2012.
[84] D. J. Li, S. Hong, S. Y. Gu, Y. Choi, S. Nakhmanson, O. Heinonen*, et al.*, "Polymer piezoelectric energy harvesters for low wind speed," *Applied Physics Letters,* vol. 104, p. 012902, Jan 6 2014.
[85] E. Molino-Minero-Re, M. Carbonell-Ventura, C. Fisac-Fuentes, A. Manuel-Lazaro, and D. M. Toma, "Piezoelectric energy harvesting from induced vortex in water flow," in *Instrumentation and Measurement Technology Conference (I2MTC), 2012 IEEE International*, 2012, pp. 624-627.

[86] K. Ishida, T. C. Huang, K. Honda, Y. Shinozuka, H. Fuketa, T. Yokota*, et al.*, "Insole Pedometer With Piezoelectric Energy Harvester and 2 V Organic Circuits," *Ieee Journal of Solid-State Circuits,* vol. 48, pp. 255-264, Jan 2013.

[87] D. H. Kim, R. Ghaffari, N. S. Lu, and J. A. Rogers, "Flexible and Stretchable Electronics for Biointegrated Devices," *Annual Review of Biomedical Engineering, Vol 14,* vol. 14, pp. 113-128, 2012.

[88] Y. Qi and M. C. McAlpine, "Nanotechnology-enabled flexible and biocompatible energy harvesting," *Energy & Environmental Science,* vol. 3, pp. 1275-1285, Sep 2010.

[89] Y. Qin, X. D. Wang, and Z. L. Wang, "Microfibre-nanowire hybrid structure for energy scavenging," *Nature,* vol. 451, pp. 809-U5, Feb 14 2008.

[90] Y. Qi, T. D. Nguyen, P. K. Purohit, and M. C. McAlpine, "Stretchable Piezoelectric Nanoribbons for Biocompatible Energy Harvesting," in *Stretchable Electronics*, ed: Wiley-VCH Verlag GmbH & Co. KGaA, 2012, pp. 111-139.

[91] K. I. Park, S. Xu, Y. Liu, G. T. Hwang, S. J. L. Kang, Z. L. Wang*, et al.*, "Piezoelectric BaTiO3 Thin Film Nanogenerator on Plastic Substrates," *Nano Letters,* vol. 10, pp. 4939-4943, Dec 2010.

[92] E. Hausler, L. Stein, and G. Harbauer, "Implantable Physiological Power Supply with Pvdf Film," *Ferroelectrics,* vol. 60, pp. 277-282, 1984.

[93] D. J. Chen, T. Sharma, and J. X. J. Zhang, "Mesoporous surface control of PVDF thin films for enhanced piezoelectric energy generation," *Sensors and Actuators a-Physical,* vol. 216, pp. 196-201, Sep 1 2014.

[94] D. J. Chen and J. X. J. Zhang, "Microporous polyvinylidene fluoride film with dense surface enables efficient piezoelectric conversion," *Applied Physics Letters,* vol. 106, p. 193901, May 11 2015.

[95] D. J. Chen, C. Wang, W. Chen, Y. Q. Chen, and J. X. J. Zhang, "PVDF-Nafion nanomembranes coated microneedles for in vivo transcutaneous implantable glucose sensing," *Biosensors & Bioelectronics,* vol. 74, pp. 1047-1052, Dec 15 2015.

[96] Q. M. Wang, X. H. Du, B. M. Xu, and L. E. Cross, "Theoretical analysis of the sensor effect of cantilever piezoelectric benders," *Journal of Applied Physics,* vol. 85, pp. 1702-1712, Feb 1 1999.

[97] J. G. Smits and W. S. Choi, "The Constituent Equations of Piezoelectric Heterogeneous Bimorphs," *Ieee Transactions on Ultrasonics Ferroelectrics and Frequency Control,* vol. 38, pp. 256-270, May 1991.

[98] M. Umeda, K. Nakamura, and S. Ueha, "Analysis of the transformation of mechanical impact energy to electric energy using piezoelectric vibrator," *Japanese Journal of Applied Physics Part 1-Regular Papers Short Notes & Review Papers,* vol. 35, pp. 3267-3273, May 1996.

[99] T. H. Ng and W. H. Liao, "Sensitivity analysis and energy harvesting for a self-powered piezoelectric sensor," *Journal of Intelligent Material Systems and Structures,* vol. 16, pp. 785-797, Oct 2005.

[100] H. D. Li, C. Tian, and Z. D. Deng, "Energy harvesting from low frequency applications using piezoelectric materials," *Applied Physics Reviews,* vol. 1, p. 041301, Dec 2014.
[101] Y. Qiu, D. C. Yang, B. Yin, J. X. Lei, H. Q. Zhang, Z. Zhang*, et al.*, "Branched ZnO nanotrees on flexible fiber-paper substrates for self-powered energy-harvesting systems," *Rsc Advances,* vol. 5, pp. 5941-5945, 2015.
[102] V. F. M. Guizzetti, D. Marioli and T. Zawada, "Thickness Optimization of a Piezoelectric Converter for Energy Harvesting," in *COMSOL Conference*, Milan, 2009.
[103] A. Nechibvute and C. Mudzingwa, "The Effect Of Substrate To Piezoelectric Thickness Ratio On Performance Of Unimorph Sensor," *International Journal of Engineering Research & Technology,* vol. 2, pp. 2678-2682, April 2013.
[104] S. N. Jagtap and R. Paily, "Geometry Optimization of a MEMS-based Energy Harvesting Device," in *Proceeding of the 2011 IEEE Students' Technology Symposium*, IIT Kharagpur, 2011, pp. 265-269.
[105] J. K. Park and W. K. Moon, "Constitutive relations for piezoelectric benders under various boundary conditions," *Sensors and Actuators a-Physical,* vol. 117, pp. 159-167, Jan 3 2005.
[106] J. W. Hutchinson and Z. Suo, "Mixed-Mode Cracking in Layered Materials," *Advances in Applied Mechanics, Vol 29,* vol. 29, pp. 63-191, 1992.
[107] Q. Chen, D. Natale, B. Neese, K. L. Ren, M. R. Lin, Q. M. Zhang*, et al.*, "Piezoelectric polymers actuators for precise shape control of large scale space antennas - art. no. 65241P," *Electroactive Polymer Actuators and Devices (EAPAD) 2007,* vol. 6524, pp. P5241-P5241, 2007.
[108] A. Navid, C. S. Lynch, and L. Pilon, "Purified and porous poly(vinylidene fluoride-trifluoroethylene) thin films for pyroelectric infrared sensing and energy harvesting," *Smart Materials and Structures,* vol. 19, p. 055006, May 2010.
[109] N. N. Rogacheva, *The theory of piezoelectric shells and plates*. Boca Raton: CRC Press, 1994.
[110] N. R. Cowan, "The Heart-Lung Coefficient and The Transverse Diameter of The Heart," *British Heart Journal,* vol. 26, pp. 116-&, 1964.
[111] Dieudonn.Jm and C. F. Jean, "Epicardial Strains during Left Ventricular Contraction Cycle," *American Journal of Physiology,* vol. 216, pp. 1188-&, 1969.
[112] G. Wang, "Analysis of bimorph piezoelectric beam energy harvesters using Timoshenko and Euler-Bernoulli beam theory," *Journal of Intelligent Material Systems and Structures,* vol. 24, pp. 226-239, Jan 2013.
[113] X. P. Li, W. Y. Shih, I. A. Aksay, and W. H. Shih, "Electromechanical behavior of PZT-brass unimorphs," *Journal of the American Ceramic Society,* vol. 82, pp. 1733-1740, Jul 1999.
[114] A. Alwan, *Global status report on noncommunicable diseases 2010*: World Health Organization, 2011.

[115] M. M. Baig, H. Gholamhosseini, and M. J. Connolly, "A comprehensive survey of wearable and wireless ECG monitoring systems for older adults," *Medical & Biological Engineering & Computing,* vol. 51, pp. 485-495, May 2013.
[116] S. R. Steinhubl, R. R. Mehta, G. S. Ebner, M. M. Ballesteros, J. Waalen, G. Steinberg*, et al.*, "Rationale and design of a home-based trial using wearable sensors to detect asymptomatic atrial fibrillation in a targeted population: The mHealth Screening To Prevent Strokes (mSToPS) trial," *American Heart Journal,* vol. 175, pp. 77-85, May 2016.
[117] J. A. Walsh, E. J. Topol, and S. R. Steinhubl, "Novel Wireless Devices for Cardiac Monitoring," *Circulation,* vol. 130, pp. 573-581, Aug 12 2014.
[118] P. K. Jain and A. K. Tiwari, "Heart monitoring systems—A review," *Computers in biology and medicine,* vol. 54, pp. 1-13, 2014.
[119] R. Rhoades and D. R. Bell, *Medical physiology : principles for clinical medicine*, 3rd ed. Philadelphia: Lippincott Williams & Wilkins, 2009.
[120] O. Postolache, P. Girão, and G. Postolache, "Seismocardiogram and Ballistocardiogram Sensing," *Advanced Instrument Engineering: Measurement, Calibration, and Design: Measurement, Calibration, and Design,* p. 223, 2013.
[121] O. T. Inan, P. F. Migeotte, K. S. Park, M. Etemadi, K. Tavakolian, R. Casanella*, et al.*, "Ballistocardiography and Seismocardiography: A Review of Recent Advances," *Ieee Journal of Biomedical and Health Informatics,* vol. 19, pp. 1414-1427, Jul 2015.
[122] Y. Liu, J. J. Norton, R. Qazi, Z. Zou, K. R. Ammann, H. Liu*, et al.*, "Epidermal mechano-acoustic sensing electronics for cardiovascular diagnostics and human-machine interfaces," *Science Advances,* vol. 2, p. e1601185, 2016.
[123] P. Castiglioni, A. Faini, G. Parati, and M. Di Rienzo, "Wearable seismocardiography," *2007 Annual International Conference of the Ieee Engineering in Medicine and Biology Society, Vols 1-16,* pp. 3954-3957, 2007.
[124] J. Tichý, *Fundamentals of Piezoelectric Sensorics : Mechanical, Dielectric, and Thermodynamical Properties of Piezoelectric Materials*.
[125] S. Noh, C. Yoon, E. Hyun, H. N. Yoon, T. J. Chung, K. S. Park*, et al.*, "Ferroelectret film-based patch-type sensor for continuous blood pressure monitoring," *Electronics Letters,* vol. 50, pp. 143-144, Jan 30 2014.
[126] S. R. Anton, K. M. Farinholt, and A. Erturk, "Piezoelectret foam-based vibration energy harvesting," *Journal of Intelligent Material Systems and Structures,* vol. 25, pp. 1681-1692, Sep 2014.
[127] F. F. Hendriks, "Mechanical behaviour of human epidermal and dermal layers in vivo," *Eindhoven: Technische Universiteit Eindhoven,* p. 106, 2005.
[128] T. Widlund, S. X. Yang, Y. Y. Hsu, and N. S. Lu, "Stretchability and compliance of freestanding serpentine-shaped ribbons," *International Journal of Solids and Structures,* vol. 51, pp. 4026-4037, Nov 2014.

[129] S. K. Ameri, R. Ho, H. Jang, Y. Wang, D. M. Schnyer, D. Akinwande*, et al.*, "Thinnest Transparent Epidermal Sensor System Based on Graphene," *2016 Ieee International Electron Devices Meeting (Iedm),* 2016.
[130] S. Yang, S. Qiao, and N. Lu, "Elasticity solutions to nonbuckling serpentine ribbons," *Journal of Applied Mechanics,* vol. 84, p. 021004, 2017.
[131] N. Lu, X. Wang, Z. Suo, and J. Vlassak, "Metal films on polymer substrates stretched beyond 50%," *Applied Physics Letters,* vol. 91, p. 221909, 2007.
[132] W. D. Jenkins, T. G. Digges, and C. R. Johnson, "Tensile Properties of Copper, Nickel, and 70-Percent-Copper-30-Percent-Nickel and 30-Percent-Copper-70-Percent-Nickel Alloys at High Temperatures," *Journal of Research of the National Bureau of Standards,* vol. 58, pp. 201-211, 1957.
[133] Y. Hara, Y. Masuda, T. Hirao, and N. Yoshikawa, "The relationship between the Young's modulus of the stratum corneum and age: a pilot study," *Skin Research and Technology,* vol. 19, pp. 339-345, 2013.
[134] K. Pandia, S. Ravindran, R. Cole, G. Kovacs, and L. Giovangrandi, "Motion artifact cancellation to obtain heart sounds from a single chest-worn accelerometer," in *Acoustics Speech and Signal Processing (ICASSP), 2010 IEEE International Conference on*, 2010, pp. 590-593.
[135] C. Yang and N. Tavassolian, "Motion artifact cancellation of seismocardiographic recording from moving subjects," *IEEE Sensors Journal,* vol. 16, pp. 5702-5708, 2016.
[136] M. Di Rienzo, P. Meriggi, E. Vaini, P. Castiglioni, and F. Rizzo, "24h seismocardiogram monitoring in ambulant subjects," in *Engineering in Medicine and Biology Society (EMBC), 2012 Annual International Conference of the IEEE*, 2012, pp. 5050-5053.
[137] C. Yang and N. Tavassolian, "Motion noise cancellation in seismocardiogram of ambulant subjects with dual sensors," in *Engineering in Medicine and Biology Society (EMBC), 2016 IEEE 38th Annual International Conference of the*, 2016, pp. 5881-5884.
[138] M. Paukkunen, M. Linnavuo, and R. Sepponen, "A portable measurement system for the superior-inferior axis of the seismocardiogram," *J Bioengineer Biomedical Sci,* vol. 3, pp. 1-4, 2013.
[139] K. Pandia, O. T. Inan, G. T. Kovacs, and L. Giovangrandi, "Extracting respiratory information from seismocardiogram signals acquired on the chest using a miniature accelerometer," *Physiological measurement,* vol. 33, p. 1643, 2012.
[140] C. M. Agress, L. G. Fields, S. Wegner, M. Wilburne, M. D. Shickman, and R. M. Muller, "The normal vibrocardiogram: Physiologic variations and relation to cardiodynamic events," *American Journal of Cardiology,* vol. 8, pp. 22-31, 1961.
[141] W.-Y. Lin, W.-C. Chou, P.-C. Chang, C.-C. Chou, M.-S. Wen, M.-Y. Ho*, et al.*, "Identification of Location Specific Feature Points in a Cardiac Cycle Using a Novel Seismocardiogram Spectrum System," *IEEE journal of biomedical and health informatics,* 2016.

[142] G. Shafiq and K. C. Veluvolu, "Surface chest motion decomposition for cardiovascular monitoring," *Scientific reports,* vol. 4, p. 5093, 2014.
[143] S. De Panfilis, C. Moroni, M. Peccianti, O. Chiru, V. Vashkevich, G. Parisi*, et al.*, "Multi-point accelerometric detection and principal component analysis of heart sounds," *Physiological measurement,* vol. 34, p. L1, 2013.
[144] T. Cheng, C. Dai, and R. Z. Gan, "Viscoelastic properties of human tympanic membrane," *Annals of biomedical engineering,* vol. 35, pp. 305-314, 2007.
[145] B. L. Boyce, J. M. Grazier, R. E. Jones, and T. D. Nguyen, "Full-field deformation of bovine cornea under constrained inflation conditions," *Biomaterials,* vol. 29, pp. 3896-3904, 2008.
[146] M. Sutton, X. Ke, S. Lessner, M. Goldbach, M. Yost, F. Zhao*, et al.*, "Strain field measurements on mouse carotid arteries using microscopic three-dimensional digital image correlation," *Journal of Biomedical Materials Research Part A,* vol. 84, pp. 178-190, 2008.
[147] S. Omkar and A. Singh, "Analysis of Wrist Extension using Digital Image Correlation," *ICTACT Journal on Image and Video Processing,* vol. 2, pp. 343-351, 2012.
[148] A. Singh and S. Omkar, "ANALYSIS OF TARSAL TUNNEL SYNDROME USING IMAGE CORRELATION," *Journal of Dental Materials & Techniques,* vol. 4, 2013.
[149] E. W. Obropta and D. J. Newman, "Skin strain fields at the shoulder joint for mechanical counter pressure space suit development," *2016 Ieee Aerospace Conference,* 2016.
[150] E. W. Obropta and D. J. Newman, "A comparison of human skin strain fields of the elbow joint for mechanical counter pressure space suit development," *2015 Ieee Aerospace Conference,* 2015.
[151] J. G. Webster, *The physiological measurement handbook*.
[152] W. Korzeniowska-Kubacka, M. Bilinska, and R. Piotrowicz, "Usefulness of seismocardiography for the diagnosis of ischemia in patients with coronary artery disease," *Annals of Noninvasive Electrocardiology,* vol. 10, pp. 281-287, Jul 2005.
[153] J. Y. Sun, N. S. Lu, J. Yoon, K. H. Oh, Z. G. Suo, and J. J. Vlassak, "Inorganic islands on a highly stretchable polyimide substrate," *Journal of Materials Research,* vol. 24, pp. 3338-3342, Nov 2009.
[154] N. S. Lu, X. Wang, Z. G. Suo, and J. Vlassak, "Metal films on polymer substrates stretched beyond 50%," *Applied Physics Letters,* vol. 91, Nov 26 2007.
[155] L. Peter, N. Noury, and M. Cerny, "A review of methods for non-invasive and continuous blood pressure monitoring: Pulse transit time method is promising?," *Irbm,* vol. 35, pp. 271-282, Oct 2014.
[156] W. Chen, T. Kobayashi, S. Ichikawa, Y. Takeuchi, and T. Togawa, "Continuous estimation of systolic blood pressure using the pulse arrival time and intermittent calibration," *Medical & Biological Engineering & Computing,* vol. 38, pp. 569-574, Sep 2000.

[157] P. A. Obrist, K. C. Light, J. A. Mccubbin, J. S. Hutcheson, and J. L. Hoffer, "Pulse Transit-Time - Relationship to Blood-Pressure and Myocardial Performance," *Psychophysiology,* vol. 16, pp. 292-301, 1979.
[158] C. C. Y. Poon and Y. T. Zhang, "Cuff-less and noninvasive measurements of arterial blood pressure by pulse transit time," *2005 27th Annual International Conference of the IEEE Engineering in Medicine and Biology Society, Vols 1-7,* pp. 5877-5880, 2005.
[159] M. S. Imtiaz, R. Shrestha, T. Dhillon, K. A. Yousuf, B. Saeed, A. Dinh*, et al.*, "Correlation Between Seismocardiogram and Systolic Blood Pressure," *2013 26th Annual Ieee Canadian Conference on Electrical and Computer Engineering (Ccece),* pp. 501-504, 2013.
[160] X. L. Aubert, J. Muehlsteff, and C. Zhu, "Relationships between blood pressure and systolic time-intervals: a lumped-model simulation study," *2007 Annual International Conference of the Ieee Engineering in Medicine and Biology Society, Vols 1-16,* pp. 1707-1710, 2007.
[161] X. Y. Zhang, E. MacPherson, and Y. T. Hang, "Relations between the timing of the second heart sound and aortic blood pressure," *Ieee Transactions on Biomedical Engineering,* vol. 55, pp. 1291-1297, Apr 2008.
[162] H. Tang, J. Gao, and Y. Park, "Heart valve closure timing intervals in response to left ventricular blood pressure," 2013.
[163] H. Tang, J. H. Zhang, H. M. Chen, A. Mondal, and Y. Park, "A non-invasive approach to investigation of ventricular blood pressure using cardiac sound features," *Physiological Measurement,* vol. 38, pp. 289-309, Feb 2017.
[164] I. Korzeniowska-Kubacka, B. Kumierczyk-Droszcz, M. Biliska, B. Dobraszkiewicz-Wasilewska, and K. Piotrowicz, "Seismocardiography-a non-invasive method of assessing systolic and diastolic left ventricular function in ischaemic heart disease," *Folia Cardiol,* vol. 13, pp. 319-325, 2006.
[165] DanielChangMD, DestinyQx, and xacax, "Wiggers Diagram," Wiggers_Diagram.svg, Ed., ed. Wikimedia: Creative Commons Attribution-Share Alike 4.0 International license, 2012.
[166] H. Tanaka, K. D. Monahan, and D. R. Seals, "Age-predicted maximal heart rate revisited," *Journal of the American College of Cardiology,* vol. 37, pp. 153-156, Jan 2001.
[167] K. Lu, J. W. Clark, F. H. Ghorbel, D. L. Ware, and A. Bidani, "A human cardiopulmonary system model applied to the analysis of the Valsalva maneuver," *American Journal of Physiology-Heart and Circulatory Physiology,* vol. 281, pp. H2661-H2679, Dec 2001.
[168] F. Y. Liang and H. Liu, "Simulation of hemodynamic responses to the Valsalva maneuver: An integrative computational model of the cardiovascular system and the autonomic nervous system," *Journal of Physiological Sciences,* vol. 56, pp. 45-65, Feb 2006.

[169] X. W. Wang, Y. Gu, Z. P. Xiong, Z. Cui, and T. Zhang, "Silk-Molded Flexible, Ultrasensitive, and Highly Stable Electronic Skin for Monitoring Human Physiological Signals," *Advanced Materials,* vol. 26, pp. 1336-1342, Mar 2014.
[170] W. Zeng, L. Shu, Q. Li, S. Chen, F. Wang, and X. M. Tao, "Fiber-Based Wearable Electronics: A Review of Materials, Fabrication, Devices, and Applications," *Advanced Materials,* vol. 26, pp. 5310-5336, Aug 20 2014.
[171] W. Honda, S. Harada, T. Arie, S. Akita, and K. Takei, "Wearable, Human-Interactive, Health-Monitoring, Wireless Devices Fabricated by Macroscale Printing Techniques," *Advanced Functional Materials,* vol. 24, pp. 3299-3304, Jun 2014.
[172] Y. Ahn, S. Song, and K. S. Yun, "Woven flexible textile structure for wearable power-generating tactile sensor array," *Smart Materials and Structures,* vol. 24, Jul 2015.
[173] R. R. Hainich, *The End of hardware: augmented reality and beyond*: BookSurge, 2009.
[174] J. A. Main and E. Garcia, "Piezoelectric stack actuators and control system design: strategies and pitfalls," *Journal of Guidance, Control, and Dynamics,* vol. 20, pp. 479-485, 1997.
[175] S. Chang, E. Murdock, Y. Mao, C. Flueraru, and J. Disano, "Stationary-fiber rotary probe with unobstructed 360 view for optical coherence tomography," *Optics letters,* vol. 36, pp. 4392-4394, 2011.
[176] U. Afaq and Omkar, "Endogenously entrained life events of Parthenium beetle, Zygogramma bicolorata Pallister (Coleoptera: Chrysomelidae)," *Biological Rhythm Research,* vol. 47, pp. 885-896, 2016.
[177] K. Spanner and B. Koc, "Piezoelectric motors, an overview," in *Actuators*, 2016, p. 6.
[178] Y. Tajitsu, "Fundamental study on improvement of piezoelectricity of poly (ι-lactic acid) and its application to film actuators," *IEEE transactions on ultrasonics, ferroelectrics, and frequency control,* vol. 60, pp. 1625-1629, 2013.